Aging disrupts spatiotemporal coordination in the cycling murine ovary

Tammy C.T. Lan[1,2,*], Alison Kochersberger[3,*], Ruth Raichur[1], Sophia Szady[4], Hien Tran[4,5], Radiana Simeonova[4,5], Ashley Helmuth[4], Andrew Minagar[4,5], Maria José Orozco Fuentes[4], Vipin Kumar[1], Giovanni Marrero[1], Irving Barrera[1], Sarah Mangiameli[1], Alex K. Shalek[1,6,7,8,9], Pardis C. Sabeti[1,10,11,12], Fei Chen[1,13], David S. Fischer[1,†], Jennifer L. Garrison[3,14-16,†], Hattie Chung[1,4,17-19,†]

[1]The Broad Institute of MIT and Harvard, Cambridge, MA, USA
[2]Department of Molecular and Cellular Biology, Harvard University, Cambridge, MA, USA
[3]Buck Institute for Research on Aging, Novato, CA, USA
[4]Department of Medicine, Cardiovascular Research Center, Yale School of Medicine, New Haven, CT, USA
[5]Yale College, New Haven, CT, USA
[6]Institute for Medical Engineering and Science (IMES), Massachusetts Institute of Technology, Cambridge, MA, USA
[7]Department of Chemistry, Massachusetts Institute of Technology, Cambridge, MA, USA
[8]Koch Institute for Integrative Cancer Research, Massachusetts Institute of Technology, Cambridge, MA, USA
[9]Ragon Institute of MGH, MIT and Harvard, Cambridge, MA, USA
[10]Howard Hughes Medical Institute, Chevy Chase, MD, USA
[11]Department of Organismic and Evolutionary Biology, Harvard University, Cambridge, MA, USA
[12]Department of Immunology and Infectious Diseases, Harvard T.H. Chan School of Public Health, Harvard University, Boston, MA, USA
[13]Department of Stem Cell and Regenerative Biology, Harvard University, Cambridge, MA, USA
[14]Center for Healthy Aging in Women, Novato, CA, USA
[15]Department of Cellular and Molecular Pharmacology, University of California, San Francisco, CA, USA
[16]Leonard Davis School of Gerontology, University of Southern California, Los Angeles, CA, USA
[17]Department of Molecular, Cellular and Developmental Biology, Yale University, New Haven, CT, USA
[18]Department of Obstetrics, Gynecology and Reproductive Sciences, Yale School of Medicine, New Haven, CT, USA
[19]Yale Center for Research on Aging, Yale School of Medicine, New Haven, CT, USA
*These authors contributed equally to this work.
[†]To whom correspondence should be addressed: hattie.chung@yale.edu (HC), jgarrison@buckinstitute.org (JG), and david.fischer@meduniwien.ac.at (DSF)

Summary

Throughout the female reproductive lifespan, the ovary completes hundreds of cycles of follicle development, ovulation, and tissue regeneration[1–3]. These processes rely on the precisely coordinated intricate multicellular interactions across time and space[4]. How aging disrupts these interactions, leading to an overall decline in reproductive and endocrine functions, remains understudied. To understand the multicellular dynamics that underlie ovarian function and their changes with age, here we use Slide-seq, a near-cellular spatial transcriptomics method, to profile 22 mouse ovaries across the reproductive cycle and chronological age, representing 610,620 near-cellular spots across 69 spatial transcriptomic profiles[5,6]. We develop a segmentation analysis to identify spatial niches that capture different states of folliculogenesis from static snapshots *in situ*, allowing us to examine the multicellular dynamics of 358 oocytes, 668 follicles, and 236 corpora lutea. We find that aging disrupts both the spatial organization and temporal coordination of folliculogenesis before the cessation of cycling, which may contribute to the dysregulation of hormone production and signaling. These disruptions are marked by altered immune cell dynamics, inflammatory signaling, and global tissue disorganization that impair the cyclic remodeling required for ovarian function. Our findings reveal how multicellular niches orchestrate ovarian function and demonstrate how age-related breakdown of tissue organization across time and space precedes reproductive decline.

48 **Main Text**

49 The ovary is a dynamic organ comprising diverse cell types that undergo continuous remodeling to regulate
50 reproductive and endocrine function throughout the female lifespan. During the female reproductive period, ovarian
51 cells undergo a repetitive cycle of phenotypic switching to collectively orchestrate oocyte maturation, ovulation,
52 and hormone production throughout the estrous or menstrual cycle[4,7]. This process of "homeostatic cycling" occurs
53 approximately 150–650 times in mice and 300–400 times in humans over the course of the female reproductive
54 lifespan[1,2]. During chronological aging, overall reproductive function declines and culminates in the cessation of
55 cycling. Here, we investigate the molecular interactions underlying this process, including the progressive depletion
56 of the ovarian reserve, the decline in the precision of cellular interactions, and the increase in tissue-wide
57 inflammation and fibrosis[8–13].

58

59 Central to ovarian function are spatially organized dynamic multicellular structures – primarily follicles, which
60 develop in distinct stages before transforming into corpora lutea (CL) after ovulation. Folliculogenesis begins with
61 a primordial follicle consisting of a dormant oocyte encased by flattened granulosa cells (GCs). Activation, the
62 awakening of the follicle from its dormant phase, triggers GCs to adopt a cuboidal shape and begin proliferation,
63 forming the preantral follicle where they coordinate morphological and functional changes to support oocyte
64 growth. As the follicle transitions to the antral stage, a fluid-filled cavity (antrum) forms, and the follicle becomes
65 gonadotropin-dependent for growth and begins producing steroid hormones[14,15]. Spatial complexity further
66 increases as theca cells create an outer layer and respond to gonadotropin hormones by producing steroids[16,17].
67 Ultimately, less than 1% of follicles recruited to grow successfully progress to ovulation[18], while the remainder
68 undergo atresia, a form of apoptosis[18]. Though atresia claims most follicles during their maturation process – which
69 spans approximately two weeks in mice and more than a year in humans – the dominant surviving follicle releases
70 a mature oocyte at ovulation. After oocyte ejection, the remaining follicular cells transform into the CL, a transient
71 hormone-producing structure essential for pregnancy and critical in regulating the complex cycle of ovulation[15,19].
72 This creates an extraordinarily complex tissue environment where, at any given time, dozens (mice) or thousands
73 (humans) of follicles at different developmental stages share the same physical space with multiple CLs[20,21]. The
74 molecular mechanisms coordinating this intricate asynchronous spatiotemporal organization remain unclear,
75 highlighting the need for spatially resolved profiling to better understand the dynamics of these cellular ecosystems.

76

77 Previous studies of ovarian aging focused primarily on follicle depletion and decline in oocyte-intrinsic properties
78 such as aneuploidy[22,23]. However, mounting evidence suggests that dysfunction across the entire ovarian tissue
79 environment driven by the repeated cyclic remodeling of folliculogenesis and ovulation contributes significantly to
80 reproductive aging through dysregulation of these multicellular ecosystems[10,12,23–25], particularly through
81 disruptions in granulosa cell signaling[26–28], extracellular matrix remodeling[29–32], and immune infiltration[12,33–35],
82 underscoring the need to investigate how multicellular dysregulation drives ovarian aging. Single-cell RNA
83 sequencing is a powerful tool to profile cellular heterogeneity and uncover novel regulatory mechanisms, but it

84 faces limitations in studying ovarian tissue. Droplet-based single-cell methods are limited in their ability to profile
85 large cells like oocytes, which exceed 100 µm in diameter resulting in capture of early stage oocytes in low
86 abundance making analysis challenging[36–39] and do not resolve interacting cell types in the follicular niche, while
87 coarse spatial transcriptomics approaches lack the resolution to characterize follicular architecture[25,40] and often rely
88 on predetermined gene panels that constrain discovery of novel regulatory patterns within and across niches[41].
89
90 Here, we present a spatiotemporal atlas of the naturally cycling C57BL/6J murine ovary across chronological aging
91 at near-single-cell resolution using Slide-seq[5,6]. Our study comprises *n*=610,620 spots at 10 µm resolution spanning
92 69 spatial transcriptomic profiles from 22 biological samples collected during the estrus and metestrus stages of the
93 estrous cycle, across three age groups. To characterize the cooperative nature of critical multicellular structures in
94 the ovary, we developed a segmentation pipeline that identified 358 primordial and growing oocytes, 668 follicles
95 of which 301 enclosed oocytes, and 236 CLs, enabling detailed analysis of *in situ* molecular signatures. Comparing
96 profiles between young and aged mice revealed that aging disrupts the temporal dynamics of folliculogenesis and
97 corpus luteum function during the estrous cycle. This disruption coincides with increased inflammatory signatures
98 and a decline in tissue organization, which may compound ovarian dysfunction. Our work highlights how
99 multicellular niches cooperate within the ovary and proposes that temporal dysregulation of these niches contributes
100 to the decline in reproductive and endocrine function with age.
101
102 ***Spatial transcriptomics reveals multicellular organization of the cycling and aging ovary***
103 We used Slide-seq to generate 69 spatial transcriptomics profiles from 22 mice harvested during ovulatory (estrus)
104 and post-ovulatory (metestrus) stages across young (10-12 weeks), reproductively middle aged (36-40 weeks), and
105 reproductively old (52-54 weeks) mice[42] (**Fig. 1a**; **Extended Data Fig. 1a, Extended Tables 1, 2**; **Methods**). This
106 design enabled us to examine the post-ovulatory tissue-wide remodeling across aging. Unsupervised clustering and
107 *post hoc* annotation of 601,831 high-quality 10 µm spot transcriptomes identified all major ovarian cell types,
108 including oocytes (*Gdf9*), multiple GC subtypes, two luteal cell populations (defined by *Parm1* and *Akr1c18*), theca
109 cells (*Col1a2*), epithelial cells (*Epcam*), fibroblasts (*Pdgfra*), smooth muscle cells (*Tagln*), immune (*Lyz2*),
110 endothelial (*Flt1*), stromal cells (*Aldh1a1*), and others (**Fig. 1b,c**; **Extended Data Fig. 1b**; **Extended Table 3**;
111 **Supplementary File 1**). Cell types were found across all ages, with an age-associated decrease in oocytes and an
112 increase in immune cells (**Fig. 1c**). To validate our Slide-seq annotations with truly single-nucleus transcriptomics,
113 we also performed snRNA-seq on whole ovaries, which revealed a consistent set of cell populations, but with a
114 notable loss of oocytes and cumulus cells, highlighting the advantage of our combined approach for capturing a
115 more complete ovarian cellular atlas (**Extended Data Fig. 1c,d**).
116
117 To analyze anatomically related groups of spots representing meaningful tissue units, we developed a segmentation
118 pipeline that identified oocytes, follicles, and corpora lutea. As large oocytes often exceed 70 µm in diameter[43]
119 thereby spanning multiple Slide-seq spots, we clustered spatially adjacent putative oocyte spots into segments to

120 create composite oocyte profiles for further analysis (**Methods**). As oocytes in primordial follicles typically
121 comprise roughly 2 spots, we identified these through a separate pipeline that segmented at least 2 neighboring
122 oocyte spots (**Methods**). The identity of primordial oocytes was further validated by expression of additional marker
123 genes such as *Sohlh1* and *Nobox*[44] (**Extended Data Fig. 1e**).
124
125 Larger structures, follicles and CL, were identified via unsupervised clustering of the spatial neighborhood graph
126 and classified based on their GC and luteal composition. These segments revealed distinct stages of follicular
127 development, including preantral (n=238), antral mitotic (n=191), antral luteinizing (n=43), and atretic (n=181)
128 follicles, as well as two types of CLs classified as *Parm*1 (n=87) and *Akr1c18* (n=147) (**Extended Data Fig. 1g,h**;
129 **Methods**). We validated the segmentation pipeline by manually annotating adjacent H&E-stained sections (**Fig.
130 1e-g**; **Extended Data Fig. 1i**; **Supplementary Files 2,3**; **Methods**). Follicle classifications captured the progression
131 of GC function that drives folliculogenesis (**Fig. 1h**), supported by stage-specific expression of key hormone
132 receptors, including the anti-Müllerian hormone receptor *Amhr2* in gonadotropin-independent preantral follicles[45]
133 and *Fshr* and *Lhcgr* in gonadotropin-dependent antral follicles[46,47] (**Fig. 1i**). Additionally, to provide orthogonal
134 support for identifying atretic follicles beyond transcriptional signatures, we examined the spatial distribution of
135 immune cells within follicles[37]. We observed that atretic follicles show increased immune infiltration toward the
136 follicle center, whereas healthy follicles exhibit minimal immune presence (**Extended Data Fig. j**; $P<0.001$ antral
137 *vs* atretic follicles, Tukey's test), which aligns with prior observations that immune cells infiltrate dying follicles
138 for tissue clearance[12]. Altogether, these results demonstrate that our segmentation pipeline captures the multicellular
139 architecture and functional organization of the ovary.
140
141 ***Oocytes follow coordinated transcriptional programs during follicular development***
142 Despite the traditional characterization of oocytes as transcriptionally silent maternal RNA storage units[48], recent
143 studies have demonstrated active transcriptional regulation during their maturation[43,49,50]. From follicle activation,
144 primordial oocytes grow approximately 7-fold in size, progressing from prophase I to arrested metaphase II over
145 the course of 18 days in mice[51]. We examined distinct transcriptional patterns of oocytes in their native tissue
146 context, defined by the enclosing follicle typ[36,52–54]. *Sohlh1* was elevated in primordial oocytes[55], *Figla* and *Kit* in
147 preantral follicles, and *Gdf9* and *H1f8* in antral follicles (**Fig. 2a-c**). We next identified distinct gene programs that
148 differ across oocyte maturation via nonnegative matrix factorization, revealing five programs that significantly
149 differed in their utilization across oocytes at different follicle stages (NMF; **Fig. 2d**; **Methods**; **Extended Data Fig.
150 2a-c**). Oocyte program 2, characterized by zona pellucida glycoproteins *Zp2* and *Zp3*, was upregulated in primordial
151 and preantral oocytes, suggesting upregulation of extracellular matrix components necessary for follicular assembly
152 immediately after primordial follicle activation[56,57]. Oocyte program 4, enriched in F-box proteins (*Fbxw19,
153 Fbxw21, Fbxw24*) that are critical components of the SCF ubiquitin E3 ligase complex controlling cell cycle
154 progression[58,59] and *Bmp15*, emerged in mature antral oocytes, reflecting the rapid shifts necessary for meiotic
155 progression. Oocyte program 0 which contains the regulator of meiosis resumption, *Bcl2l10*, and early embryonic

156 development genes *Btg4* and *Tcl1* was elevated in mature follicles preparing to respond to the gonadotropin surge
157 (**Fig. 2e**; **Extended Data Fig. 1b**; $P<0.001$ preantral vs antral; t-test)[60–62]. Oocytes within atretic follicles showed
158 divergent expression of regulators of maturation processes, with lowered expression of *Padi6* and upregulation of
159 oocyte program 0 (**Fig. 2a,e**; **Extended Data Fig. 2b**; $P<0.05$ antral vs atretic; t-test). Altogether, our findings
160 reveal that oocytes undergo dynamic transcriptional regulation throughout folliculogenesis, switching from
161 processes required to maintain oocyte dormancy to proliferative programs upon follicle activation.
162
163 ***Aging alters regulators of oocyte maturation***
164 Aging leads to both the depletion and functional decline of maturing oocytes, with reduced oocyte quality observed
165 across follicle stages[63,64]. Consistent with this, we observed a sharp decrease in the average oocyte numbers in each
166 puck across all follicle types with age (**Fig. 2f**). Differential expression analysis between maturing oocytes of young
167 and old animals revealed multiple genes that change with age (**Extended Data Fig. 2d**; **Methods**). In particular,
168 expression of the nuclear androgen receptor *Ar* and hydroxysteroid dehydrogenase *Akr1c18,* known to metabolize
169 progesterone, increased in aging oocytes (**Fig. 2g**; **Extended Data Fig. 2d**). These genes are known to be involved
170 in oocyte maturation and meiosis[65–67], and their upregulation may reflect an adaptive shift by oocytes to changing
171 hormone levels in the aging ovarian environment[68,69]. Furthermore, we observed decreased expression of the insulin-
172 degrading enzyme *Ide*, which attenuates insulin signaling in healthy folliculogenesis[70,71]. Insulin signaling regulates
173 the final stages of oocyte maturation, although high insulin levels can reduce oocyte quality, underscoring the need
174 for balanced signaling[71,72]. Interestingly, aging oocytes show downregulation of the *Nlrp9b* family genes
175 (*Nlrp9a*/*b*/*c*), which normally increases during late maturation in young oocytes[73] (**Extended Data Fig. 2e**). These
176 NOD-like receptor homologs localize to the subcortical maternal complex and are thought to regulate the oocyte-
177 to-embryo transition[74,75], though their role is under debate[75]. Furthermore, these changes are consistent across
178 follicle types enclosing the oocytes, suggesting that these trends are not driven by changes in the follicular
179 composition with age (**Extended Data Fig. 2f**). Together, our results indicate that aging may disrupt the integration
180 of external signals that guide oocyte maturation, suggesting a potential mechanistic basis for age-related decline in
181 oocyte quality.
182
183 ***Molecular programs define spatially organized follicle lifecycles in young ovaries***
184 Oocyte maturation occurs in concert with dynamic remodeling of surrounding granulosa cells. To characterize this
185 organization, we systematically compared GC states across hundreds of follicles in young ovaries by quantifying
186 cell states as a function of scaled radial distance from the follicle center, revealing extensive intra-follicle
187 heterogeneity (**Fig. 3a, b**; **Extended Data Fig. 3a**; **Methods**). Cell cycle analysis and diffusion pseudotime (DPT)
188 analysis of GC trajectories toward their two terminal fates, luteinization or atresia, revealed that proliferating GCs
189 are enriched near the follicle center, whereas differentiated GCs with higher pseudotime localize to the periphery,
190 consistent with literature that proximity to the theca-granulosa boundary influences specialization (**Fig. 3c,d;**
191 **Extended Data Fig. 3b,c**; **Methods**). Immunostaining confirmed these patterns, with *Ki67* marking proliferative

192 GCs near the center and *Cyp19a1* labeling mature GCs at the periphery (**Fig. 3e,f**). To further identify spatially
193 organized transcriptional patterns, we applied consensus non-negative matrix factorization (cNMF)[76] to identify co-
194 expressed GC gene expression programs (GEPs) and mapped their spatial distribution (**Extended Data Fig. 3d,e,f**).
195 In non-atretic follicles, a GC maturation program (GEP2; *Inhbb*, *Fst*) localized centrally, while a luteinization
196 program (GEP1; *Hsd3b1*, *Lhcgr*, *Mro*) was enriched at the periphery (**Fig. 3g**). This compartmentalization was
197 disrupted in atretic follicles, which showed globally reduced expression of both programs. Altogether, our findings
198 indicate that granulosa cells maintain a spatial division of labor balancing proliferation and differentiation during
199 follicle development, which is lost with atresia.
200
201 ***Aging disrupts the temporal trajectory of GC differentiation***
202 We next examined how GCs utilize GEPs across their differentiation trajectory, spatial context, estrous stage, and
203 reproductive age by ordering usage profiles by diffusion pseudotime to better visualize usage patterns (**Fig. 3h**;
204 **Extended Data Fig. 3e,g,h**). In young, non-atretic follicles, GEP usage followed the expected sequence of
205 folliculogenesis defined by canonical markers. For instance, GCs in preantral follicles during estrus exhibited high
206 usage of an early development program GEP9 (*Wt1, Wnt4*) but low activity of proliferative GEP3 (*Top2a*, *Mki67*)
207 and follicular dominance GEPs 2 and 4 (*Inhbb*, *Fst*; *Esr2*, *Greb1l*). By contrast, GCs in luteinizing follicles showed
208 increased activity of the follicular dominance GEPs as well as the luteinization GEP1 (*Lhcgr*, *Hsd3b1*), particularly
209 during metestrus, while atretic follicles expressed apoptosis-associated GEPs 10, 11 (*Thbs1*, *Pik3ip1*; *Ghr, Ptprd*)
210 (**Fig. 3h, Extended Data Fig. 3f,g**). In aged ovaries, this orderly transcriptional trajectory was significantly altered.
211 In non-atretic follicles, expression of early development (GEP9) decreased, follicular dominance and luteinization
212 (GEP2, 1) lost stage specificity, and an apoptosis-associated program (GEP10) was elevated (**Fig. 3h**,**i**; **Extended**
213 **Data Fig. 3g,h**). Notably, GCs in atretic follicles were the most affected by aging, with downregulation of canonical
214 apoptosis-associated (GEP10, 11) and proliferation (GEP3) modules but aberrant upregulation of the extracellular
215 matrix (ECM) remodeling program (GEP6; *Col1a2*, *Lama2*) typically confined to preantral follicles in young
216 animals. These patterns suggest a shift from regulated cell to dysregulated remodeling, blurring developmental and
217 degenerative boundaries in aged follicles. Together, these results indicate that aging disrupts the defined temporal
218 sequence of GC differentiation and impairs the regulation of follicle atresia.
219
220 ***Aging alters the progression of follicular atresia***
221 Given the pronounced transcriptional alterations in atretic follicles, we next conducted a deeper investigation of
222 atretic GC heterogeneity and progression. Subclustering atretic GCs revealed three states (**Fig. 3j**): state 1, marked
223 by metabolic reprogramming (*Cdk8*, *Hexb*, *Hsd3b1*, *Tpt1*)[77–81]; state 2, enriched for oxidative stress response and
224 matrix remodeling (*Clu*, *Gpx3, Sparc*, *Col1a2*)[82–84]; and state 3, defined by apoptotic and immune-modulatory
225 signatures (*Foxo1*, *Ghr*, *Pik3ip1*, *Cfh*, *Cd47*)[85–89]. While analysis from transcriptomic snapshots cannot confirm
226 developmental origins and trajectories, we performed partition-based graph abstraction (PAGA) to infer how
227 different GC states relate to each other and found that transitions to atretic GC may arise from multiple non-atretic

228 GC states, most strongly from antral early GCs, consistent with the high rates of follicular atresia before dominant
229 follicle selection[90,91] (**Fig. 3k**). Furthermore, pseudotime analysis suggested a trajectory from state 1 to state 3 (**Fig.**
230 **3l**), supported by the observation that states 1 and 2 were enriched in immature follicles, whereas state 3
231 predominated in mature and fully atretic follicles. These distributions suggest a progression from early metabolic
232 reprogramming through stress and ECM remodeling to terminal apoptosis, transitioning from early atretic subtypes
233 in estrus to late apoptotic populations in metestrus (**Fig. 3m**).
234
235 Aging disrupted atretic progression. Across all follicle types, we observed a decrease in terminal apoptotic and
236 immuno-modulatory GC atretic 3 in aged ovaries (**Fig. 3m**). This failure to transition to the terminal atretic state
237 was accompanied by upregulation of genes associated with the complement system, reduced levels of the
238 phagocytosis inhibitor "don't-eat-me-signal" *Cd47* (**Extended Data Fig. 3i**). Together, these findings suggest that
239 effective atresia requires a coordinated transition to an apoptotic, immune-active state that promotes follicular
240 clearance, and that aging impairs this process, potentially leading to unresolved atresia, chronic inflammation, and
241 accumulation of follicular debris in the aged ovary.
242
243 ***Multicellular dynamics and interactions shaping folliculogenesis progression***
244 Folliculogenesis progresses through coordinated interactions among multiple cell types, extending beyond cell-
245 autonomous granulosa programs. To resolve this higher-order organization (**Fig. 4a**), we arranged follicle segments
246 from reproductively young mice along a computationally inferred folliculogenesis trajectory (**Fig. 4b,c**). Pairwise
247 distributional distances between segments, calculated using the Wasserstein distance[92] (**Fig. 4b,c**), enabled
248 clustering of follicles and corpora lutea by multicellular similarity, visualized in a UMAP embedding (**Fig. 4d**;
249 **Extended Data Fig. 4a**; **Methods**). Diffusion pseudotime analysis recovered the expected transitions from preantral
250 to antral or atretic follicles (**Fig. 4e**), accompanied by gradual shifts in cell type composition (**Extended Data Fig.**
251 **4b**). To examine how compositional changes were reflected in cell-cell communication, we applied
252 MultiNicheNet[93] to infer receptor-ligand interactions among oocytes, granulosa, theca, and immune cells across
253 preantral, antral, and atretic follicles, treating each follicle as a sample (**Methods**; **Extended Data Fig. 4c**). Follicle
254 stage-specific interactions included *Gdf9-Fxyd6* between oocytes and GCs in preantral follicles, *Fst-Bmpr1b*
255 between GCs and theca cells in antral follicles, and *Apoa4-Lrp1* within GCs in atretic follicles. Receptor-ligand
256 interaction scores varied smoothly across the folliculogenesis trajectory (**Fig. 4f**; **Methods**). The candidate atretic
257 interaction, *Apoa4-Lrp1*, suggests follicle metabolic reprogramming, as *Lrp1* (low-density lipoprotein receptor-
258 related protein 1) regulates lipid transport and glucose metabolism[94,95], while *Apoa4* promotes lipid metabolism,
259 and their interaction facilitates glucose uptake[96]. Notably, *LRP1* has been genetically linked to polycystic ovarian
260 syndrome (PCOS), a disorder characterized by metabolic and hormonal dysfunction[97].
261
262 ***Temporal coupling in follicle activation, maturation, and hormone sensing***

263 Although all follicles in the ovary experience the same systemic hormones, they progress asynchronously through
264 distinct developmental states across the estrous cycle. We therefore analyzed how follicle populations of different
265 stages coexist across the cycle in reproductively young mice. In metestrus, the proportion of preantral follicles was
266 significantly lower compared to estrus (**Fig. 4g**; P=0.001, two-tailed t-test). This shift likely reflects an increase in
267 antral and atretic follicles at metestrus, as preantral follicle numbers remain largely stable across the cycle, while
268 larger follicles expand[98–101]. Furthermore, this change is likely not attributed to differential preantral atresia, since
269 death rates of small follicles remain constant[99,101]. To assess how follicle maturation progresses across the cycle, we
270 compared antral follicle features between estrus and metestrus. The hormonal dynamics preceding estrus are critical:
271 surges in follicle-stimulating hormone (FSH) and luteinizing hormone (LH) trigger competition among antral
272 follicles for dominance, driving them toward either ovulation or atresia such that mature antral follicles are typically
273 depleted by estrus[100–104]. Consistent with this, antral mitotic follicles were significantly smaller during estrus than
274 metestrus (**Extended Data Fig. 4d;** P=0.001, two-tailed t-test) and exhibited lower pseudotime values, indicating
275 a less mature state (**Fig. 4h**; **Extended Data Fig. 4e;** P=0.002, two-tailed t-test). Functionally, antral follicles at
276 estrus showed reduced expression of the gonadotropin receptors *Lhcgr* and *Fshr* (**Fig. 4i**; *P<0.01, **P<0.001, two-
277 tailed t-test), suggesting that they are in an immature, non-hormone-responsive state, possibly due to their recent
278 transition from the gonadotropin-independent preantral state[14].
279
280 ***Aging disrupts homeostatic temporal coupling***
281 The coordinated timing of follicle maturation and hormone responsiveness in young mice prompted us to ask how
282 this coupling changes with age. A hallmark of ovarian aging is the onset of irregular cycling, as observed during
283 perimenopause in humans, indicating disrupted temporal regulation of endocrine signaling and ovarian
284 function[105,106]. Although the reproductively aged mice in our study were cycling, their molecular profiles revealed
285 a loss of temporal coordination observed in young mice. Unlike young mice, old mice showed no stage-dependent
286 shifts in preantral follicle composition and antral follicle size (**Fig. 4j**; P=0.942, two-tailed t-test; **Extended Data**
287 **Fig. 4f**). Projecting follicles from old mice onto the reference trajectory of young mice revealed a distortion in
288 pseudotime distribution, showing no significant distinction between estrus and metestrus (**Fig. 4k**; P=0.677, two-
289 tailed t-test; **Extended Data Fig. 4e,g**; **Methods**). Consistently, *Fshr* and *Lhcgr* expression within antral follicles
290 did not vary across stages in old mice (**Fig. 4l**). In young ovaries, gonadotropins synchronize follicle cohorts to
291 ensure coordinated progression toward ovulation or atresia, yielding immature antral follicles at estrus. By contrast,
292 old ovaries had larger, more mature follicles at estrus, consistent with disrupted follicle development. While reduced
293 follicle numbers in old ovaries limit statistical power, the consistent absence of stage-dependent differences in
294 follicle composition, pseudotime, and hormone receptor expression suggests that temporal regulation of
295 folliculogenesis becomes uncoupled from the estrous cycle with age, preceding acyclicity and reproductive
296 senescence.
297
298 ***Temporal dysregulation of corpus luteum clearance in aged ovaries***

299 We next examined whether the corpus luteum dynamics are also altered with age. Of note, we observed two spatially
300 segregated luteal cell populations with opposing progesterone regulatory programs (**Fig. 5a, Extended Data Fig.**
301 **5a**)[107]. Marked by *Parm1* and *Akr1c18*, these populations correspond to known luteal subtypes previously attributed
302 to granulosa and theca origins[108,109] (**Extended Data Fig. 5b)**. However, our data suggest that these populations
303 reflect a temporal phenotypic switch during the CL lifecycle (**Extended Data Fig. 5c**)[37]. *Parm1*-enriched CLs ('CL
304 – Parm1') express progesterone synthesis genes, contain vascular endothelial cells, are enriched at estrus, and
305 consist of smaller histologically[110,111], features consistent with newly formed, hormonally active structures
306 (**Extended Data Fig. 5a-e**)[19,37,107,112,113]. In contrast, *Akr1c18*-enriched CLs ('CL – Akr1c18') express the regression
307 marker prostaglandin F receptor *Ptgfr*, infiltrated by immune cells, more frequent at metestrus, and contain
308 histologically larger cells[110,111], features indicating a regression state (**Extended Data Fig. 5a-f**). In aged ovaries,
309 while we find the transcriptional identities of the luteal cells are maintained (**Extended Data Fig. 5g**), *Akr1c18* CLs
310 abnormally accumulated at estrus (**Fig. 5b**, P=0.006, two-tailed t-test). Because timely CL clearance and
311 accompanying drop in progesterone are required to initiate the next cycle[19,104,113], persistence of these degenerating
312 CLs likely disrupts progesterone homeostasis, potentially impairing normal cycle progression[4,14].
313
314 Investigating the molecular aberrations in persistent CLs revealed dysregulated inflammatory and luteolysis
315 signaling with age. Under homeostatic conditions, immune cells accumulate in *Akr1c18* CLs at metestrus to
316 facilitate tissue clearance during luteolysis[12] (**Fig. 5c**). In aged ovaries, immune infiltration was significantly
317 elevated in *Akr1c18* CLs at metestrus (**Fig. 5d**; **Extended Data Fig. 5h**; P<0.005, two-tailed t-test). Furthermore,
318 aged *Akr1c18* CLs failed to upregulate the prolactin receptor *Prlr* and the prostaglandin receptor *Ptgfr* (**Fig. 5e**),
319 which normally trigger luteolysis, but instead showed elevated expression of the immune-recruiting chemokine
320 *Ccl2*, along with pro-inflammatory cytokines *Il1b* and *Ccl3*[33,38,39] (**Fig. 5f**; **Extended Data Fig.** 5i). Across ovarian
321 compartments, immune populations increased most prominently within CLs, implicating defective CL clearance as
322 a major driver of inflammaging (**Fig. 5g**). Altogether, our findings indicate that aged CLs exhibit dysregulation of
323 prolactin- and prostaglandin- mediated regression, leading to persistent CLs that sustain inflammation and
324 contribute to endocrine decline.
325
326 ***Global immune compositional changes define age-associated inflammation***
327 As impaired tissue clearance and chronic inflammation are major hallmarks of ovarian aging[10,33], we sought to
328 closely examine the functional and spatial dynamics of immune populations. We identified four macrophage
329 subsets, along with dendritic cells, mast cells, plasma cells, and T cells with distinct spatial localization within
330 tissues (**Fig. 6a,b**; **Methods**). The macrophage subsets included canonical phagocytic (Macrophage 1: *Cd36*,
331 *Mmp12*), antigen-presenting (Macrophage 2: *Cd74*, *H2-Aa*, *S100a4/6*), efferocytic/repair (Macrophage 3: *Mrc1*,
332 *Stab1*, *Mertk*), and metabolically active (Macrophage 4: *Acsbg1*, *Adh1*) populations. Phagocytic and antigen-
333 presenting macrophages (Macrophages 1 and 2) were the most abundant and expanded significantly with age (**Fig.**
334 **6b**). Spatial mapping revealed that the most significant accumulation in immune cells occurred in preantral and

335 atretic follicles and CLs (**Fig. 6c**). Across all ages, phagocytic macrophages (Macrophage 1) localized to the
336 periphery, while antigen-presenting macrophages (Macrophage 2) were enriched at the core, suggesting their key
337 role in inflammaging (**Fig. 6d,e**). This pattern was accentuated in aged ovaries, which showed a general trend
338 towards greater immune infiltration towards the segment center (**Fig. 6d**). Immunofluorescence of a regressing CL
339 revealed CD11b+ macrophages and CD3+ T cells at the CL center, supporting the likely role of antigen presentation
340 in CL clearance (**Fig. 6f**). Although low in abundance, T cells expand in CLs of aged ovaries, which may be the
341 functional site of prior reports of cytotoxic and double negative T cell accumulation in the aging ovary[39]. Altogether,
342 spatial profiling highlights age-related immune infiltration within ovarian structures, with phagocytic and antigen-
343 presenting macrophages showing particularly strong enrichment in atretic and luteinizing follicles.
344
345 A hallmark of ovarian aging is the accumulation of multinucleated giant cells (MNGCs), which reflect chronic
346 inflammation and are associated with fibrosis[11,33,114,115]. MNGCs, visible as clusters of fused cells on H&E stains,
347 increased markedly with age (**Fig. 7a,b**; **Extended Data Fig. 6a**). To define their molecular features, we performed
348 image registration between adjacent pairs of H&E images and Slide-seq pucks using anatomical landmarks to
349 identify immune spots located within *vs* outside of MNGCs (**Fig. 7c**; **Extended Data Fig. 6b; Methods**).
350 Macrophages (four distinct subsets), particularly the phagocytic subtype (Macrophage 1), were the predominant
351 immune population enriched within MNGCs (**Fig. 7d**). Differential expression analysis revealed distinct
352 transcriptional shifts in MNGC-associated macrophages (**Extended Data Fig. 6c**). Phagocytic macrophages
353 (Macrophage 1) upregulated ribosomal and proliferative genes (*Rps24*, *Cdk11c*) while downregulating chemokines
354 (*Ccl6*, *Ccl9*) and *Spp1*, suggesting reduced immune signaling (**Fig. 7e**). Antigen-presenting macrophages
355 (Macrophage 2) upregulated complement (*C3*), fusion-related genes (*Tagln*, *Acta2*), and *Itgae* (CD103), consistent
356 with a tissue-resident state. Efferocytic/repair macrophages (Macrophage 3) upregulated clearance and lysosomal
357 genes (*Gpnmb*, *Mfge8*, *Ctsd*) but reduced *Adgre1* (F4/80). Metabolically active macrophages (Macrophage 4)
358 expressed higher levels of inflammatory and lipid regulators (*Pla2g7*, *Lyz2*, *Lgals3*). Together, these findings show
359 that macrophages within MNGCs adopt specialized transcriptional programs distinct from those in the surrounding
360 stroma, reflecting coordinated roles in cell fusion, complement activation, efferocytosis, and metabolic remodeling.
361
362 Ovarian aging is marked by global shifts in tissue composition and function, including increased inflammation that
363 may broadly impair tissue homeostasis[11,116]. We examined alterations in the stroma, including all cell types located
364 predominately outside of follicles and corpora lutea. Analysis of stromal cell populations revealed an age-associated
365 increase in surface epithelial and immune cells, coupled with a decline in steroidogenic stromal cells, progressing
366 monotonically from young to middle-aged and old mice[10,116–119] (**Fig. 7f**; compositional test with scCODA[120];
367 **Extended Data Fig. 6d**; **Methods**). The thickening of the surface epithelium was independently confirmed by
368 morphometric measurements on adjacent H&E sections (**Extended Data Fig. 6e**; **Methods**). These compositional
369 shifts coincided with transcriptional changes characterized by reduced expression of extracellular matrix genes,
370 increased metalloproteases involved in tissue remodeling, and elevated markers of fibrosis and inflammation[116]

371 (**Fig. 7g; Extended Data Fig. 6f**). Together, these changes suggest that aging disrupts immune-mediated
372 maintenance of stromal homeostasis, promoting chronic inflammation and fibrosis within the ovarian
373 microenvironment.
374
375 ***A model for global tissue disorganization in ovarian aging***
376 We hypothesized that age-related remodeling of the ovarian stroma during disrupt coordination between follicles.
377 To test this, we quantified the spatial co-localization of homotypic follicles, i.e. those of the same follicle
378 developmental stage. At short length scales (<500 μm), both preantral and atretic follicles were highly co-localized
379 in young but not aged mice (**Fig. 7h**; **Methods**), consistent with prior reports that follicle crowding facilitates early
380 activation and preantral development[121,122]. The loss of preantral clustering with age likely reflects, in part, increased
381 extracellular matrix rigidity[9,11,116]. Co-localization of atretic follicles in young ovaries suggests a role for spatially
382 regulated paracrine signaling during follicle selection, potentially influenced by the dominant follicle. In contrast,
383 antral follicles did not co-localize at short length scales in either young or old mice, consistent with their function
384 as isolated "islands" of dominant follicles during selection. Modest co-localization at larger scales (> 2,000 μm) in
385 both young and old mice may simply reflect the overall larger size of the ovary in young mice (~3,000 μm in total
386 diameter). Together, these data reveal that ovarian aging reduces follicular crowding, disrupting the spatial
387 coordination of follicle development and interfollicular communication.
388
389 The loss of global spatial organization in aged ovaries suggests that inflammation disrupts both individual follicle
390 function and their coordinated development, marking molecular hallmarks of ovarian aging across cells, niches and
391 the entire tissue (**Fig. 7i**). At the cellular level, oocytes function declines as the number of maturing oocytes
392 decreases and their transcriptional states shift with age. These changes are compounded by alterations in
393 surrounding niches: inflammatory gene expression increases within follicles, and their responsiveness to the estrous
394 cycle diminishes. In old mice, this is reflected by preantral follicles that no longer vary by cycle stage and by the
395 accumulation of late corpora lutea due to defective clearance. At the organ level, the surface epithelium thickens,
396 and the stroma becomes dominated by chronic inflammation and multinucleated giant cells. Together, these findings
397 show that age-related inflammation progressively erodes ovarian organization and remodeling across multiple
398 spatial scales, from cells and niches to the whole organ.
399
400 **Discussion**
401 Here, we present a 10μm-resolution, >600,000 spot spatial transcriptomic atlas of the naturally cycling murine
402 ovary across reproductive ages, revealing that aging disrupts the spatial and temporal coordination of the ovarian
403 tissue environment across multiple scales. Aging attenuates oocyte transcriptional programs, erodes the spatial
404 polarity of granulosa cells, and alters the timing of follicle maturation and CL clearance. These changes coincide
405 with increased immune infiltration, MNGC formation, and loss of global tissue coordination, collectively defining
406 ovarian aging as a progressive tissue-wide breakdown of spatiotemporal regulation rather than a singular decline in

407 oocyte number or quality. The extended presence of CLs expressing progesterone-metabolizing and immune
408 recruitment genes coupled with an expansion of infiltrating immune cells may trigger chronic inflammation, while
409 the emergence of MNGCs containing immune cells with altered signaling marks a shift to sustained inflammatory
410 and lipid-associated activity. In parallel, loss of spatial coupling between neighboring follicles suggests that
411 extracellular matrix remodeling and paracrine signaling required for coordinated development deteriorate with age.
412 Together, these changes precede the cessation of cycling, propagating local follicular and luteal spatiotemporal
413 regulation into global tissue disorganization, representing early molecular and structural hallmarks of reproductive
414 aging.
415
416 During each estrous cycle, numerous follicles compete for dominance and ovulation, with the majority undergoing
417 atresia. The spatial organization of GCs within follicles may represent an elegant mechanism to efficiently compete
418 for metabolic resources while sustaining coordinated growth. By segregating proliferative activity to inner GCs and
419 hormone-sensing, steroidogenic functions to outer GCs positioned near the vasculature and stroma, follicles
420 optimize resource allocation under the energetic constraints of this competitive environment. We hypothesize that
421 the success of spatial compartmentalization of GC function during folliculogenesis could contribute to follicular
422 fate, with dominant follicles effectively maintaining functional polarity while less efficient competitors undergo
423 atresia[123,124]. In addition, our results support and refine current understanding of follicular atresia as a heterogeneous
424 process that can arise at multiple follicular stages. We identified engagement of metabolic reprogramming, stress
425 response, extracellular matrix remodeling, and immune-modulatory pathways as well as apoptotic pathways that
426 are concentrated at the follicle edge and vary with follicle state and estrous cycle context. While our results outline
427 a plausible sequence of atresia commitment arising from multiple GC lineages, the specific molecular drivers
428 require experimental validation[17,125–127].
429
430 Our findings highlight the critical role of temporal coordination in ovarian function. While the ovulation cycle is
431 often viewed primarily as a mechanism for oocyte release, our results highlight the tissue-wide remodeling
432 required for successful cycling. In young mice, these processes are tightly coupled to the estrous cycle, reflecting
433 finely tuned synchronization between local follicular processes and systemic endocrine signals consistent with
434 previous reports[98–101,103,104]. With age, however, this temporal pattern deteriorates: follicles lose stage-and follicle-
435 type restricted expression of folliculogenesis and atretic pathways and CLs persist across stages with altered
436 expression in progesterone metabolism. This mirrors luteal-phase changes described in perimenopausal women
437 and suggests that reproductive aging manifests as a breakdown in cyclical synchronization between local tissue
438 dynamics and systemic hormonal rhythms. We note that these multicellular features of reproductive function in
439 young mice and their progressive dysfunction in old mice are exceptionally dynamic with an estrous cycle length
440 of only four days, allowing spatial transcriptomics to capture snapshots of meaningful niche transitions that
441 describe changes across multiple scales, from radial heterogeneity within follicles, to variation across follicles,
442 and spatial patterns of follicle co-localization that underscore the importance of interfollicular coordination.

These results have potential implications for understanding and mitigating human reproductive aging, which remains challenging to profile at scale and high temporal resolution. The observation that spatial and temporal coordination break down before cycle cessation suggests new approaches for detecting and potentially intervening in age-related fertility decline. Additionally, the role of tissue-wide organization in maintaining function suggests that therapeutic strategies may need to target the entire ovarian environment rather than focusing solely on oocytes or follicles.

Several key questions requiring targeted perturbation and ability to track follicular fate emerge from our findings. How do GCs maintain distinct functional zones despite their high proliferation rate? Would improved compartmentalization alter atresia? What signals coordinate states between neighboring follicles? How are atretic GCs, regressing luteal cells and infiltrating immune cells cleared from the tissue? Would interventions targeting cellular turnover or inflammatory pathways preserve ovarian function with age? Understanding these mechanisms could reveal new principles of tissue remodeling relevant not only for ovarian function but also regeneration and aging in other contexts.

We acknowledge several limitations in our study. While spatial transcriptomics provides unprecedented insights into tissue organization, we lack direct observation of fate decisions and cannot pinpoint the exact step at which follicles commit to atresia, which follicles contain successfully ovulated oocytes, or the age of a corpus luteum. Future studies integrating lineage tracing and hormone measurements across the full estrous cycle would provide a more complete picture of ovarian temporal dynamics and their changes with aging. Additionally, validation in human tissue will be important for translating these findings into clinical applications.

Here we demonstrate that ovarian function requires precisely coordinated spatial and temporal organization across multiple scales, from cell-type specific patterning within follicles, stage specific coordination of follicles and CLs, to tissue-wide cellular remodeling. Spatial transcriptomics technologies can capture meaningful multicellular transitions if carefully analyzed, positioning this methodology as a key instrument to derive mechanistic insights into reproductive function and decline, opening new avenues for preserving fertility and ovarian endocrine function.

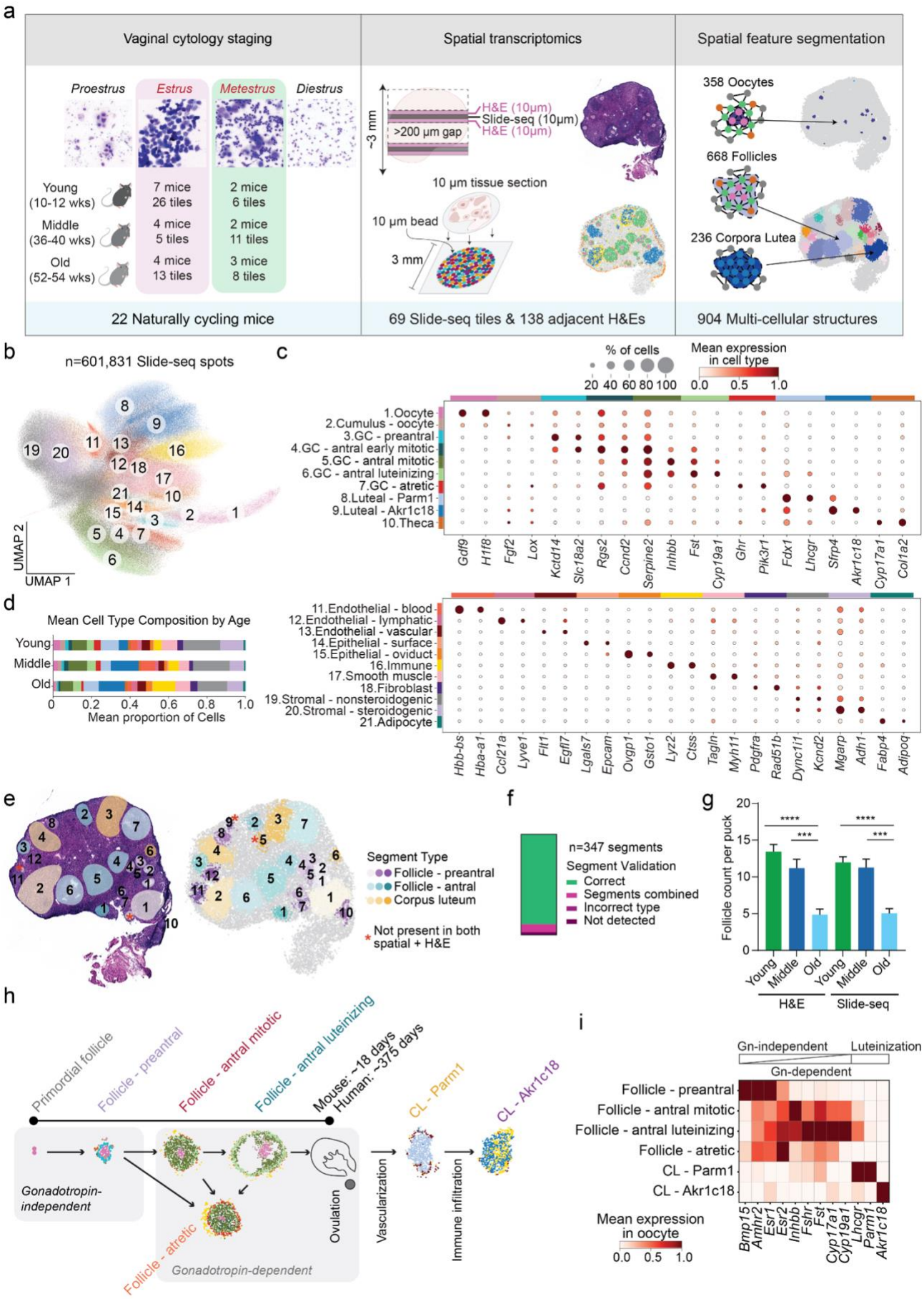
a
Vaginal cytology staging
Spatial transcriptomics
Spatial feature segmentation
Proestrus
Estrus
Metestrus
Diestrus
Young (10-12 wks)
Middle (36-40 wks)
Old (52-54 wks)
7 mice 26 tiles
4 mice 5 tiles
4 mice 13 tiles
2 mice 6 tiles
2 mice 11 tiles
3 mice 8 tiles
~3 mm
>200 µm gap
H&E (10µm)
Slide-seq (10µm)
H&E (10µm)
10 µm tissue section
10 µm bead
3 mm
358 Oocytes
668 Follicles
236 Corpora Lutea
22 Naturally cycling mice
69 Slide-seq tiles & 138 adjacent H&Es
904 Multi-cellular structures
b
n=601,831 Slide-seq spots
UMAP 2
UMAP 1
c
% of cells
20 40 60 80 100
Mean expression in cell type
0.0 0.5 1.0
1.Oocyte
2.Cumulus - oocyte
3.GC - preantral
4.GC - antral early mitotic
5.GC - antral mitotic
6.GC - antral luteinizing
7.GC - atretic
8.Luteal - Parm1
9.Luteal - Akr1c18
10.Theca
Gdf9 H1f8 Fgf2 Lox Kctd14 Slc18a2 Rgs2 Ccnd2 Serpine2 Inhbb Fst Cyp19a1 Ghr Plk3r1 Fdx1 Lhcgr Sfrp4 Akr1c18 Cyp17a1 Col1a2
d
Mean Cell Type Composition by Age
Young
Middle
Old
0 0.2 0.4 0.6 0.8 1.0
Mean proportion of Cells
11.Endothelial - blood
12.Endothelial - lymphatic
13.Endothelial - vascular
14.Epithelial - surface
15.Epithelial - oviduct
16.Immune
17.Smooth muscle
18.Fibroblast
19.Stromal - nonsteroidogenic
20.Stromal - steroidogenic
21.Adipocyte
Hbb-bs Hba-a1 Ccl21a Lyve1 Flt1 Egfl7 Lgals7 Epcam Ovgp1 Gsto1 Lyz2 Ctss Tagln Myh11 Pdgfra Rad51b Dync1i1 Kcnd2 Mgarp Adh1 Fabp4 Adipoq
e
Segment Type
Follicle - preantral
Follicle - antral
Corpus luteum
Not present in both spatial + H&E
f
n=347 segments
Segment Validation
Correct
Segments combined
Incorrect type
Not detected
g
Follicle count per puck
0 5 10 15 20
****
***
Young Middle Old Young Middle Old
H&E
Slide-seq
h
Primordial follicle
Follicle - preantral
Follicle - antral mitotic
Follicle - antral luteinizing
Mouse: ~18 days
Human: ~375 days
CL - Parm1
CL - Akr1c18
Gonadotropin-independent
Follicle - atretic
Gonadotropin-dependent
Ovulation
Vascularization
Immune infiltration
i
Gn-independent
Luteinization
Gn-dependent
Follicle - preantral
Follicle - antral mitotic
Follicle - antral luteinizing
Follicle - atretic
CL - Parm1
CL - Akr1c18
Mean expression in oocyte
0.0 0.5 1.0
Bmp15 Amhr2 Esr1 Esr2 Inhbb Fshr Fst Cyp17a1 Cyp19a1 Lhcgr Parm1 Akr1c18

472 **Figure 1. A spatiotemporal map of the cycling and aging ovary identifies spatial niches driving**
473 **folliculogenesis.**
474 **a.** Overview of experimental design. Mice were staged via vaginal cytology and harvested from estrus and metestrus
475 stages (*n*=22; young 10-12 weeks, middle 36-40 weeks, old 52-54 weeks). Multiple non-adjacent sections (10 µm
476 thickness) were profiled using Slide-seq from each ovary with a minimum gap of 200 µm to avoid resampling the
477 same follicle or CL structure. Adjacent sections were taken for histological analysis. After clustering and cell type
478 annotation, multicellular segments were defined with an automated segmentation pipeline.
479 **b.** UMAP embedding of RNA profiles (dots) captured by Slide-seq spots (n=610,620; each at 10 µm resolution)
480 across 69 Slide-seq pucks (**Methods**). Spots colored by post hoc annotation (color legend). "GC": granulosa cell.
481 **c.** Mean expression (log normalized counts, dot color) and proportion of expressing cells (dot size) of marker genes
482 (columns) used for annotating cell type clusters (rows).
483 **d.** Mean cell type composition across young (*n*=32), middle (*n*=16), and old (*n*=21) pucks.
484 **e.** Representative H&E sections and corresponding spatial segment maps showing annotated preantral follicles
485 (purple), antral follicles (green-blue), and corpora lutea (yellow). Asterisks denote segment structures only present
486 in either H&E or Slide-seq sections due to sampling, rather than an error of the segmentation.
487 **f.** Quantification of segmentation accuracy across *n*=347 segments where an adjacent H&E section was present to
488 validate with, the majority (*n*=311) were correct. Error types included segments that were grouped with another
489 object in the pipeline, segments where the incorrect type was assigned, and segments that were not detected by the
490 pipeline. Cohen's kappa=0.85.
491 **g.** Mean follicle counts of adjacent H&E sections and Slide-seq segmentation across young (*n*=32), middle (*n*=16),
492 and old (*n*=21) pucks. Error bars: SEM (***$P<0.001$, ****$P<0.0001$ two-tailed t-test; all other bar groups, not
493 significant).
494 **h.** Schematic of folliculogenesis and CL formation. GCs form a single layer around a dormant oocyte in primordial
495 follicles. Activation triggers GCs to proliferate, forming the preantral follicle. The follicle then transitions to the
496 gonadotropin-dependent antral stage during which a fluid-filled cavity forms the antrum. Theca cells are recruited
497 to create an outer layer, and GCs differentiate into multiple subtypes. Follicle atresia can occur during any stage of
498 folliculogenesis. After ovulation, GCs luteinize into luteal cells that form the CL, which is subsequently cleared
499 from the tissue.
500 **i.** Mean expression (log normalized counts and variance-scaled) of key hormone receptors and synthesis genes
501 (columns) across segment types (rows), grouped by gonadotropin-independent, gonadotropin-dependent, and
502 luteinization stages. Segment counts: preantral (*n*=238), antral mitotic (*n*=191), antral luteinizing (*n*=43), atretic
503 (*n*=181), CL - Parm1 (*n*=87), CL - Akr1c18 (*n*=147); *n*=22 mice across all ages.

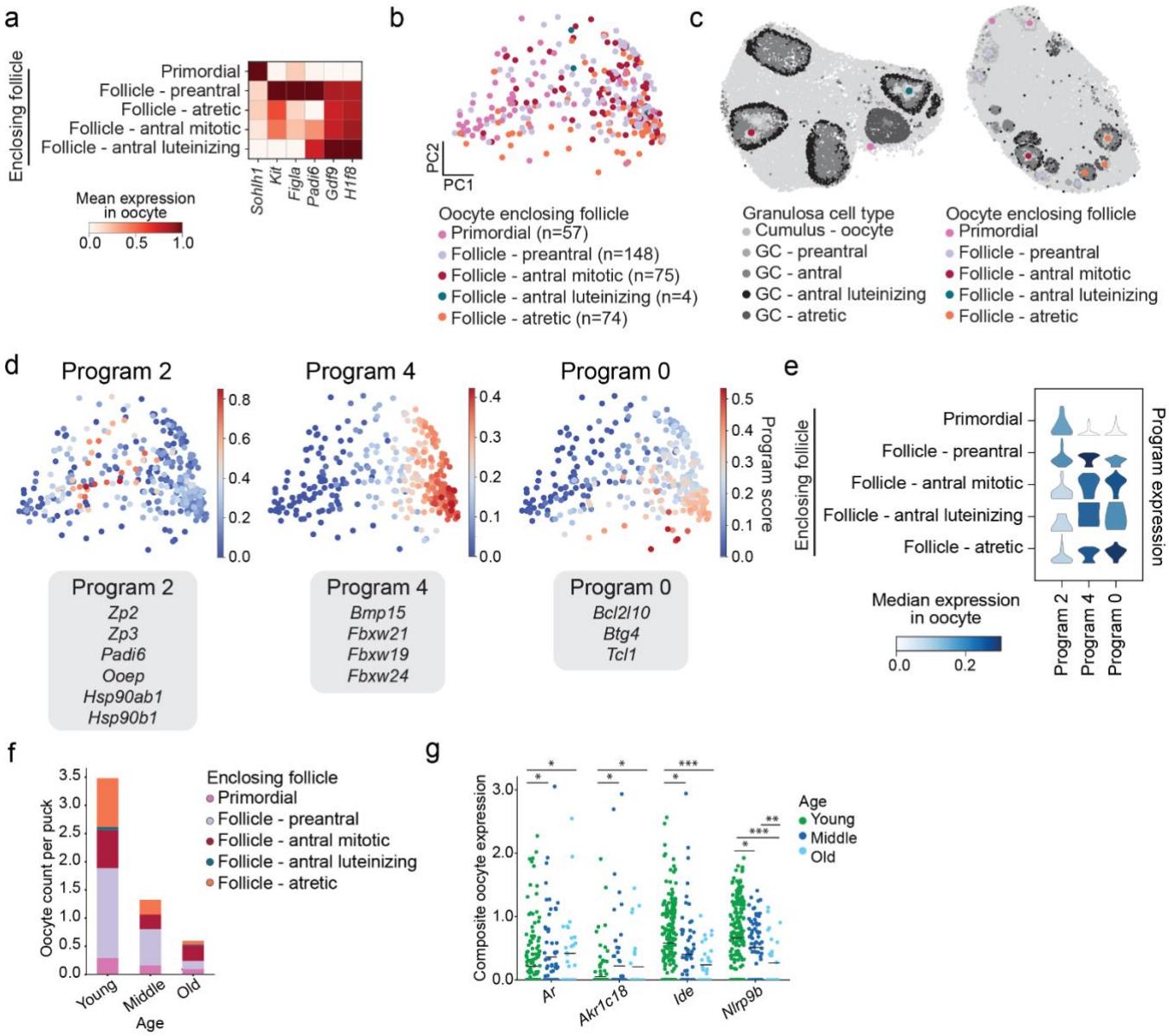

Figure 2. Oocyte transcriptional dynamics across folliculogenesis and age.

a. Mean expression (log normalized counts and variance-scaled) of oocyte marker genes (columns) grouped by the enclosing follicle at different stages of folliculogenesis (rows); *n*=358 oocytes across 22 mice, all age groups. Oocyte counts per follicle type in **Extended Data Table 4**.

b. Principal component (PC) embedding of RNA profiles (dot) indicated by its enclosing follicle stage (color); *n*=358 oocytes across 22 mice, all age groups.

c. Example spatial plots of two pucks showing oocytes (colored dots) in their tissue context depicting the stage of its enclosing follicle (color), with surrounding GC spots (gray).

d. Expression (color) of gene programs identified in oocytes (*n*=358) via non-negative matrix factorization. Top genes contributing to each oocyte gene program, gray text box.

515 **e.** Violin plot of median expression (color) and distribution (kernel density) of oocyte gene programs (columns)
516 across stages of folliculogenesis (rows); *n*=358 oocytes across 22 mice. Oocyte counts per follicle type and age in
517 **Extended Data Table 4**.
518 **f.** Average composite oocyte count per puck (y axis) by enclosing follicle type (color) across age groups (x axis).
519 Oocyte frequencies per age group: young (*n*=229), middle (*n*=89), and old (*n*=40).
520 **g.** Differentially expressed genes of oocytes across age. Select genes (*y* axis) showing significant age-associated
521 changes in oocytes (dots), with colors indicating age; **P*<0.05, ***P*<0.005, ****P*<0.0005, two-tailed t-test,
522 Benjamini-Hochberg correction. Differentially expressed genes were first identified between young and old non-
523 primordial oocytes, then tested pairwise across young, middle, and old to identify monotonic trends. Non-primordial
524 oocyte counts by age in **Extended Data Table 4**.

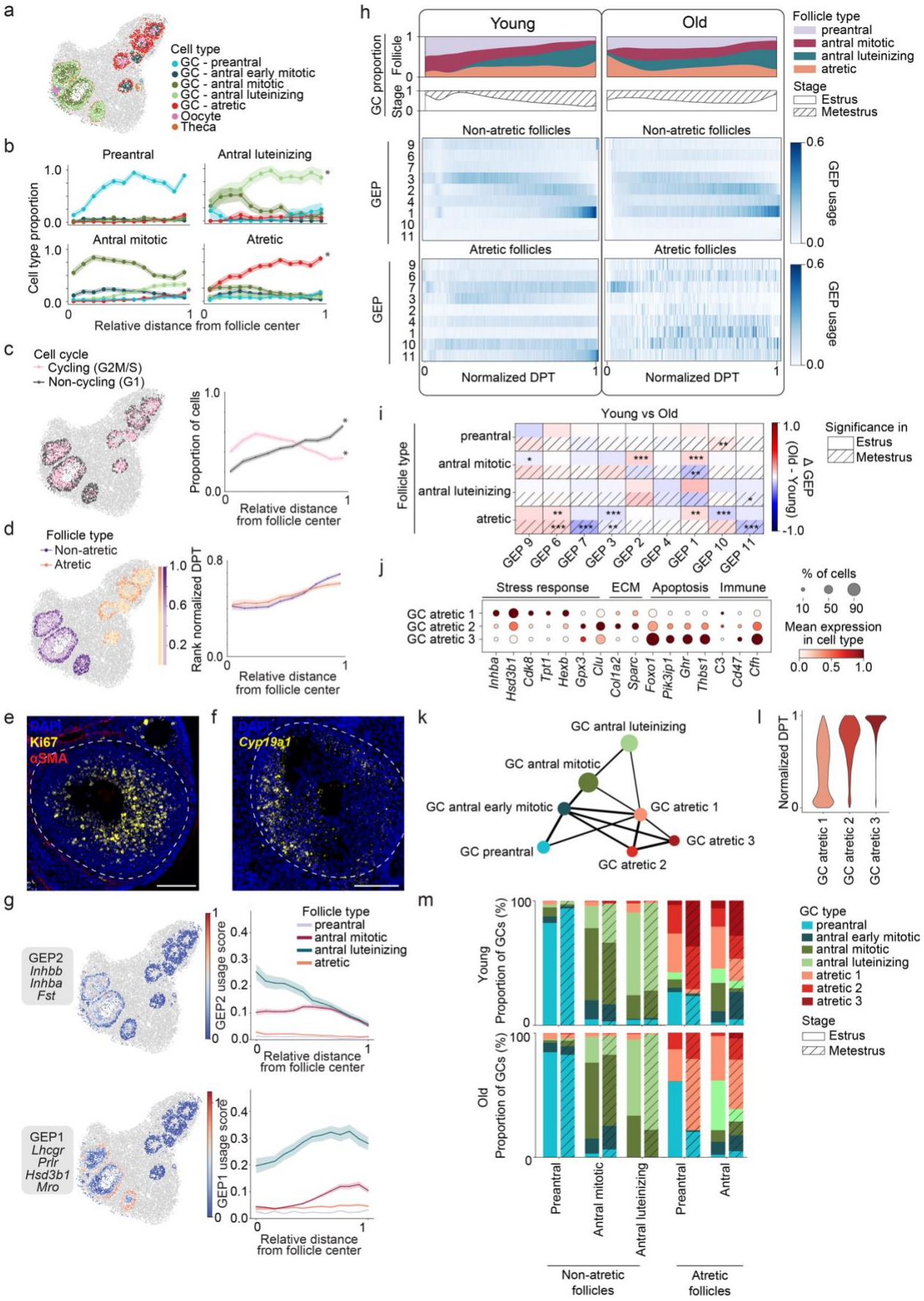
a
Cell type
GC - preantral
GC - antral early mitotic
GC - antral mitotic
GC - antral luteinizing
GC - atretic
Oocyte
Theca
b
Preantral
Antral luteinizing
Antral mitotic
Atretic
Cell type proportion
Relative distance from follicle center
c
Cell cycle
Cycling (G2M/S)
Non-cycling (G1)
Proportion of cells
Relative distance from follicle center
d
Follicle type
Non-atretic
Atretic
Rank normalized DPT
Relative distance from follicle center
e
DAPI
Ki67
αSMA
f
DAPI
Cyp19a1
g
GEP2
Inhbb
Inhba
Fst
GEP2 usage score
Follicle type
preantral
antral mitotic
antral luteinizing
atretic
Relative distance from follicle center
GEP1
Lhcgr
Prlr
Hsd3b1
Mro
GEP1 usage score
Relative distance from follicle center
h
Young
Old
GC proportion
Follicle
Stage
Follicle type
preantral
antral mitotic
antral luteinizing
atretic
Stage
Estrus
Metestrus
Non-atretic follicles
Atretic follicles
GEP
GEP usage
Normalized DPT
i
Young vs Old
Follicle type
preantral
antral mitotic
antral luteinizing
atretic
Δ GEP (Old - Young)
Significance in
Estrus
Metestrus
GEP 9
GEP 6
GEP 7
GEP 3
GEP 2
GEP 4
GEP 1
GEP 10
GEP 11
j
Stress response
ECM
Apoptosis
Immune
GC atretic 1
GC atretic 2
GC atretic 3
Inhba
Hsd3b1
Cdk8
Tpt1
Hexb
Gpx3
Clu
Col1a2
Sparc
Foxo1
Pik3ip1
Ghr
Thbs1
C3
Cd47
Cfh
% of cells
Mean expression in cell type
k
GC antral luteinizing
GC antral mitotic
GC antral early mitotic
GC atretic 1
GC preantral
GC atretic 3
GC atretic 2
l
Normalized DPT
GC atretic 1
GC atretic 2
GC atretic 3
m
Young
Old
Proportion of GCs (%)
GC type
preantral
antral early mitotic
antral mitotic
antral luteinizing
atretic 1
atretic 2
atretic 3
Stage
Estrus
Metestrus
Preantral
Antral mitotic
Antral luteinizing
Preantral
Antral
Non-atretic follicles
Atretic follicles

525

Figure 3. Spatiotemporal coordination of granulosa cells within the follicular niche.

a. Spatial plot of an example puck showing follicular cell types (colors), including preantral, antral early mitotic, antral mitotic, antral luteinizing, and atretic granulosa cell (GC) subtypes, and oocyte and theca.

b. Radial distribution of GC subtypes (colored lines, y axis) across follicle type (panels). Lines show the mean proportion of each subtype across 10 normalized radial bins as a function of the relative radial distance from the center to the edge (x axis; 0 = center, 1 = edge); shading indicates standard error of the mean (SEM) across follicles. Monotonically significant radial trends are indicated (**P*<0.05, Spearman correlation coefficient); *n*=653 total follicles across 22 mice, all age groups. Follicle counts by type in **Extended Data Table 4**.

c. GC cell cycle states. Left: spatial example showing cycling (G2M/S, pink) and non-cycling (G1, gray) GCs. Right: Mean proportion of cycling vs non-cycling GCs (y axis) across radial bins; shading indicates SEM across follicles. Monotonically significant radial trends are indicated (**P*<0.05, Spearman correlation coefficient; *n*=668 follicles).

d. Diffusion pseudotime (DPT) of GCs. Left: Spatial example showing DPT values (colorbar) across two follicle fates, non-atretic (purple) and atretic (orange). Right: Mean DPT of GCs (y axis) across radial bins; shading indicates SEM across follicles. Monotonically significant radial trends are indicated (**P*<0.05, Spearman correlation coefficient); *n*=653 total follicles across 22 mice, all age groups. Follicle counts by type in **Extended Data Table 4**.

e. Ki67 (yellow) and αSMA (red) immunofluorescence in an antral follicle of a young ovary. Scale bar, 100 µm.

f. *Cyp19a1* (yellow) mRNA detected by fluorescence in situ hybridization in a young ovary. Scale bar, 100 µm.

g. GC gene programs (GEPs) identified by cNMF. Left: Spatial expression of two distinct GEPs (colorbar), FSH regulation (left) and luteinization (right), with top contributing genes in gray. Right: Mean program usage score (y axis) across radial bins (x axis) for preantral (purple), antral mitotic (maroon), antral luteinizing (teal), and atretic (orange) follicles (shading indicates SEM); *n*=653 total follicles across 22 mice, all age groups. Follicle counts by type in **Extended Data Table 4**.

h. Dynamics of GC GEPs across pseudotime (DPT), follicle type, and estrous stage in young (*n*=9) and old (*n*=7) mice. Top: kernel density distribution of follicle types (preantral, antral mitotic, antral luteinizing, and atretic) across normalized pseudotime (gaussian_kde); estrous stage composition below. Heatmaps show mean normalized GEP usage (color) for GC spots in non-atretic (middle panels) and atretic (bottom panels) follicles across pseudotime (*n*=500 bins).

i. Age-associated differences in GC GEP usage. Each cell shows the mean difference in usage (ΔGEP = [Age= Old]) per GEP (columns) between Old (*n*=7) and Young (*n*=9) mice within follicular types (rows), in estrus (upper half) and metestrus (lower half). Red = higher usage in Old; blue = lower. Statistical significance from linear models (GEP ~ Age; **Methods)**; Stars indicate Benjamini-Hochberg FDR-adjusted significance (*q<0.05, **q<0.01, ***q<0.001). Follicle counts by age, stage, and type in **Extended Data Table 4**.

560 **j.** Mean expression (log normalized counts, dot color) and proportion of expressing cells (dot size) of marker genes
561 (columns) used for annotating atretic GC subtypes (rows); *n*=17,175 spots across 22 mice, all age groups. Spot
562 counts by GC type in **Extended Data Table 4**.
563 **k.** Partition-based Graph Abstraction (PAGA) of GC types.
564 **l.** Distribution of normalized pseudotime (DPT; x axis) for spots within three distinct atretic granulosa cell clusters.
565 **k.** Mean GC type composition of follicles by age, stage, and follicle type; *n*=105,390 spots across 22 mice, all age
566 groups. Follicle counts by age, stage, and type in **Extended Data Table 4**.
567

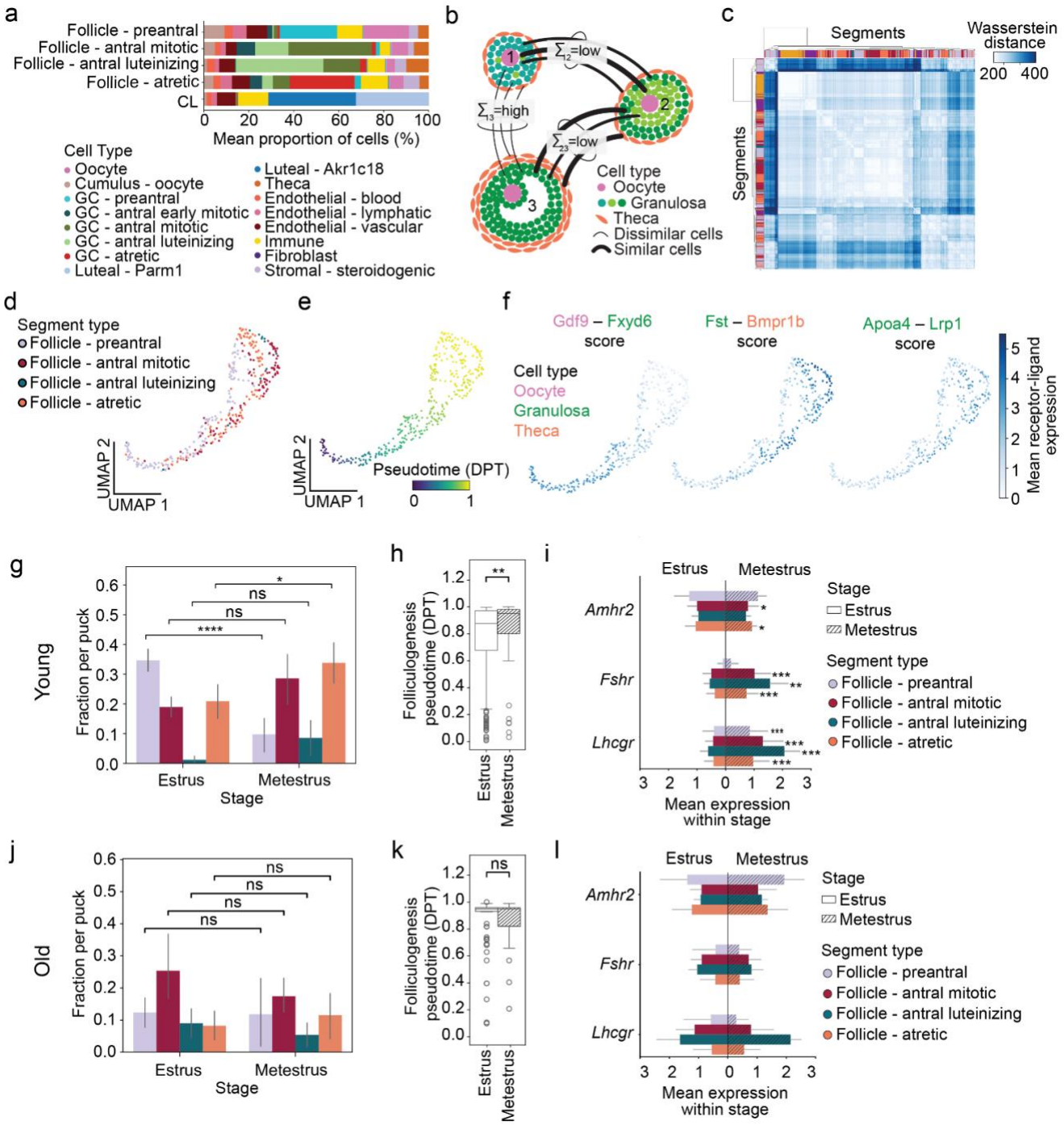

Figure 4. Aging disrupts the temporal variation in folliculogenesis.

a. Mean cell type composition of preantral (*n*=238), antral mitotic (*n*=191), atretic (*n*=181), and antral luteinizing (*n*=43) follicles, and CL (*n*=234).

b. Schematic of optimal transport inference of multicellular transitions, where pairs of follicles are aligned by minimizing their distributional distance. Transcriptionally similar pairings (e.g. GC to GC) incurs low cost, while whereas dissimilar pairings (e.g. theca to GC) incur high cost.

c. Pairwise transition matrix of segments from young mice (left; rows, columns) showing transport costs (blue) organized by unsupervised hierarchical clustering (dendrogram, axes) and annotated by segment type (color).

577 **d,e.** Interpolated folliculogenesis trajectory in young mice (*m*=382 follicles across 8 mice). UMAP of follicles (dots)
578 based on transport distances, colored by segment type (**d**) and diffusion pseudotime (DPT, colorscale) (**e**).
579 **f.** UMAPs of follicles (dots) showing mean ligand-receptor expression scores (color) for significant interactions
580 identified by MultiNicheNet (**Methods**). Ligand (panel title, left) and receptor (panel title, right) components are
581 colored by the expressing cell type; follicle counts: preantral *n*=144, antral *n*=120, atretic *n*=160.
582 **g-l.** Follicle characteristics in young (*n*=9) (**g-i**) and old (*n*=7) mice (**j-l**). **g,j.** Fraction of follicle types per puck (y
583 axis) across estrus and metestrus (x axis; $^{**}P<0.005$, ns, not significant; two-tailed t test). Puck counts: 23 in young
584 estrus, 6 in young metestrus, 12 in old estrus, 6 in old metestrus. **h,k.** Boxplots of follicle DPT (y axis) by stage (x
585 axis, bar shading) ($^{**}P<0.005$, ns, not significant; two-tailed t-test). Center line indicates median, box bounds
586 represent first and third quartiles, whiskers span from each quartile to the minimum or the maximum (1.5
587 interquartile range below 25% or above 75% quartiles). Follicle counts: young estrus *n*=281, young metestrus *n*=66,
588 old estrus *n*=58, old metestrus *n*=23. **i,l.** Mean expression of hormone receptor genes (x axis) across follicles
589 grouped by type (color) and stage (bar shading). Error bars: SEM ($^{*}P<0.05$, $^{***}P<0.01$, two-tailed t-test; all others
590 ns). Follicle counts by age, stage, and type in **Extended Data Table 4**.
591

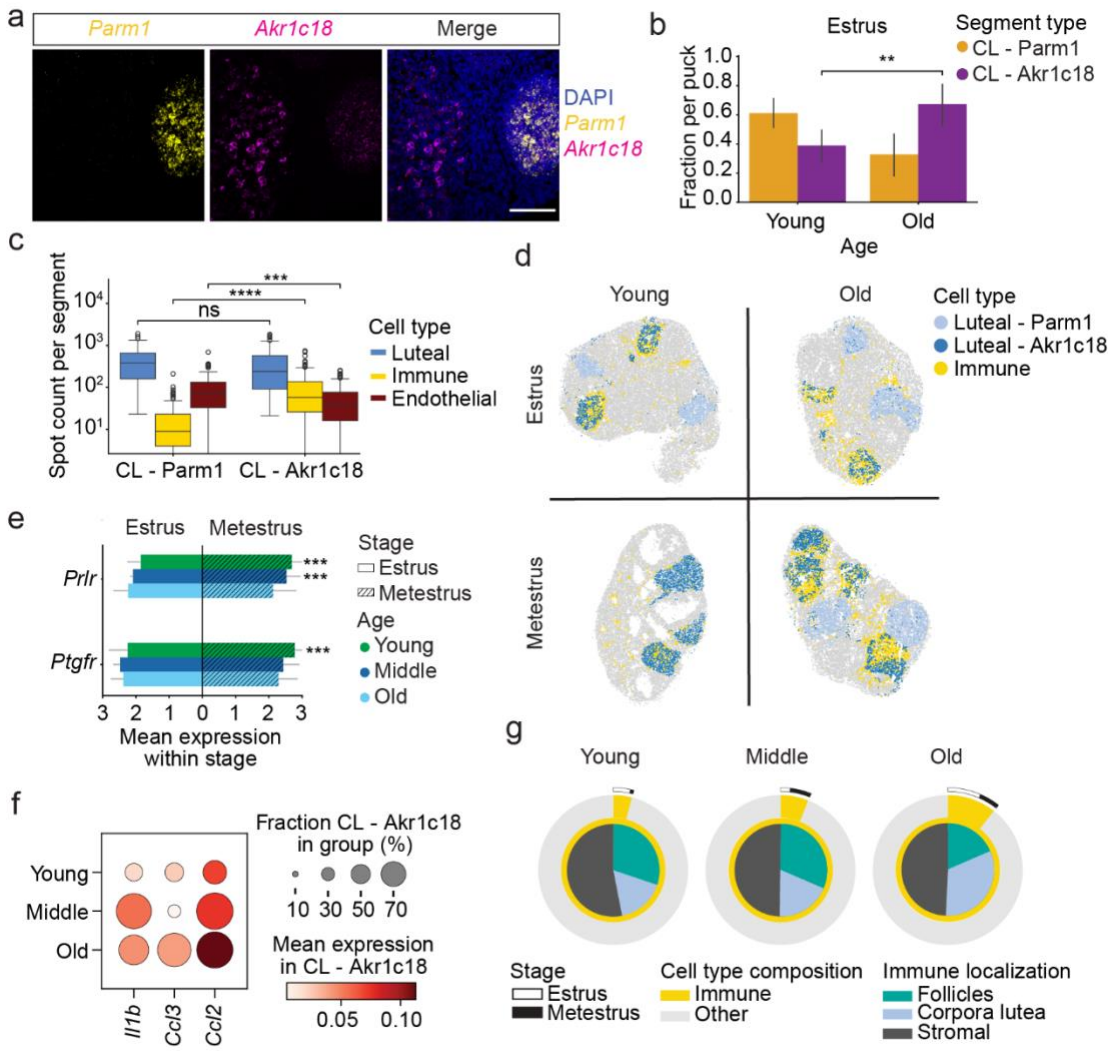

Figure 5. Aging disrupts corpus luteum clearance.

a. *Parm1* (yellow) and *Akr1c18* (teal) mRNA labeled by fluorescence in situ hybridization in a young ovary. Scale bar, 100 µm.

b. Fraction of each CL type per puck (y axis) during estrus, grouped by age (x axis). Error bars: standard deviation across pucks (young n=23, old n=12).

c. Cell type composition of CL subtypes. Boxplots show spot counts (y axis, $\log_{10}$ scale) for luteal (early and late combined), immune, and vascular cells (color) across CL - Parm1 and CL - Akr1c18 (***P<0.001, ****P<0.0001; two-tailed t-test). Center line indicates median, box bounds represent first and third quartiles, whiskers span from each quartile to the minimum or the maximum (1.5 interquartile range below 25% or above 75% quartiles); n=234 corpora lutea across 22 mice, all age groups. CL type counts in **Extended Data Table 4**.

d. Spatial maps from representative pucks across stage (estrus, metestrus) and age (young, old) showing luteal (blues) and immune (yellow) cells; all other cell types, gray.

606 **e.** Mean expression of CL regression receptor genes (x axis) in Akr1c18 CLs across young (*n*=9), middle (*n*=6),
607 and old (*n=7*) mice (color) by stage (shading). Error bars: SEM (**P*<0.05, ****P*<0.01, two-tailed t-test; all others
608 ns). Akr1c18 CL counts by age and stage in **Extended Data Table 4**.
609 **f.** Mean expression and proportion of CL - *Akr1c18* segments (dot size) expressing selected genes (x-axis) involved
610 in CL clearance and immune cell recruitment, across young (*n*=9), middle (*n*=6) and old (*n=7*) mice (rows). CL -
611 Akr1c18 counts by age in **Extended Data Table 4**.
612 **g.** Immune population changes with age. Outer ring: fraction of immune (yellow) vs. non-immune (gray) spots
613 across estrus (white) and metestrus (black). Inner ring: distribution of immune spots across spatial compartments
614 for young (*n*=31), middle (*n*=16), and old (*n*=21) pucks.

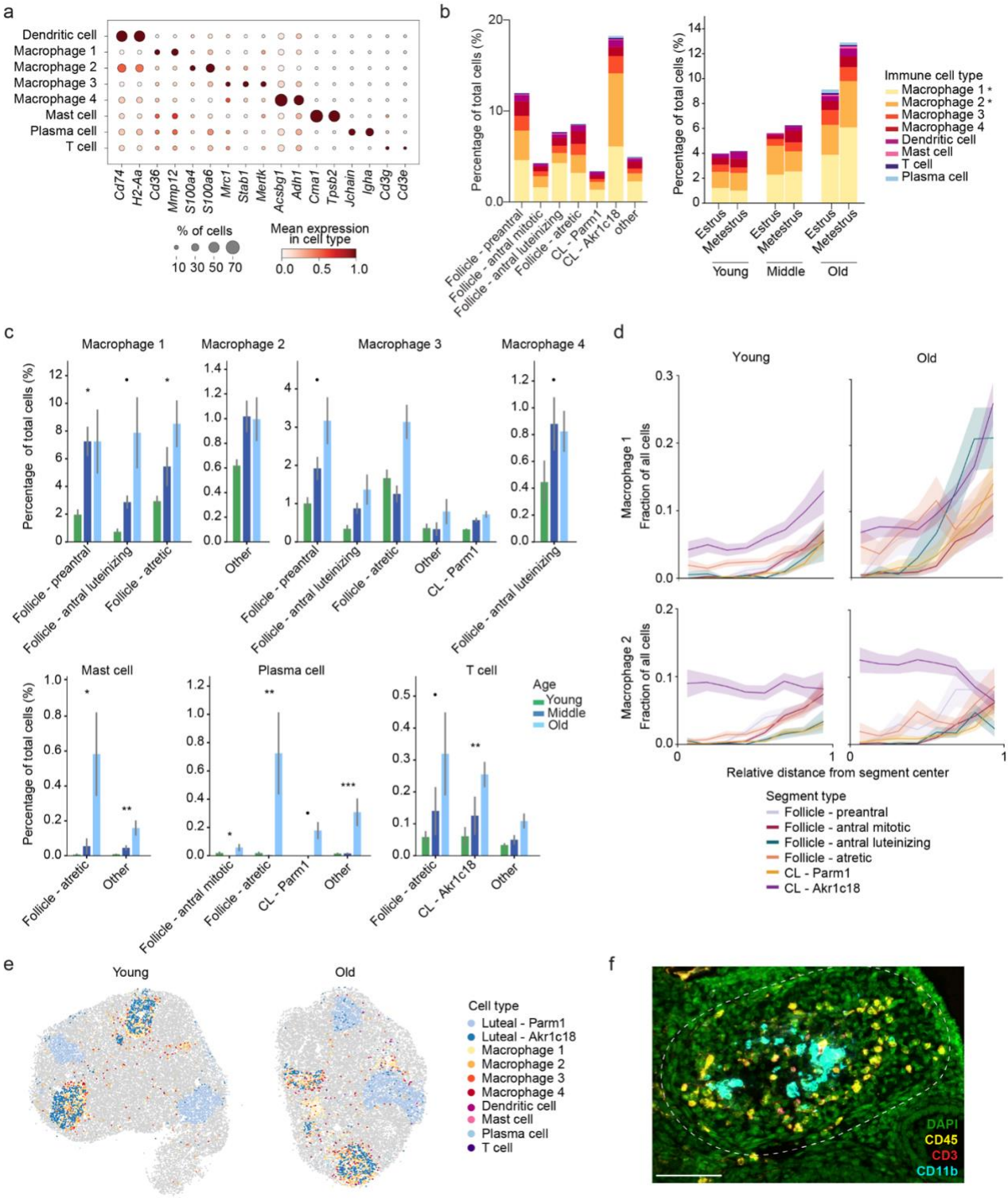

Figure 6. Age-associated changes in immune composition.

a. Mean expression (log normalized counts, color) and proportion of expressing spots (size) of marker genes (columns) of immune cell types (rows); spot counts in **Extended Data Table 4**.

b. Spatial and temporal distribution of immune cell types. Left: Percentage of immune cell types across spatial structures. Right: Percentage across stage and age. (*P<0.05, age-associated changes identified by scCODA). Follicle type and puck counts by age and stage in **Extended Data Table 4**.

c. Immune populations significantly altered with age within spatial structures. Error bars: SEM across young (n=9), middle (n=6), and old (n=7) mice. (*P<0.05, ***P<0.01, two-tailed t-test; all others, ns). Follicle type by age in **Extended Data Table 4**.

d. Distribution of macrophage subtypes (panels) by mean proportion in segment type (colored lines, y axis) in young (n=9) and old (n=7) mice across radial bins (x axis; 0 = center, 1 = edge). Shading indicates standard error of the mean (SEM); frequencies of segment types by age in **Extended Data Table 4**.

e. Representative spatial maps of immune cell types in young and old animals.

f. Immunofluorescence labeling of immune cells in a regressing CL (dotted line) from a young ovary. Scale bar, 100 μm.

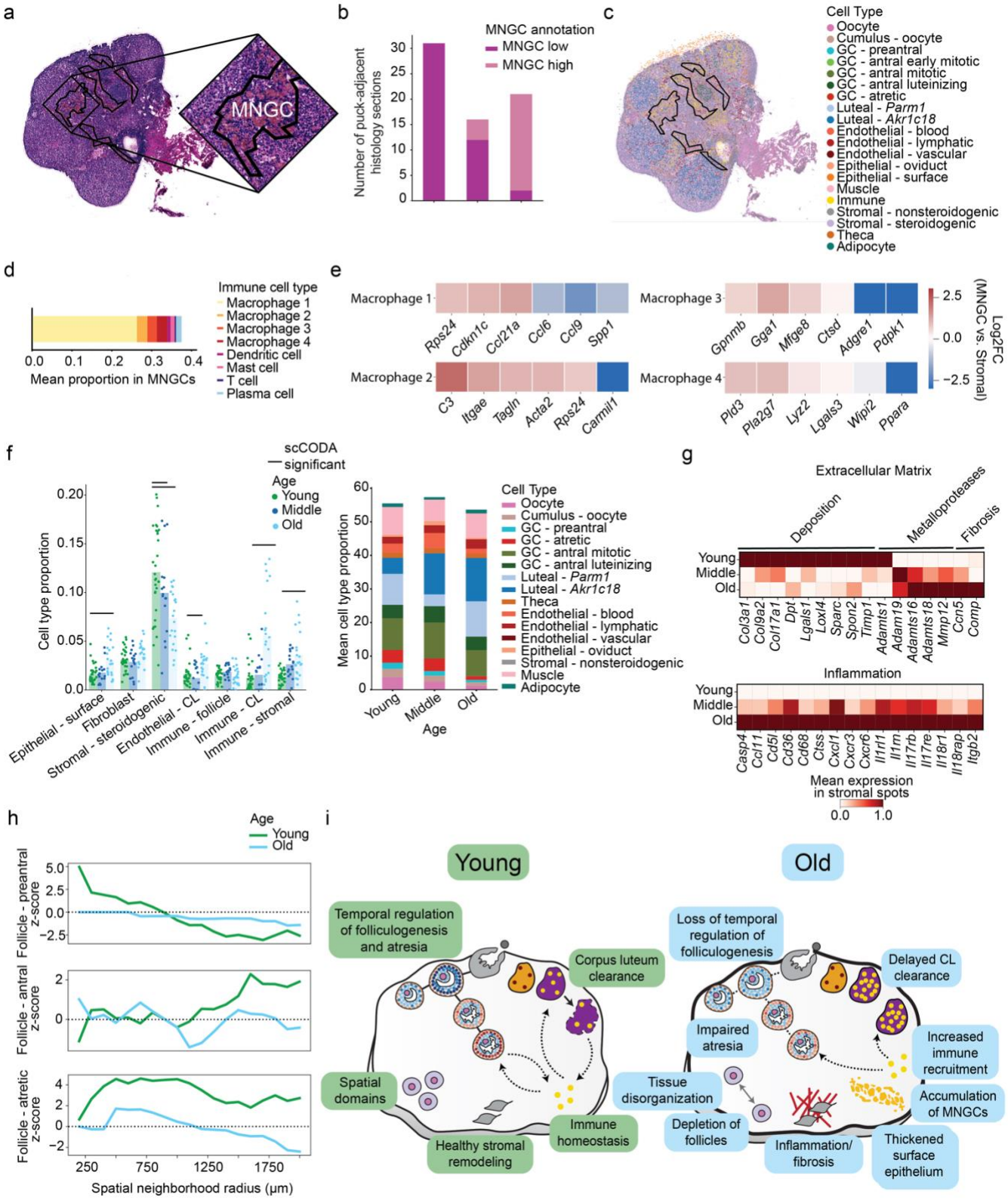

Figure 7. Loss of tissue-wide homeostatic remodeling with aging.

a. Identification of multi-nucleated giant cells (MNGCs) in aged ovaries. Example H&E section with manually drawn MNGC masks (**Methods**).

636 **b.** Distribution of histology sections (y axis) annotated as MNGC-high or MNGC-low across young (*n*=31), middle
637 (*n*=16), and old (*n*=21) pucks (x axis).
638 **c.** Example registration of MNGC masks from adjacent H&E to Slide-seq using Napari (**Methods**). Slide-seq spots
639 are colored by annotated cell type (colors).
640 **d.** Mean proportions of immune subtypes within MNGC regions in old animals.
641 **e.** Log2 fold changes in representative genes across macrophage subsets (rows), comparing stromal macrophages
642 inside vs. outside MNGCs in old animals. Spot counts in **Extended Data Table 4**.
643 **f.** Age-associated compositional changes in stromal populations. Left: Proportion (y axis) of select cell types (x
644 axis) for individual pucks (dots) and mean across pucks (bars); significant changes identified by scCODA using all
645 cell types with "Epithelial – oviduct" as the reference (**Extended Data Fig. 6d**; **Methods**; black bars, FDR=0.05).
646 Right: Mean proportion of all remaining cell types (y bars) across ages (x axis); puck counts: young *n*= 32, middle
647 *n*=16 pucks, old *n*=21 pucks.
648 **g.** Mean expression (log normalized, variance-scaled) of ECM- and inflammation-related genes (columns) in
649 stromal subtypes ("stromal – non-steroidogenic", "stromal – steroidogenic", "fibroblast") across young (*n*=9),
650 middle (*n*=6) and old (*n=7*) mice (rows). Genes identified by differential expression analysis between young and
651 old stromal spots (**Methods**); spot counts in **Extended Data Table 4**.
652 **h.** Spatial neighborhood analysis of homotypic follicle co-localization. Z-scores of co-localization (y axis) as a
653 function of increasing spatial radius (x axis; 200 μm steps) compared to a null model (z-score 0, black dotted line)
654 for preantral (top), antral (middle), atretic (bottom) follicles in young (*n*=9) and old (*n=7*) mice (colors); follicle
655 counts by age in **Extended Data Table 4**.
656 **i.** Schematic hallmarks of ovarian aging. Aging impacts key processes underlying tissue-wide homeostasis,
657 impacting both the reproductive and endocrine functions of the ovary. Young ovaries maintain temporal regulation
658 of folliculogenesis, spatial domain integrity, immune homeostasis, and coordinated remodeling. Aged ovaries show
659 disrupted timing, impaired atresia and CL clearance, tissue disorganization, follicle loss, MNGC accumulation,
660 inflammation, fibrosis, and surface epithelial thickening.

a

Mouse	Age	Stage	# Pucks
5	Young	Estrus	6
7	Young	Estrus	5
8	Young	Estrus	5
13	Young	Estrus	2
16	Young	Estrus	1
AK01b	Young	Estrus	4
AK02b	Young	Estrus	3
6	Young	Metestrus	5
26	Young	Metestrus	1
9	Middle	Estrus	1
12	Middle	Estrus	1
18	Middle	Estrus	1
19	Middle	Estrus	2
10	Middle	Metestrus	5
11	Middle	Metestrus	6
1	Old	Estrus	5
3	Old	Estrus	4
21	Old	Estrus	1
F12ov	Old	Estrus	3
2	Old	Metestrus	4
4	Old	Metestrus	2
25	Old	Metestrus	2

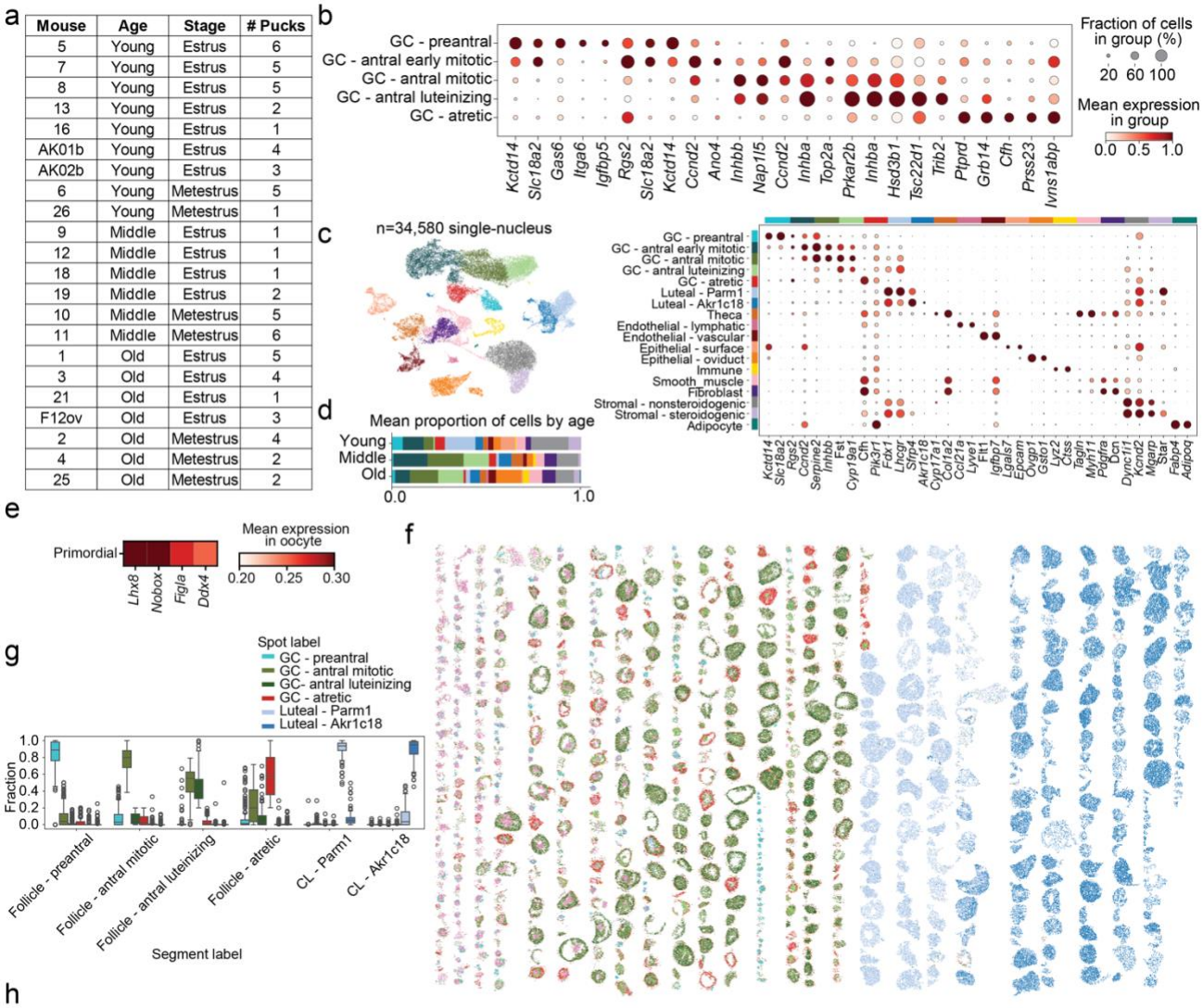

662

663 **Extended Data Figure 1. Classification and characteristics of segments driving folliculogenesis.**

664 **a.** Table of pucks sequenced per mouse, with age and estrous stage.

665 **b.** Mean expression (color, scaled per gene) and fraction of expressing cells (dot size) of marker genes (columns)
666 defining GC subclusters (rows). Top five differentially expressed genes per subcluster shown (Wilcoxon rank-sum
667 test; min log fold-change ≥ 1).

668 **c**. UMAP embedding of 34,580 nuclei from whole-ovary snRNA-seq colored by major cell type. Dot plot shows
669 mean expression (color, log normalized counts) and fraction of expressing cells (dot size) of marker genes used to
670 annotate granulosa, luteal, stromal, immune, endothelial, and epithelial populations.

671 **d.** Mean cell type proportions across young, middle, and old mice, showing age-associated compositional shifts.

672 **e.** Mean composite expression of primordial oocyte marker genes across primordial oocytes (n=57).

673 **f.** Summary spatial plot of all detected follicle and CL segments.

674 **g.** Boxplot of spot-level cell type composition (y axis, colors) across segment labels (x axis). Boxplot: center line
675 indicates median, box bounds represent first and third quartiles, whiskers span from each quartile to the minimum
676 or the maximum (1.5 interquartile range below 25% or above 75% quartiles); segment counts by type in **Extended**
677 **Data Table 4**.

678 **h.** PCA of segments based on cell type composition. Left: segments by spot counts. Right: segments colored by
679 assigned type.

680 **i.** Mean follicle counts from adjacent H&E and Slide-seq segmentation across age groups. Error bars: SEM.
681 (*P<0.05, **P<0.01, ***P<0.001, ****P<0.0001 two-tailed t-test; all other bar groups, ns); young n=31, middle
682 n=16, old n=21 pucks.

683 **j.** Mean proportion of immune cells (y axis) across radial distance (x axis; 0-1) for each follicle type (color, lines);
684 shading indicates SEM. Immune fractions differ between atretic and non-atretic follicles containing an oocyte
685 (P<0.005, Tukey HSD test). Follicle counts by type in **Extended Data Table 4**.

686

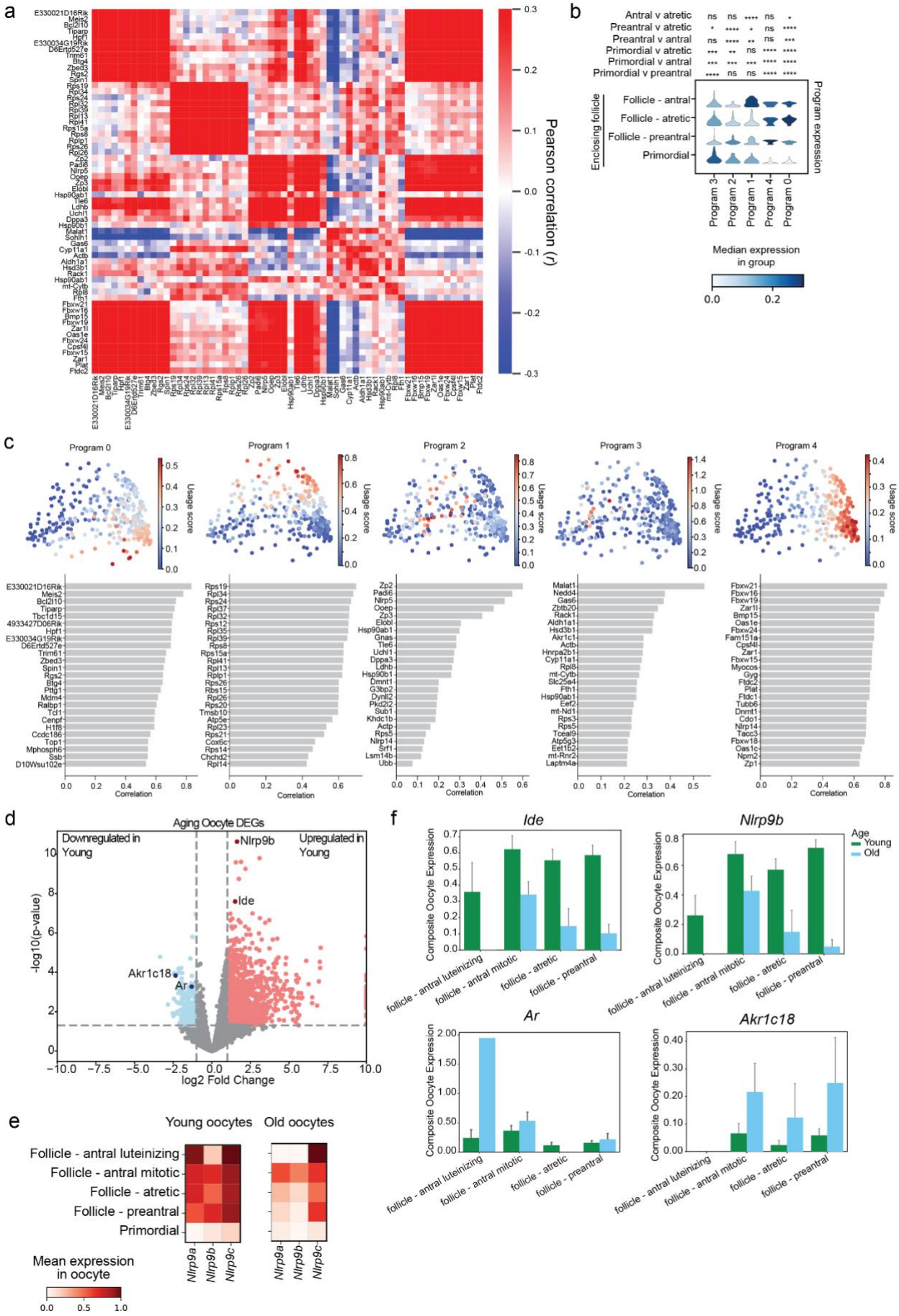
a
Pearson correlation (r)
b
Antral v atretic
Preantral v atretic
Preantral v antral
Primordial v atretic
Primordial v antral
Primordial v preantral
Enclosing follicle
Follicle - antral
Follicle - atretic
Follicle - preantral
Primordial
Program expression
Program 3
Program 2
Program 1
Program 4
Program 0
Median expression in group
c
Program 0
Program 1
Program 2
Program 3
Program 4
Usage score
Correlation
d
Aging Oocyte DEGs
Downregulated in Young
Upregulated in Young
Nlrp9b
Ide
Akr1c18
Ar
-log10(p-value)
log2 Fold Change
e
Young oocytes
Old oocytes
Follicle - antral luteinizing
Follicle - antral mitotic
Follicle - atretic
Follicle - preantral
Primordial
Nlrp9a
Nlrp9b
Nlrp9c
Mean expression in oocyte
f
Ide
Nlrp9b
Ar
Akr1c18
Age
Young
Old
Composite Oocyte Expression
follicle - antral luteinizing
follicle - antral mitotic
follicle - atretic
follicle - preantral

688 **Extended Data Figure 2. Evaluating oocyte transcriptomes using non-negative matrix factorization**

689 **a.** Pearson correlation (red/blue color) of pairwise gene expression across oocytes (rows and columns) based on the
690 top 12 genes from each cNMF program, ordered by hierarchical clustering; *n*=358 oocytes.

691 **b.** Median expression (color) and distribution (kernel density) of oocyte gene program scores (x axis) by enclosing
692 follicle type (y axis); significance assessed by two-tailed tests (**P*<0.05, ***P*<0.01, ****P*<0.001, *****P*<0.0001;
693 ns). Oocyte counts by enclosing follicle type in **Extended Data Table 4**.

694 **c.** PCA embedding of composite oocyte transcriptomes showing usage of cNMF programs and their top 20
695 contributing genes; *n*=358 oocytes.

696 **d**. Differentially expressed genes (dots) between young (n=9) and old (n=7) oocytes. Volcano plot showing
697 significance (y axis, $-\log_{10}$(P-value)) and $\log_2$ fold change (x axis). Significant genes (Benjamini-Hochberg
698 FDR<5%, log2FC>1) colored; select genes annotated. Non-primordial oocyte counts by age in **Extended Data**
699 **Table 4**.

700 **e.** Mean expression (log normalized, variance-scaled) of *Nlrp9*-family genes (columns) in oocytes grouped by the
701 enclosing follicle type (rows), in young (left, *n*=9) and old (right, *n*=7) mice. Oocyte counts by enclosing follicle
702 type and age in **Extended Data Table 4**.

703 **f.** Mean expression of selected differentially expressed genes in oocytes by follicle type for young (*n*=9) and old
704 (*n*=7) mice. Error bars: SEM. Oocyte counts by enclosing follicle type and age in **Extended Data Table 4**.

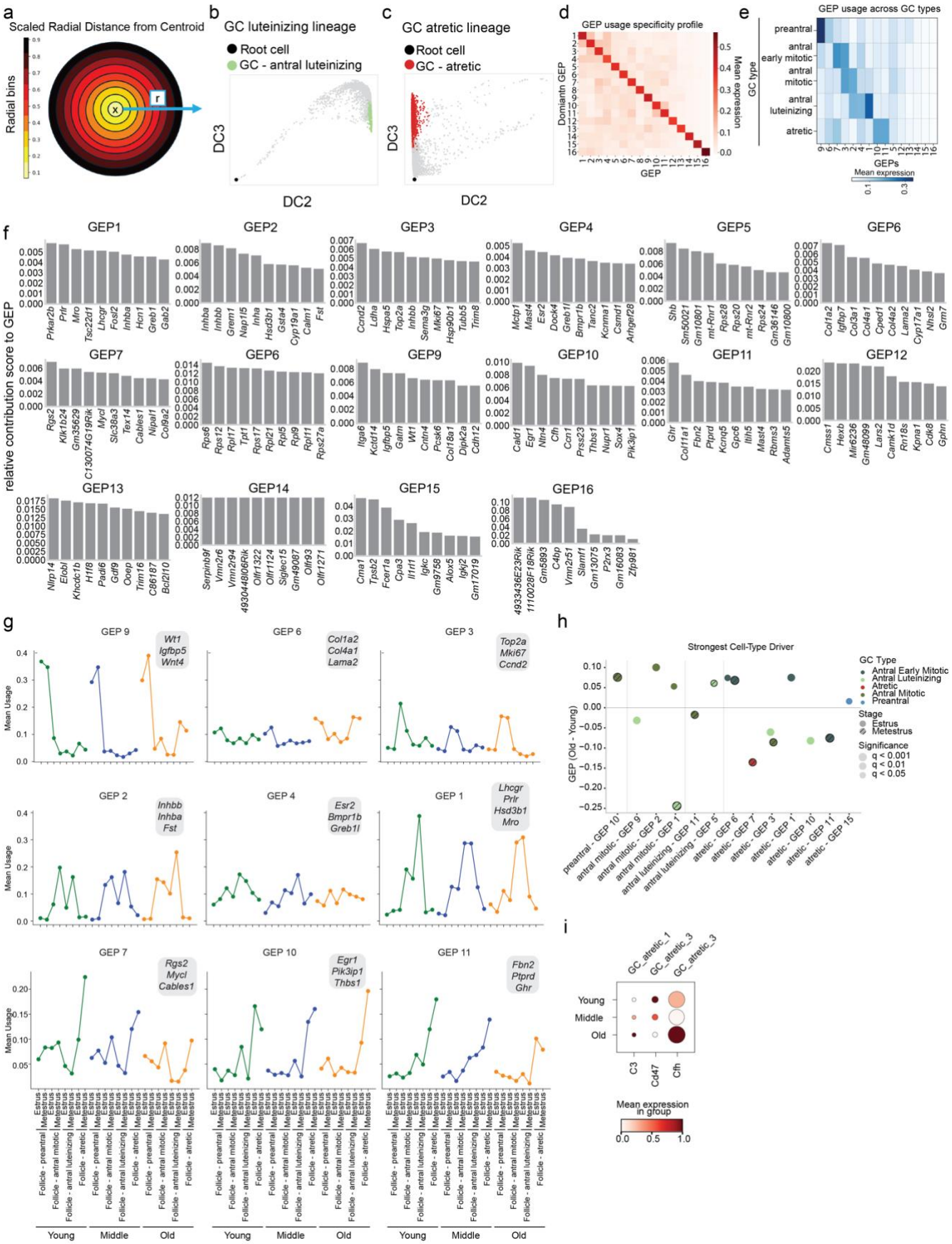
a
Scaled Radial Distance from Centroid
Radial bins
r
b
GC luteinizing lineage
Root cell
GC - antral luteinizing
DC3
DC2
c
GC atretic lineage
Root cell
GC - atretic
DC3
DC2
d
GEP usage specificity profile
Dominatn GEP
GEP
Mean expression
e
GEP usage across GC types
GC type
preantral
antral early mitotic
antral mitotic
antral luteinizing
atretic
GEPs
Mean expression
f
relative contribution score to GEP
GEP1
Prkar2b Prlr Mro Tsc22d1 Lhcgr Fosl2 Inhba Hcn1 Greb1 Gab2
GEP2
Inhba Inhbb Grem1 Nap1l5 Inha Hsd3b1 Gsta4 Cyp19a1 Calm1 Fst
GEP3
Ccnd2 Ldha Hspa5 Top2a Inhbb Sema3g Mki67 Hsp90b1 Tubb5 Trim8
GEP4
Mctp1 Mast4 Esr2 Dock4 Greb1l Bmpr1b Tanc2 Kcnma1 Csmd1 Arhgef28
GEP5
Shb Sm50021 Gm10801 mt-Rnr1 Rps28 Rps20 mt-Rnr2 Rps24 Gm36146 Gm10800
GEP6
Col1a2 Igfbp7 Col3a1 Col4a1 Cped1 Col4a2 Lama2 Cyp17a1 Nhsl2 Grm7
GEP7
Rgs2 Klk1b24 Gm35629 C130074G19Rik Mycl Slc38a3 Tex14 Cables1 Nipal1 Col9a2
GEP6
Rps6 Rps12 Rpl17 Tpt1 Rps17 Rpl21 Rpl5 Rpl9 Rpl11 Rps27a
GEP9
Itga6 Kctd14 Igfbp5 Galm Wt1 Cntn4 Pcsk6 Col18a1 Dipk2a Cdh12
GEP10
Cald1 Egr1 Ntn4 Cfh Ccn1 Prss23 Thbs1 Nupr1 Sox4 Pik3ip1
GEP11
Ghr Col11a1 Fbn2 Ptprd Kcnq5 Gpc6 Itih5 Mast4 Rbms3 Adamts5
GEP12
Cmss1 Hexb Mir6236 Gm48099 Lars2 Camk1d Rn18s Kpna1 Cdk8 Gphn
GEP13
Nlrp14 Elobl Khcdc1b H1f8 Pad16 Gdf9 Ooep Trim16 C86187 Bcl2l10
GEP14
Serpinb9r Vmn2r6 Vmn2r94 4930448I06Rik Olfr1322 Olfr1124 Siglec15 Gm49087 Olfr93 Olfr1271
GEP15
Cma1 Tpsb2 Fcer1a Cpa3 Il1rl1 Igkc Gm9758 Alox5 Igkj2 Gm17019
GEP16
4933436E23Rik 1110028F18Rik Gm5893 C4bp Vmn2r51 Slamf1 Gm13075 P2rx3 Gm16083 Zfp981
g
GEP 9
Wt1 Igfbp5 Wnt4
GEP 6
Col1a2 Col4a1 Lama2
GEP 3
Top2a Mki67 Ccnd2
GEP 2
Inhbb Inhba Fst
GEP 4
Esr2 Bmpr1b Greb1l
GEP 1
Lhcgr Prlr Hsd3b1 Mro
GEP 7
Rgs2 Mycl Cables1
GEP 10
Egr1 Pik3ip1 Thbs1
GEP 11
Fbn2 Ptprd Ghr
Mean Usage
Estrus
Metestrus
Follicle - preantral
Follicle - antral mitotic
Follicle - antral luteinizing
Follicle - atretic
Young
Middle
Old
h
Strongest Cell-Type Driver
GEP (Old - Young)
GC Type
Antral Early Mitotic
Antral Luteinizing
Atretic
Antral Mitotic
Preantral
Stage
Estrus
Metestrus
Significance
q < 0.001
q < 0.01
q < 0.05
preantral - GEP 10
antral mitotic - GEP 9
antral mitotic - GEP 2
antral mitotic - GEP 1
antral luteinizing - GEP 11
antral luteinizing - GEP 5
atretic - GEP 6
atretic - GEP 7
atretic - GEP 3
atretic - GEP 1
atretic - GEP 10
atretic - GEP 11
atretic - GEP 15
i
GC_atretic_1
GC_atretic_3
GC_atretic_3
Young
Middle
Old
C3
Cd47
Cfh
Mean expression in group

705

706

Extended Data Figure 3. Spatial and molecular determinants of granulosa coordination in follicular niches.

a. Schematic of radial analysis. Scaled radial distance (*r*) from the follicular centroid ("x") was computed for each GC spot across 10 uniformly spaced, concentric bins were used to aggregate spot-level characteristics.

b,c. Diffusion map embeddings (DC2, DC3) of GCs (spots) along luteinizing (**b**) and atretic (**c**) lineages, colored by terminal fate ("GC – antral luteinizing", "GC – atretic") and annotated with the root spot (black dot) used for diffusion pseudotime (DPT).

d. Mean expression (red colorscale; log normalized, variance-scaled) of GC gene programs (rows, columns). GCs were grouped by their dominant program (highest usage); within-group mean program scores are shown.

e. Mean usage of K=16 cNMF-derived gene expression programs (GEPs; columns) across GC subtypes (rows). Color intensity indicates the mean normalized program usage within each group.

f. Top contributing genes (*x* axis) for each of the 16 GC GEPs (subplot) and their contribution scores (*y* axis). Contribution scores reflect gene weights within each program.

g. Mean usage of selected GEPs by follicle type, estrous stage, and age. Each panel (GEP) lists top contributing genes for that GEP and shows the mean GEP usage across preantral, antral, and atretic follicles for young (green), middle (blue), and old (orange) mice. Follicle counts by stage and age in **Extended Data Table 4**.

h. Dominant GC subtype drivers of age-associated GEP changes. For each significant follicle-level GEP ($q < 0.05$), the GC subtype with the largest age effect (Old − Young) within each estrous stage is shown. Points represent effect size (β[Age = Old]) for the most strongly associated cell type within the corresponding follicle segment and GEP. Colors denote the dominant GC subtype, while hatch marks distinguish stages (solid = Estrus, hatched = Metestrus). Point size encodes statistical significance level ($q < 0.05$, 0.01, 0.001). Positive effect sizes indicate higher GEP usage in old ovaries, and negative values indicate higher usage in young. Vertical separators delineate follicle type.

i. Expression of selected immune-related genes in atretic GC clusters by age. Dot size indicates fraction of expressing cells; color indicates normalized mean expression level.

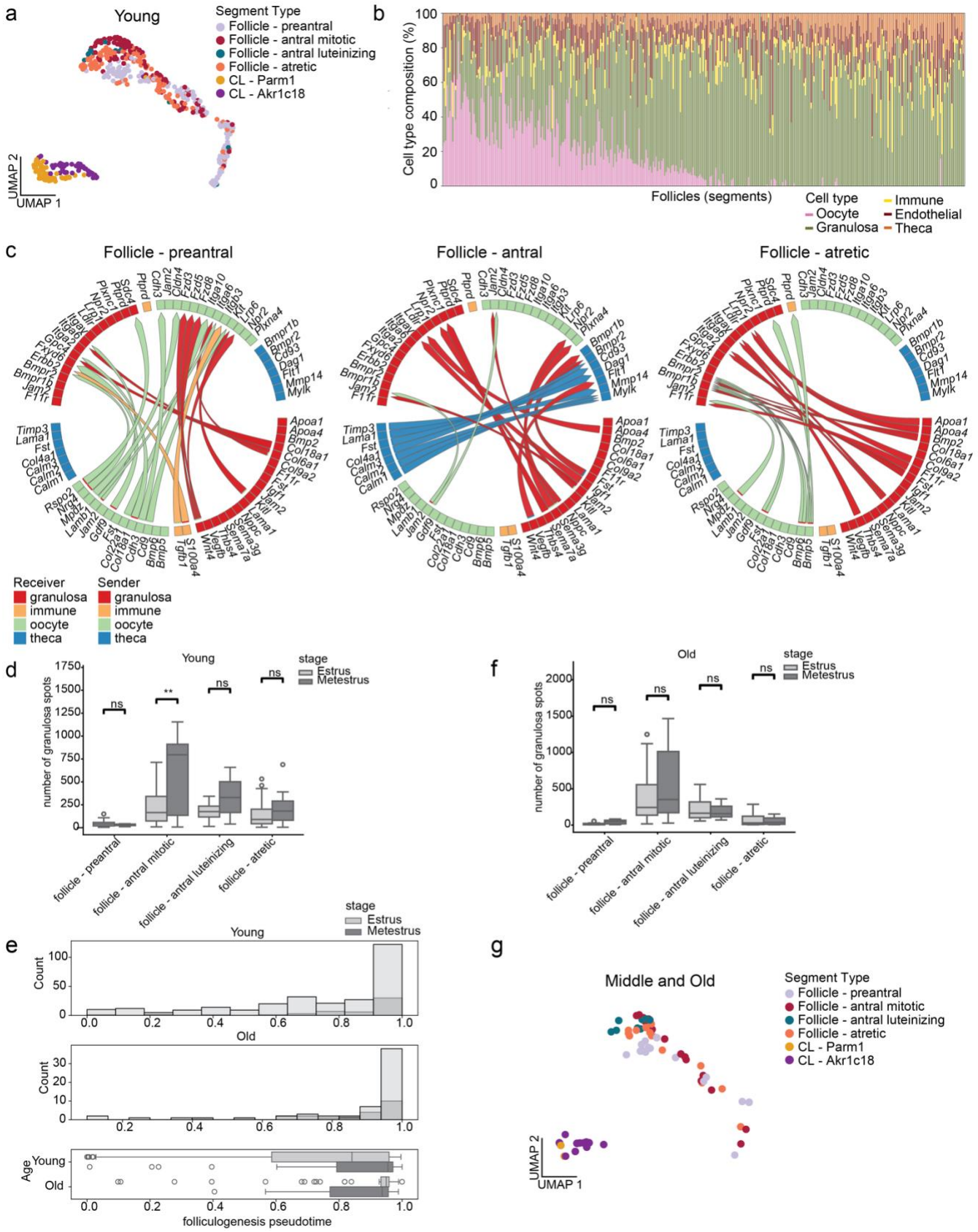
a
Young
Segment Type
Follicle - preantral
Follicle - antral mitotic
Follicle - antral luteinizing
Follicle - atretic
CL - Parm1
CL - Akr1c18
UMAP 2
UMAP 1
b
Cell type composition (%)
Follicles (segments)
Cell type
Oocyte
Granulosa
Immune
Endothelial
Theca
c
Follicle - preantral
Follicle - antral
Follicle - atretic
Receiver
granulosa
immune
oocyte
theca
Sender
granulosa
immune
oocyte
theca
d
Young
stage
Estrus
Metestrus
number of granulosa spots
follicle - preantral
follicle - antral mitotic
follicle - antral luteinizing
follicle - atretic
e
Young
Old
Count
Age
folliculogenesis pseudotime
f
Old
number of granulosa spots
g
Middle and Old
Segment Type
Follicle - preantral
Follicle - antral mitotic
Follicle - antral luteinizing
Follicle - atretic
CL - Parm1
CL - Akr1c18
UMAP 2
UMAP 1

Extended Data Figure 4. Age-associated temporal dysregulation of folliculogenesis.

a. UMAP of all young segments (dots; *n*=472 follicles and corpora lutea) based on transport cost distances.

b.c. Cell type composition (colors, y axis) of each follicle (bars, x axis) ordered by their folliculogenesis diffusion pseudotime as in **Fig. 4e**.

c. Circos plot of the top receptor-ligand interactions enriched in preantral (left; *n*=144), antral (center; *n*=114), and atretic (right; *n*=109) follicles identified by MultiNicheNet. Interactions significantly enriched in each follicle type are shown by arrows starting from ligands (bottom half) of a "sender" cell type (color) to the corresponding receptor (top half) of a "receiver" cell type (color).

d. Distribution of follicle sizes in young mice. Boxplot of the follicle size (number of granulosa spots; y axis) by follicle type (x axis) and stage (bar shading) (**$P<0.005$, two-tailed t-test of means). Boxplot: center line indicates the median, box bounds represent the first and third quartiles, and whiskers span from each quartile to the minimum or the maximum (1.5 interquartile range below 25% or above 75% quartiles). Follicle type by stage counts in **Extended Data Table 4**.

e. Distribution of follicle pseudotime in young and old mice. Boxplot of follicle pseudotime in old and young across stages. Boxplot elements: same as in **d**. Follicle counts by stage and age in **Extended Data Table 4**.

f. Distribution of follicle sizes in old mice. Boxplot of the follicle size (number of granulosa spots; y axis) by follicle type (x axis) and stage (bar shading) (ns, two-tailed t-test of means). Boxplot elements: same as in **d**. Follicle type by stage counts in **Extended Data Table 4**.

g. UMAP of all middle and old segments (dots; *n*=190 follicles and corpora lutea) projected into the young segment trajectory based on their transport cost matrix.

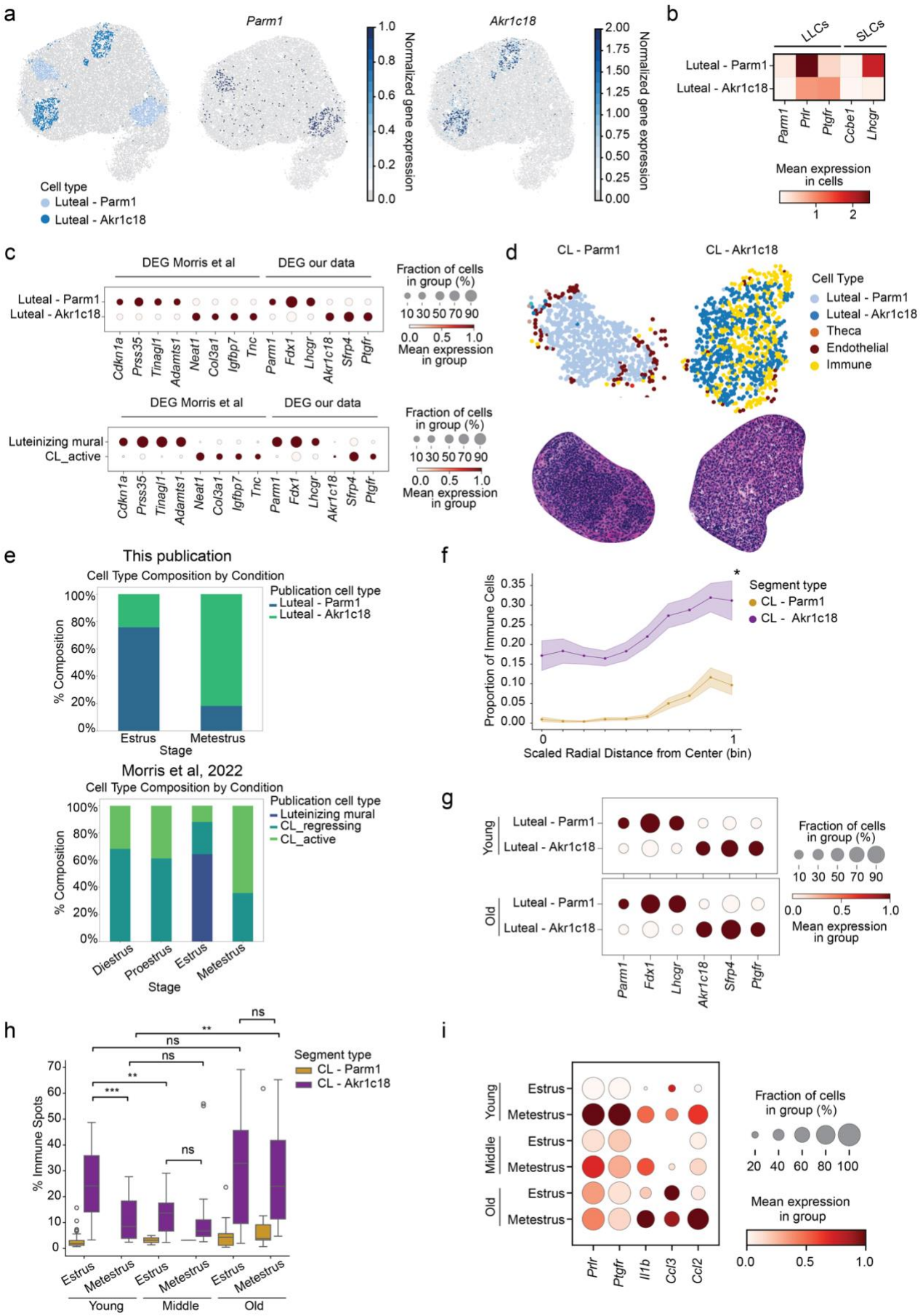
a
Parm1
Akr1c18
Normalized gene expression
Cell type
Luteal - Parm1
Luteal - Akr1c18
b
LLCs
SLCs
Luteal - Parm1
Luteal - Akr1c18
Parm1
Prlr
Ptgfr
Ccbe1
Lhcgr
Mean expression in cells
c
DEG Morris et al
DEG our data
Luteal - Parm1
Luteal - Akr1c18
Luteinizing mural
CL_active
Cdkn1a
Prss35
Tinagl1
Adamts1
Neat1
Col3a1
Igfbp7
Tnc
Parm1
Fdx1
Lhcgr
Akr1c18
Sfrp4
Ptgfr
Fraction of cells in group (%)
Mean expression in group
d
CL - Parm1
CL - Akr1c18
Cell Type
Luteal - Parm1
Luteal - Akr1c18
Theca
Endothelial
Immune
e
This publication
Cell Type Composition by Condition
Publication cell type
Luteal - Parm1
Luteal - Akr1c18
% Composition
Estrus
Metestrus
Stage
Morris et al, 2022
Cell Type Composition by Condition
Publication cell type
Luteinizing mural
CL_regressing
CL_active
Diestrus
Proestrus
Estrus
Metestrus
f
Proportion of Immune Cells
Segment type
CL - Parm1
CL - Akr1c18
Scaled Radial Distance from Center (bin)
g
Young
Old
Luteal - Parm1
Luteal - Akr1c18
Parm1
Fdx1
Lhcgr
Akr1c18
Sfrp4
Ptgfr
Fraction of cells in group (%)
Mean expression in group
h
% Immune Spots
Segment type
CL - Parm1
CL - Akr1c18
Estrus
Metestrus
Young
Middle
Old
i
Young
Middle
Old
Estrus
Metestrus
Prlr
Ptgfr
Il1b
Ccl3
Ccl2
Fraction of cells in group (%)
Mean expression in group

754

Extended Data Figure 5. Dysregulation of corpora lutea clearance with age.

a. Spatial visualization of luteal cell type markers in a representative puck. Top: early (light blue) and late (dark blue) luteal cell clusters. Middle and right: normalized expression of luteal subtype markers *Parm1* and *Akr1c18* (blue scale). All other cell types in gray.

b. Mean expression of genes associated with large luteal cells (LLCs) and small luteal cells (SLCs) in previous literature. Spot counts in **Extended Data Table 4**.

c. Differentially expressed genes (DEGs) of luteal clusters from Morris et al. and their corresponding expression in our dataset, showing high concordance between 'Luteal - Parm1' and 'Luteinizing mural,' and between 'Luteal - Akr1c18' and 'Active CL.'

d. Representative spatial plots and H&E images of 'CL - Parm1' and 'CL - Akr1c18' structures.

e. Relative proportions of luteal subtypes across estrus and metestrus in our dataset (top) compared with all 4 estrous stages in Morris et al. 2022[37] (bottom).

f. Immune cell proportions within each CL type (colored lines, y axis) as a function of the radial distance (x axis) from the CL center (0) to edge (1). Shaded lines represent the standard error of the mean (SEM) fraction across segments within each radial bin ($P<0.005$, Tukey HSD, all bins). CL type counts in **Extended Data Table 4**.

g. Age-stratified gene expression showing conservation of luteal subtype marker expression in young (top) and old (bottom) ovaries, demonstrating that transcriptional identities are preserved with age despite shifts in proportional abundance.

h. Immune cell abundance in CL subtypes. Boxplots show distribution of spot counts (y axis, $\log_{10}$ scale) of luteal (early and late combined), immune, and vascular cell types (color) across 'CL – Parm1' and 'CL – Akr1c18' (**$P<0.01$, ***$P<0.001$, ns – not significant; two-tailed t-test). Center line indicates median, box bounds represent first and third quartiles, whiskers span from each quartile to the minimum or the maximum (1.5 interquartile range below 25% or above 75% quartiles). CL type counts by age and stage in **Extended Data Table 4**.

i. Mean expression and proportion of CL - Akr1c18 segments (dot size) expressing select CL clearance and immune-recruitment genes (x-axis), grouped by age and stage (rows). CL – Akr1c18 counts by age and stage in **Extended Data Table 4**.

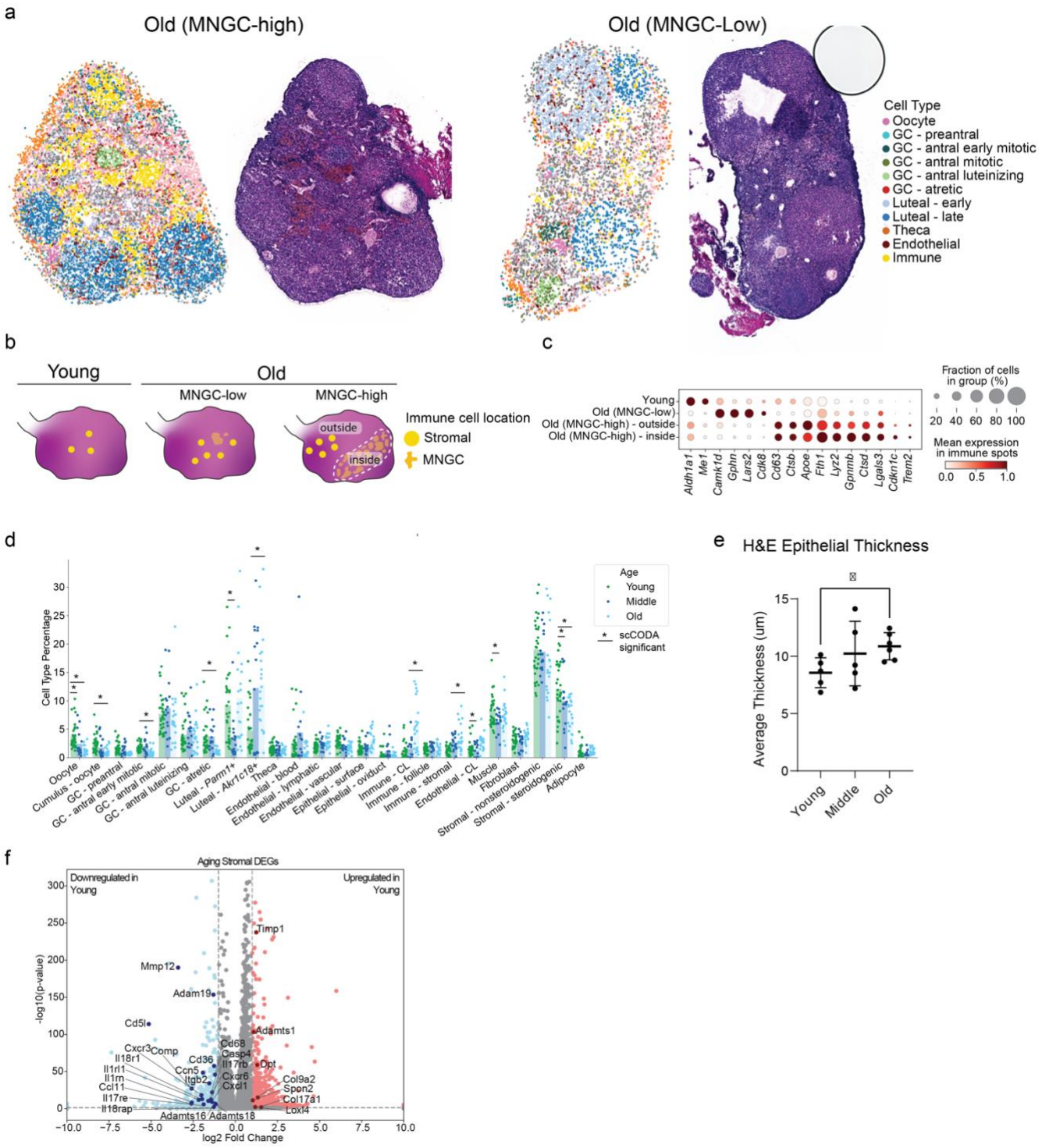

Extended Data Figure 6. MNGC signatures in aging ovaries.

a. Representative spatial plots and adjacent H&E sections for old animals categorized as 'MNGC-high' and 'MNGC-low'.

b. Schematic of MNGC transcriptional analysis. Stromal immune spots were grouped by age (young *vs* old) and MNGC content (low *vs* high), then examined for differentially expressed genes (DEGs) across these four categories.

790 Mean expression (log normalized counts, dot color) and proportion of expressing stromal immune cells (dot size)
791 of differentially expressed genes (columns) in each age-MNGC category (rows).
792 **c.** DEGs in aging stromal cells (fibroblasts, stromal nonsteroidogenic, stromal steroidogenic). Significance (y axis,
793 $-\log_{10}$(P-value)) and effect size as $\log_2$-fold change (x axis) for genes (dots) that are differentially expressed between
794 young and old. Significant genes (color; Benjamini-Hochberg FDR<5%, log2FC>1) are annotated with select
795 genes. Spot counts in **Extended Data Table 4**.
796 **d.** Distribution of cell type composition (y axis) across pucks (dot) and the mean composition across pucks (bars)
797 within each age group (color). Significant changes determined by scCODA indicated by black bars (FDR=0.05).
798 Young *n*= 32 pucks, Middle *n*=16 pucks, Old *n*=21 pucks.
799 **e.** Average surface epithelium thickness in adjacent H&E sections of young, middle, and old animals. Dots represent
800 an H&E section, where three thickness measurements were taken and averaged. Bars represent mean, error bars
801 SEM (**P*<0.05, two-tailed t-test of means); *n*=5 pucks per age group.
802 **f.** Differentially expressed genes in aging stromal cells (fibroblasts, stromal nonsteroidogenic, stromal
803 steroidogenic). Significance (y axis, $-\log_{10}$(P-value)) and effect size as $\log_2$-fold change (x axis) for genes (dots)
804 that are differentially expressed between young and old. Significant genes (color; Benjamini-Hochberg FDR<5%,
805 log2FC>1) are annotated with select genes. Spot counts in **Extended Data Table 4**.
806

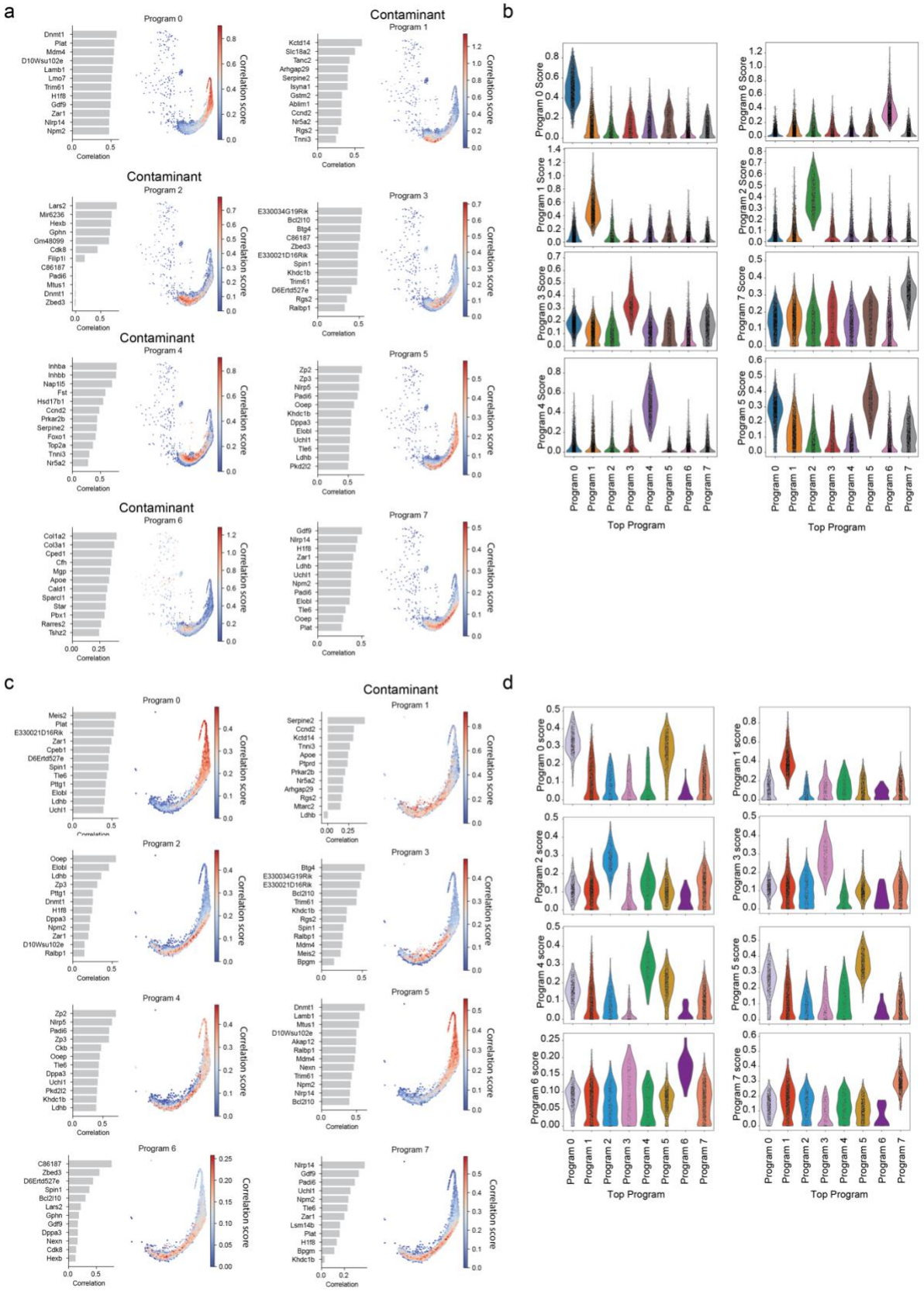
a
Contaminant
Program 0
Program 1
Program 2
Program 3
Program 4
Program 5
Program 6
Program 7
Correlation
Correlation score
b
Program 0 Score
Program 1 Score
Program 2 Score
Program 3 Score
Program 4 Score
Program 5 Score
Program 6 Score
Program 7 Score
Top Program
c
d
Program 0 score
Program 1 score
Program 2 score
Program 3 score
Program 4 score
Program 5 score
Program 6 score
Program 7 score

807

808

809 **Extended Data Figure 7. Identifying contaminated oocyte spots using non-negative matrix factorization.**
810 Two iterations of oocyte spot decontamination.
811 **a-d.** Identifying contaminated oocyte spots through a two-step iteration, with the first iteration in **a,b** to remove
812 contaminant spots, followed by a second iteration in **c,d** to further remove residual contaminants.
813 **a,c.** Gene programs identified through NMF on oocyte spots using *k*=8 programs. Correlation scores (left, x axis)
814 of the top 12 genes (left, y axis) and their program usage on a UMAP projection (right) of oocyte spots. Programs
815 identified as contamination based on the expression of known cumulus and granulosa marker genes are labeled as
816 'Contaminant' (first iteration: programs 1, 2, 4, and 6; second iteration: program 1).
817 **b,d.** Distribution of program scores (y axis, kernel density estimate) grouped by the top gene program (x axis) for
818 each spot (dots). Distributions were used to manually set program-specific thresholds for removing contaminants.
819 First iteration thresholds: Program 1: > 0.4, Program 2: > 0.3, Program 4: > 0.3, Program 6: > 0.4. Second iteration
820 thresholds: Program 1: > 0.3.

821 **METHODS**

822 **Mice.**

823 *Buck mice.* Female C57BL/6J (Jax 000664) mice were bred at the University of San Francisco (UCSF). All mice
824 were maintained under SPF conditions on a 12-hour light-dark cycle, at ambient temperature 21.5 + 1˚C and relative
825 humidity between 30% and 70% and provided food and water ad libitum. All mouse experiments were approved
826 by and performed in accordance with the Institutional Animal Care and Use Committee guidelines at UCSF on a
827 mouse protocol under Zachary Knight.

828

829 *Broad mice*. Female C57BL/6J (Jax 000664) mice were purchased from The Jackson Laboratory at ages 10, 36,
830 and 50 weeks. Mice were acclimated to the vivarium for 2 days ("Broad cohort 1") or 2 weeks ("Broad cohort 2")
831 upon arrival. All mice were maintained under SPF conditions on a 12-hour light-dark cycle, at ambient temperature
832 21.5 $\pm$ 1˚C and relative humidity between 30% and 70% and provided food and water ad libitum. All mouse
833 experiments were approved by and performed in accordance with the Institutional Animal Care and Use Committee
834 guidelines at the Broad Institute on a mouse protocol under H.C. and F.C.

835

836 *Yale mice.* Female C57BL/6J (Jax 000664) mice were purchased from The Jackson Laboratory at ages 8, 36, and
837 42 weeks. Mice were acclimated to the vivarium for 14 days upon arrival and maintained under SPF conditions on
838 a 12-hour light-dark cycle, at ambient temperature 21.5 $\pm$ 1˚C and relative humidity between 30% and 70%, with
839 food and water provided ad libitum. All mouse experiments were approved by and performed in accordance with
840 the Institutional Animal Care and Use Committee guidelines at Yale University on a mouse protocol under H.C.

841

842 **Estrous cycle staging mice by vaginal cytology.**

843 *Buck mice.* Mice collected at UCSF were staged near-daily for 8 consecutive days using vaginal cytology, as
844 previously described[128,129]. A total volume of 100 µL sterile saline (in 20-50 µL increments) was expelled 5-10
845 times with a P200 pipette into the vaginal canal, taking care to avoid touching the vaginal opening with the pipette
846 tip then expelled onto a glass slide and imaged immediately using Nikon Eclipse Ts2 (10X objective) and a Nikon
847 DS Qi2 camera.

848

849 *Broad and Yale mice.* Female mice were staged near-daily for 8 consecutive days using vaginal cytology, as
850 previously described[128,129]. Briefly, mini-tip flocked nasopharyngeal swabs (VWR SLIN501CS01) were moistened
851 with sterile PBS, and ~1/4th of the flocked tip was inserted into the vaginal canal of manually restrained mice. Swabs
852 were rotated 5 times clockwise, 5 times counterclockwise, and then smeared onto a non-treated glass slide (VWR
853 #16004-422). Slides were air-dried and stained with a 0.1% crystal violet solution (Jorgenson #J0322) for 1–2
854 minutes. Excess stain was rinsed with PBS and sterile water, and the slides were counterstained with 1% eosin
855 (Jorgenson #J0322A) for 10–20 seconds. Following the counterstaining step, slides were rinsed again, air-dried

856 completely, examined under a light microscope, and imaged with a Leica Aperio VERSA Brightfield, Fluorescence
857 & FISH Digital Pathology Scanner, using the 20x objective.
858
859 Cytology evaluation identified the predominant cell types (epithelial cells, cornified cells, and leukocytes), enabling
860 the classification of the estrous cycle stages (proestrus, estrus, metestrus, and diestrus) as previously described[128,129].
861 In brief, proestrus, estrus, and diestrus are characterized by a predominance of nucleated epithelial cells, cornified
862 epithelial cells, or leukocytes, respectively, while metestrus is identified by a mixture of cornified epithelial cells
863 and leukocytes[130]. The time course of the estrous cycle is in **Extended Data Table 1**.
864
865 **Tissue collection.**
866 Once identified to be in the appropriate estrous stage for collection, mice were placed under anesthesia with 3%
867 isoflurane for 1 minute and maintained via a nose cone flowing 1% isoflurane. Anesthesia was confirmed by the
868 absence of a pedal reflex. Transcardial perfusion was performed with PBS through the left ventricle to remove blood
869 from tissues before entire ovaries were removed and immediately frozen on dry ice in a cryomold containing
870 Optimal Cutting Temperature (OCT) compound. Tissues were then either processed immediately or stored at -80°C
871 for storage.
872
873 **Hematoxylin and eosin stain of adjacent histology sections.**
874 Using a Leica ST5010 Autostainer XL (Leica Biosystems), 10 µm sections from fresh frozen tissues were
875 immersed in xylene, sequentially processed through a graded ethanol series (100% and 95%), and then stained
876 with hematoxylin (Leica Biosystems 3801571). The nuclei were differentiated with mild acid treatment (Leica
877 Biosystems 3803598), followed by "bluing" through exposure to a weakly alkaline solution (Leica Biosystems
878 3802918) and subsequent water washing. Sections were then stained with Eosin (Leica Biosystems 3801616),
879 processed through a graded ethanol series (100% and 95%), xylene, dehydrated, and finally coverslipped using
880 the Leica CV5030 Fully Automated Glass Coverslipper. Brightfield images were captured with the Leica Aperio
881 VERSA Brightfield, Fluorescence & FISH Digital Pathology Scanner, using the 20x objective.
882
883 **RNA-FISH via Hybridization Chain Reaction (HCR).**
884 RNA in situ hybridization was performed on 10 µm-thick cryosections using the HCR v3.0 (Molecular
885 Instruments) for fresh frozen tissue sections with the HCR-Gold RNA-FISH kit according to the manufacturer's
886 instructions. Probes targeting mouse genes were obtained from Molecular Instruments without custom design.
887 Sections were fixed with ice-cold 4% paraformaldehyde (PFA) in PBS for 15 minutes at 4°C, then sequentially
888 immersed in 50%, 70%, 100% EtOH at room temperature, and washed with PBS. Samples were pre-hybridized in
889 50 µl of pre-warmed HCR hybridization buffer for 10 minutes at 37°C in a humidified chamber. Probe solution (2
890 µL of each probe in 100 µL HCR Hybridization Buffer) was applied to tissue sections, covered, and incubated
891 overnight at 37˚C in a humidified chamber. Sections were washed four times with pre-warmed HCR probe wash

892 buffer for 15 min each at 37˚C. For amplification, samples were pre-amplified with 50 µL of HCR Gold
893 Amplifier Buffer for 30 min at RT in a humidified chamber. Hairpins h1 and h2 (2 µL each) were heated at 95˚C
894 for 90 sec, cooled to RT in the dark for 30 min, diluted in 100 µL HCR Gold Amplifier Buffer, and 50 µL of this
895 amplification solution was added to the sample. Slides were covered and incubated overnight at RT in the dark.
896 Samples were washed four times with HCR Gold Amplifier Wash Buffer for 15 minutes each at room
897 temperature in the dark, then dried by blotting with a Kimwipe. Nuclei were counterstained with DAPI (1 µg/mL
898 in PBS, Miltenyi #130-111-570) and washed once with PBS. Autofluorescence was quenched by incubating
899 samples with TrueBlack (1x in 70% ethanol, Biotium #23007) for 1 minute at room temperature, followed by
900 three PBS washes. Samples were mounted with antifade mounting media (Thermo Fisher #P10144) and imaged
901 on an Andor Dragonfly 505 spinning disk confocal system. Images were analyzed using ImageJ software.
902
903 **Multiplexed immunofluorescence of immune markers.**
904 Fresh-frozen tissue samples were embedded in optimal cutting temperature (OCT) compound and cryosectioned
905 into 10 µm serial sections. Sections were mounted onto SuperFrost microscope slides (VWR, Cat# 48311-703)
906 and stored at −80 °C until staining. Slides were fixed in 4% paraformaldehyde (PFA) for 10 minutes, then
907 transferred to the Molecular Cytology Core Facility at Memorial Sloan Kettering Cancer Center (MSKCC). Slides
908 were blocked for 20 minutes in phosphate-buffered saline (PBS) containing 0.2% Triton X-100, 5% normal goat
909 serum (NGS), and 5% bovine serum albumin (BSA). Iterative immunofluorescence was performed on the
910 Lunaphore COMET staining platform over 11 cycles using Alexa Fluor 555- and 647-conjugated secondary
911 antibodies. Primary antibodies were applied as follows: CD11b (Abcam, Cat# ab182981, 0.125 µg/mL, 4 min
912 exposure, cycle 3), Ki-67 (Invitrogen, Cat# 14-5698-82, 1:2000 dilution, 8 min exposure, cycle 5), and CD3
913 (Roche, Cat# N03789, 1:2 dilution, 8 min exposure, cycle 9). Following COMET imaging, slides were transferred
914 to a Leica automated staining platform for antigen retrieval using pH 9 retrieval buffer for 15 minutes, followed
915 by staining with CD45 (Proteintech, Cat# 60287-1-Ig) using an Alexa Fluor 594-conjugated secondary antibody.
916 Images from both platforms were aligned for analysis.
917
918 **Single nucleus RNA sequencing.**
919 Nuclei were isolated from three frozen ovarian tissue, one from each age group at estrus, using EZ-lysis buffer
920 supplemented with recombinant RNase inhibitor (1 µL/mL). Pre-chilled douncers were prepared by washing with
921 RNase Zap, 70% ethanol, and ultrapure water. Tissue was transferred to a douncer containing 2 mL of EZ-lysis
922 buffer and homogenized with 20 strokes each of pestle A and pestle B. The homogenate was transferred to a 15
923 mL conical tube, brought to 5 mL total volume with EZ-lysis buffer, incubated on ice for 5 minutes, and
924 centrifuged at 500*g* for 5 minutes at 4°C. The pellet was washed once more with 5 mL EZ-lysis buffer using the
925 same incubation and centrifugation conditions, then resuspended in 200 µL PBS containing RNase inhibitor and
926 filtered through a 40 µm strainer. Three V4 (GEM-X) 3’ 10x channels were loaded, each channel with 20,000

927 nuclei from one sample. Reverse transcription, cDNA amplification, and library construction were conducted
928 according to the standard 10X Genomics single cell 3' V4 protocol.
929
930 ***In situ* transcriptome processing via Slide-seq.**
931 Tissue sections were processed and sequenced using Slide-seq v2 as previously described[5]. Slide-seq arrays were
932 purchased from Curio Biosciences (Curio Seeker) or prepared in-house using custom-synthesized barcoded beads
933 functionalized with the sequence[30]
934 (5'TTT_PC_GCCGGTAATACGACTCACTATAGGGCTACACGACGCTCTTCCGATCTJJJJJJJJTCTTCAGC
935 GTTCCCGAGAJJJJJJNNNNNNNNVVT30-3') with a photocleavable linker (PC), a bead barcode sequence (J, 14
936 bp), a UMI sequence (NNNNNNNVV, 9 bp), and a poly dT tail. The sample table of all Slide-seq data, denoting
937 the puck origin and other metadata, is in **Extended Data Table 2**.
938
939 OCT-embedded frozen tissue samples were warmed to -20°C, sectioned to 10 µm on a cryostat (Leica CM3050S),
940 placed on a pre-cooled Slide-seq array and melted onto the array by warming it briefly. For each sample, 2-3 sections
941 for Slide-seq were collected >200 µm to maximize sampling diversity of tissue sub-structures and consecutive
942 sections were collected for hematoxylin and eosin staining. The affixed tissue section and array was moved into a
943 1.5 mL Eppendorf tube for tissue digestion and transcriptomic library preparation as previously described[5,6]. The
944 last library amplification was performed in a final volume of 200 µL of PCR mix, divided into four 0.2 ml tubes
945 and cycled with the following program: 1 cycle of 98°C for 2 min, 4 cycles of 98°C for 20 s, 65°C for 45 s, 72°C
946 for 3 min, 9 cycles of 98°C for 20 s, 67°C for 20 s, 72°C for 3 min, and 1 cycle of 72°C for 5 min. Libraries were
947 sequenced using the following read structure on a NextSeq 1000/2000 (P2; Illumina) or NovaSeq (S4 or X;
948 Illumina): Read1: 42 bp; Read2: 50bp; Index1: 8 bp, and sequences were processed as previously described[5] using
949 the pipeline available at (https://github.com/MacoskoLab/slideseq-tools).
950
951 **Hematoxylin and eosin stain of adjacent histology sections.**
952 Serial sections of 10 µm thickness were obtained from the frozen tissue samples and mounted onto glass microscope
953 slides (VWR SuperForst 48311-703). Using a Leica ST5010 Autostainer XL (Leica Biosystems), sections were
954 immersed in xylene, sequentially processed through a graded ethanol series (100% and 95%), and then stained with
955 hematoxylin (Leica Biosystems 3801571). The nuclei were differentiated with mild acid treatment (Leica
956 Biosystems 3803598), followed by "bluing" through exposure to a weakly alkaline solution (Leica Biosystems
957 3802918) and subsequent water washing. Sections were then stained with Eosin (Leica Biosystems 3801616),
958 processed through a graded ethanol series (100% and 95%), xylene, dehydrated, and finally coverslipped using the
959 Leica CV5030 Fully Automated Glass Coverslipper. Brightfield images were captured with the Leica Aperio
960 VERSA Brightfield, Fluorescence & FISH Digital Pathology Scanner, using the 20x objective.
961
962 **Pre-processing of single nucleus and spatial transcriptomics data.**

963 Raw sequencing reads were demultiplexed using Cellranger (v.6.1.2) mkfastq (10x Genomics)[131] and aligned to
964 the mouse mm10 reference genome using STAR v2.7.8a with default parameters[132]. For spatial data, spatial
965 barcode assignment and bead-based feature extraction were performed using the Slide-seq pipeline (v2022-01-01)
966 and represented as a gene-by-spot expression matrix directly within the Slide-seq pipeline for downstream
967 analyses[5,6].
968
969 **Initial data processing.**
970 Gene expression data of individual samples or pucks were concatenated using an outer join. For spatial data, spatial
971 coordinates were assigned by matching barcodes from puck-specific barcode matching files. Metadata, including
972 puck and sample IDs, estrous stage, and animal age category, were appended to the AnnData object. The combined
973 dataset was filtered to retain spots with at least 50 detected genes and 150 UMI counts. For spot clustering and
974 embeddings, all gene expression values were scaled and centered. The top 5,000 highly variable genes were
975 identified from log-normalized counts across all batches using Scanpy's highly_variable_genes function (batch
976 key=puck)[133]. Dimensionality reduction was conducted by first regressing out total UMI counts on log-normalized
977 counts, then conducting principal component analysis (PCA) on highly variable genes, followed by correcting for
978 puck-specific batch effects using a PyTorch implementation of Harmony[134], then constructing a nearest-neighbor
979 graph with k=10 neighbors using the top 40 principal components. Unsupervised clusters of spots were identified
980 with the Leiden algorithm[135] (resolution=1.5) and visualized using UMAP[136], all implemented in Scanpy[133]
981 (v1.10.1).
982
983 *Smear removal.*
984 Smearing artifacts were manually identified and removed using an interactive selection tool. Spatial scatter plots
985 were generated using Squidpy to visualize cell spots color-coded by cluster identity[137]. Using an interactive
986 LassoSelector widget, regions of spots suspected of containing technical artifacts were removed and excluded from
987 further analyses. This process was repeated for each puck, resulting in refined AnnData objects free from smear
988 artifacts. Following smear removal, the dataset was re-processed to refine dimensionality reduction and clustering
989 as described above, resulting in a total of n=601,831 spots from 68 spatial transcriptomes.
990
991 **Projection of additional pucks.**
992 To incorporate additional Slide-seq data into the existing reference atlas, raw gene-by-spot matrices from newly
993 generated pucks (young, metestrus stage) were first pre-processed as described above. Briefly, spatial coordinates
994 were assigned, metadata were appended, and smear artifacts were removed using the same interactive lasso-based
995 filtering procedure.
996
997 To ensure compatibility between the query puck and the reference atlas, we harmonized the gene sets prior to
998 integration. Specifically, genes present in the reference but absent in the query, as well as query-only genes, were

identified. The query AnnData object was then subset and reordered to the intersection of reference and query genes, yielding a matched feature space for projection. The cleaned query AnnData was projected onto the existing atlas using scvi-tools (v1.1.6) to learn a shared latent representation. The pretrained SCVI model was reloaded and the query puck was registered as a new dataset. Latent embeddings for the query were obtained and concatenated with reference embeddings for downstream analysis.

For label transfer, scArches[138] (v0.6.1) was used to adapt the pretrained SCVI model via the unsupervised surgery pipeline as described in the scArches documentation. This enabled alignment of the query data with the harmonized latent space and probabilistic annotation transfer. Spot-level labels were assigned for both fine-grained and major cell type categories. To increase annotation robustness, low-confidence calls were masked using an uncertainty threshold of 0.2. Spatial segmentation was performed as described below.

Unsupervised clustering and cell type annotation.

Cell types were annotated using top differentially expressed genes (DEG) identified for each Leiden cluster and cross-referenced with established marker genes from literature[37,40,125,139–145]. DEGs were identified using Scanpy's rank_genes_groups function with the Wilcoxon rank-sum test to detect cluster-specific marker genes. Spatial scatter plots and UMAP embeddings were used to visualize marker gene expression and confirm cluster-specific identities. Granulosa cells (GCs) were further subclustered by re-running Leiden clustering on GC subsets, followed by DEG analysis and marker-based assignment. The top 50 marker genes identified for each cluster are in **Extended Data Table 3**.

Immune and granulosa cell subclustering

To refine annotation of specific populations, we performed iterative subclustering of immune cells and granulosa cells (GCs). First, AnnData objects were subset to include only the cell types of interest (e.g., Immune, atretic GCs). Raw counts were normalized to a total of 10,000 transcripts per cell with highly expressed genes down-weighted (max_fraction=0.05), followed by log-transformation. Highly variable genes were identified using Scanpy's highly_variable_genes function (flavor="seurat", batch_key="segment_label"), and the data were scaled to unit variance with a maximum value of 10. Principal component analysis (PCA) was then performed on the highly variable gene set, and neighborhood graphs were constructed using the top 50 PCs as input.

UMAP embeddings were generated for visualization, and Leiden clustering was used to define subclusters within each subset. Differentially expressed genes (DEGs) were identified for each subcluster using the Wilcoxon rank-sum test (min log fold-change ≥ 1) on normalized counts. For annotation, we required that selected DEGs be (i) specific to the cluster, (ii) highly expressed across the majority of cells within that cluster, and (iii) supported by prior literature as having cell type–defining functional roles. Representative markers were visualized using dot plots to confirm specificity and coverage.

1035

1036 For immune cells, the first round of subclustering resolved broad classes including macrophages, T cells, plasma
1037 cells, dendritic cells, and mast cells. Because macrophages formed a large and heterogeneous population, we
1038 performed a second round of subclustering restricted to this compartment, which enabled identification of
1039 functionally distinct macrophage subtypes supported by known marker genes. A similar iterative approach was
1040 applied to GCs (**Extended Data Fig. 1b)**. Broad subclustering resolved major GC states, after which the atretic
1041 GC compartment was isolated and re-clustered separately. This refinement revealed transcriptionally distinct
1042 atretic GC subpopulations, consistent with prior descriptions of heterogeneity in follicular atresia. For a detailed
1043 description of the iterative subclustering strategy, DEG-based marker selection, and literature-based justification
1044 for GC and immune subtype annotation, see **Supplementary File 1**. The top statistically ranked DEGs for each
1045 GC subcluster are provided in **Extended Data Table 3**.

1046

1047 **Comparison of luteal populations with published datasets.**

1048 To assess the concordance of our luteal populations with previously published corpora lutea (CL) classifications,
1049 we compared our data to the well-annotated single-cell RNA-seq dataset from Morris et al. (2022)[37]. Raw clustered
1050 AnnData objects were obtained and reprocessed. For clarity, we excluded the "Regressing CL" cluster reported in
1051 Morris et al. as this population originates from post-partum ovaries, which were not part of our study design. Cell
1052 type composition was quantified using contingency tables of cluster identity against estrous stage. To directly
1053 compare gene expression profiles, we visualized differentially expressed genes (DEGs) in luteal subtypes identified
1054 in both our dataset and Morris et al. (2022) as dotplots. Gene-level concordance was assessed by overlapping marker
1055 sets and expression distributions across annotated luteal subtypes.

1056

1057 **Spatial segmentation of oocytes, follicles, and CL.**

1058 Code underlying these analyses can be found in II.2_segmentation.ipynb and II.3_segment_extension.ipynb.

1059

1060 *Oocyte segmentation.*

1061 We defined spots in the 'Oocyte' or the 'Oocyte - cumulus' spot cluster as putative oocyte spots. 'Oocyte - cumulus'
1062 spots were included in initial segmentation to ensure robustness against variations in cluster boundaries between
1063 'Oocyte' and 'Oocyte - cumulus' spots but were subsequently removed from the final oocyte segments as described
1064 below. For each puck, a spatial neighborhood graph of putative oocyte spots (radius=50) was constructed and
1065 clustered with the Leiden algorithm[135] (resolution=0.1) to define preliminary oocyte segments. 'Oocyte - cumulus'
1066 spots were then removed from these segments. Segments containing fewer than three spots were also discarded.
1067 Final oocyte segments were further refined through subclustering, merging, and manual curation based on tissue
1068 context. Details of these curation choices are documented in the supplementary code.

1069

1070 *Additional decontamination of cumulus spots from oocyte spots.*

1071 Non-negative matrix factorization (NMF)[146] was used to identify gene programs corresponding to cumulus cell
1072 contamination in spots labeled as oocyte from Leiden clustering. scikit-learn[147] was used to perform NMF with k=8
1073 programs on log1p normalized counts. Programs 1 (*Kctd14*, *Slc18a2*, *Wt1*), 2 (*Lars2*, *Hexb*, *Cdk8*), 4 (*Inhba*, *Inhbb*,
1074 *Nap1l5*), and 6 (*Col1a2*, *Col3a1*, *Cfh*) were identified as contaminating signals based on their constituent genes
1075 (**Extended Data Fig. 7a**). Spots were annotated as contaminants if they either had these programs as their top
1076 utilized program or if the program scores reached the following thresholds: Program 1: > 0.4, Program 2: > 0.3,
1077 Program 4: > 0.3, Program 6: > 0.4 (**Extended Data Fig. 7b**). Spots annotated as contaminants were removed from
1078 the object before a second round of decontamination was performed on remaining spots using NMF with k=8
1079 programs. Program 1 (*Serpine2, Ccnd2, Kctd14*) was identified as a contaminating signal based on its constituent
1080 genes (**Extended Data Fig. 7c**). Spots that had this program as the top utilized program, or had a program score
1081 >0.3 were annotated as contaminants (**Extended Data Fig. 7d**) and removed from the oocyte segments for the
1082 computation of these averages.
1083
1084 *Identifying primordial oocytes.*
1085 To identify any remaining small, putatively primordial, oocytes, unassigned spots labeled as 'Oocyte' or expressing
1086 primordial oocyte marker gene *Sohlh1*[36,55] that were at least 200 from an oocyte segment center were selected. A
1087 spatial neighborhood graph of these putative primordial oocyte spots for pucks containing at least two such spots
1088 using a radius of 20 µm to account for the expected small size of these primordial oocytes. Oocyte segments were
1089 identified after Leiden[124] clustering (resolution=0.1). Spots labelled as 'Oocyte - cumulus' were removed from these
1090 segments. Segments containing less than 2 spots or lacking *Sohlh1* expression were excluded.
1091
1092 *Segmentation of follicles and corpora lutea.*
1093 Spots in the 'Cumulus – oocyte', 'GC – preantral', 'GC - antral early mitotic', 'GC - antral luteinizing', 'GC - antral
1094 mitotic', 'GC – atretic' clusters were defined as putative follicle spots, while spots in the 'Luteal - early', 'Luteal -
1095 late' clusters were defined as putative CL spots. A spatial neighborhood graph of the putative follicle and CL spots
1096 (radius 50 µm) was constructed and clustered with Leiden[135] (resolution=0.1 for follicles and a smaller
1097 resolution=0.001 for CLs because they tended to be larger) for each puck, yielding segments. Segments with less
1098 than 20 spots were removed, the remaining were then subclustered and merged as appropriate based on manual
1099 inspection. These curation choices are documented in the supplementary code. Segments were then extended to
1100 include additional spots from the selected GC or luteal cell types, respectively, within 50 µm of a spot already
1101 assigned to a segment or the next closest segment if multiple were within 50 µm.
1102
1103 In a few cases, oocyte segments had been identified by the above oocyte segmentation but the corresponding follicle
1104 was either too small or irregular, resulting in partial or complete omission by this follicle segmentation pipeline. To
1105 address these cases, unassigned spots from the above selection of follicle cell types within 50 µm of an oocyte
1106 segment were assigned as follicle segments and grouped based on the closest oocyte segment. If these new follicle

1107 segments were closer than 100 µm (minimal spot-spot distance across a segment pair) to existing follicle segments,
1108 the segments were merged.
1109
1110 To capture remaining small follicles, unassigned spots in the 'Cumulus – oocyte', 'GC – preantral', 'GC - antral
1111 early mitotic', and 'GC – atretic' spot clusters were defined as mapping to putative small follicles. Within each
1112 puck, one spatial neighborhood graph was each constructed for these putative follicle and CL spots (radius 20 µm)
1113 and clustered with Leiden (resolution=0.1), resulting in additional segments. Segments with less than 5 spots
1114 assigned were removed. Remaining segments were merged with existing follicle segments if they were within 50
1115 µm of existing segments (minimal spot-spot distance across segment pair). The final segments were further
1116 subclustered, merged, and reassigned to proximal oocytes as appropriate. These curation choices are documented
1117 in the supplementary code.
1118
1119 *Assigning proximal spots to segments.*
1120 Immune ('Immune'), endothelial (all 'Endothelial' types), theca ('Theca' and 'Stromal - steroidogenic'), and
1121 mesenchyme ('Adipocyte', 'Stromal - nonsteroidogenic') spots were assigned to follicle or CL segments that were
1122 less than 100 µm away.
1123
1124 *Assigning oocytes to follicles.*
1125 Oocyte segments were assigned to the closest follicle segment if it was less than 100 µm away. These assignments
1126 were manually curated where appropriate based on manual inspection of the segmentation results and the
1127 surrounding tissue; these curation choices are documented in the supplementary code.
1128
1129 **Follicles and corpora lutea segments labeling.**
1130 First, segments were assigned as follicle or CL: CL segments were classified as those in which the most frequent
1131 spot type was a luteal type, or where the sum of the fraction of luteal types out of above granulosa (GC) and luteal
1132 types was larger than 50%; all remaining segments were classified as follicles. (**Extended Data Fig. 1g, h**). Note
1133 that this classification was performed on all segments from both the follicle and CL segmentation above to recover
1134 exceptional cases in this initial segmentation. Second, more specific state labels were assigned to the resulting
1135 follicle and CL segments. Follicle segments were labelled as 'Follicle – atretic' if more than 20% of their assigned
1136 spots were classified as 'GC – atretic'. All other follicle segments were classified based on their most abundant GC
1137 type ('GC – preantral' as 'Follicle – preantral', 'GC – antral luteinizing' as 'Follicle – antral luteinizing', 'GC –
1138 antral early mitotic' and 'GC – antral mitotic' as 'Follicle – antral mitotic'). CL segments were classified as 'CL -
1139 early' and 'CL – late' based on their majority luteal cell type.
1140
1141 **Validation of the segmentation pipeline with manually segmented adjacent H&Es.**

1142 To validate the segmentation pipeline, adjacent H&E-stained sections were annotated for preantral follicles, antral
1143 follicles, and corpora lutea. Annotated H&E sections were then compared to spatial plots of segmented objects,
1144 with 'follicle - antral luteinizing','follicle - antral mitotic', and 'follicle - atretic' combined into a single 'follicle -
1145 antral' category, as by histology of fresh frozen sections these categories can not be distinguished. For all young
1146 sections, follicles were annotated as being consistent between the spatial plot and H&E (89.6%, **Fig. 1e,f,**
1147 **Supplementary File 2,3**) or annotated if there was a mismatch between the two sections. Differences in annotations
1148 between the adjacent H&E section and Slide-seq section are mostly due to structures that are not present in both
1149 sections–for example, the edge of a follicle was captured in the sequenced section, and the adjacent section that was
1150 H&E stained does not contain any cells from that follicle (**Supplementary File 2,3**). The remaining discrepancies
1151 are the result of separate follicles being segmented as a single object (7.9%), an incorrect segment identity being
1152 assigned (0.6%), and the segmentation pipeline not detecting an object (1.9%) (**Fig. 1f**). Cohen's kappa was
1153 calculated with scikit-learn[147]. Follicle counts and error types were plotted using GraphPad Prism version 10.0.0.
1154

1155 **Calculating mean expression profiles of oocyte, follicle and CL segments.**

1156 Raw (unfiltered and un-normalized) counts of spots assigned to a segment (either oocyte, follicle, or CL were
1157 normalized per spot to 10,000, then averaged within each segment. Where appropriate, the resulting segment
1158 expression profiles were log1p transformed for downstream analyses.
1159

1160 **Trajectory inference of GCs.**

1161 Trajectory inference of GCs was performed using diffusion pseudotime (DPT), a graph-based method that models
1162 cellular transitions along a continuum, as described in previous single-cell RNA-seq studies[148]. DPT analysis was
1163 conducted on annotated GCs after dimensionality reduction using principal component analysis (PCA). A k-nearest
1164 neighbor (k-NN) graph was constructed using the top 40 principal components, with k set to 10, to define local
1165 cellular neighborhoods. Diffusion components (DCs) were computed from the neighborhood graph to capture the
1166 structure of cellular transitions in high-dimensional space. The root of the trajectory was manually selected based
1167 on inspection of DC embedding. DPT values were calculated in two complementary ways, depending on the
1168 analysis. For Fig 3d., pseudotime was computed separately for GC spots in non-atretic and atretic follicles to analyze
1169 spatial patterns of trajectories in follicles under developmental versus degenerative conditions. For Fig 3h., DPT
1170 was computed across all GC spots combined to provide a single ordering of granulosa cell states across the follicular
1171 lifecycle and facilitate comparison across follicle types, estrous cycle stage, and age (**Extended Data Fig. 3g**).
1172

1173 **Calculation of cell cycle scores.**

1174 To assess cell cycle dynamics in annotated granulosa cell spots in mice, canonical markers of S-phase and G2/M-
1175 phase, as previously described[149], were used to calculate cell cycle phase scores. Based on these scores, spots were
1176 classified into three phases: G1, S, or G2/M. Spots classified as G1 were further categorized as "Non-Cycling,"
1177 while spots in S or G2/M phases were categorized as "Cycling." This classification was integrated with spatial

1178 transcriptomic data to map the cycling status of annotated granulosa spots. Dimensionality reduction methods were
1179 applied to visualize cell cycle phases in relation to spatial organization in tissues, enabling an analysis of
1180 proliferative activity within granulosa cell-associated regions of the ovary.
1181
1182 **Radial distance analysis within segments.**
1183 To examine spatial trends in our analysis, radial distances for spots within follicular segments were computed. The
1184 radial distance for each spot was calculated as the Euclidean distance from the centroid of the segment, scaled by
1185 the maximum segment radius. This normalized distance, referred to as the "scaled radial distance," enabled a
1186 standardized comparison of spatial patterns across segments of varying sizes. Spots were binned along the scaled
1187 radial distance into equal intervals spanning the range [0, 1] (**Extended Data Fig. 3a**).
1188
1189 For each radial bin, the mean and standard error of the mean (SEM) of various features such as cell type
1190 composition, DPT and cell cycle scores, cNMF-derived gene program usage were first calculated across individual
1191 bins. Each mean and SEM were then aggregated for each distance bin within the same segment type. Segment-
1192 specific trends were then visualized by plotting the mean proportions or cNMF program scores for each distance
1193 bin, with shaded regions representing the SEMs.
1194
1195 To evaluate spatial trends in various features across scaled radial distance bins, the monotonic relationship between
1196 the radial bin index (independent variable) and the mean values of the feature of interest (e.g., cell type composition,
1197 cell cycle state, DPT, or cNMF program usage) for each segment type was assessed using Spearman rank
1198 correlation. For each segment type, the mean feature values within each radial distance bin were calculated as
1199 described above and correlated with the corresponding radial distance bins to determine whether the feature of
1200 interest varied systematically with distance from the segment centroid. Spearman correlation was chosen for its
1201 robustness in detecting monotonic relationships, regardless of the underlying distribution or linearity. The Spearman
1202 correlation coefficient (ρ) and associated p-value were calculated using the SciPy library. Bins with fewer than two
1203 data points were excluded from the analysis.
1204
1205 **Identifying gene programs with non-negative factorization.**
1206 *Oocytes.*
1207 Gene programs in composite oocytes were identified using scikit-learn[147] to perform non-negative matrix
1208 factorization (NMF)[146]. Log-normalized counts were used for NMF (k=5 programs) to reduce the noise of highly
1209 expressed genes in composite oocytes that were composed of few oocyte spots. To interpret the biological relevance
1210 of the gene programs, genes were ranked for each program by their contributions to the gene weight matrix. Program
1211 usage across oocytes were visualized using PCA embeddings.
1212
1213 *Granulosa cells (GCs).*

Gene programs in GCs were identified using consensus non-negative matrix factorization (cNMF), following the workflow described by Kotliar et al[76]. Using raw gene expression counts as input, 5,000 highly variable genes (HVGs) were identified by calculating gene variance across spots during preprocessing with the top 5,000 HVGs retained for downstream analyses. Batch correction was incorporated directly into the cNMF pipeline using an adapted version of Harmony[134] and the resulting corrected matrix, with negative values set to zero, resulting in the batch-corrected matrix used for factorization. cNMF was run on the corrected matrix to factorize the expression data into two components: a gene weight matrix, in which each gene is associated with specific programs, and a usage matrix, in which each spot is assigned a score reflecting its degree of program activity. The number of programs (k) was set to 16 to balance program stability and error, calculated as the Pearson correlation between factorization results across 20 replicates for each k. For the selected k, cNMF was re-run with 200 replicates to generate final consensus matrices and extract robust and biologically meaningful programs.

To interpret the biological relevance of the gene programs, genes were ranked for each program by their contributions to the gene weight matrix (**Extended Data Fig. 3f**). Program activity scores were normalized per spot by dividing the raw usage matrix values by the total program activity per spot. Spots were grouped by their dominant GC program, defined as the program with the highest normalized usage score, to assess program separation and overlap (**Extended Data Fig. 3d**). Gene programs were annotated by comparing the top contributing genes against known GC markers and enriched functional pathways from the literature[14,17,25,150,151].

Analysis of gene expression programs (GEP) with pseudotime.

To investigate transcriptional dynamics during follicle development and atresia, we analyzed cNMF-derived GEP usage scores ordered along diffusion pseudotime (DPT). As described above, DPT was calculated as a unified trajectory across all GC spots. Stage stream plots depict the distribution of follicle type occupancy along pseudotime. For each type, Gaussian kernel density estimates (KDEs) of pseudotime values were computed across a grid of 400 points, normalized at each position, and displayed as stacked area plots. Estrous phase lanes (second row, when available) were generated analogously for estrus and metestrus and plotted as a two-band stackplot to visualize stage occupancy along pseudotime. GEP heatmaps were generated separately for GC spots within non-atretic and atretic follicles. Pseudotime was divided into 500 equal-width bins, and average GEP usage scores were computed per bin.

For each GEP, and within each follicle type and estrous stage, we tested for differences between young and old ovaries using ordinary least squares (OLS) regression with cluster-robust standard errors. Specifically, for each stratum we fit the model Usage_k ~ Age (with young as the reference) and extracted the p-value for the coefficient corresponding to old. Robust variance estimates were clustered by puck to account for within-puck correlation of spots. Strata lacking both age groups were returned as not estimable. Across all tested GEP × follicle type × stage combinations, p-values were adjusted for multiple testing using the Benjamini–Hochberg procedure, and

significance was defined at FDR < 0.05. Significance panels adjacent to the heatmaps summarize the results: white = not significant, light gray = significant in Estrus only, dark gray = significant in Metestrus only, black = significant in both stages. Stars indicate the adjusted significance level ($q < 0.05$, $q < 0.01$, $q < 0.001$). Analyses were performed using pandas for data handling and statsmodels for regression and multiple testing correction (statsmodels.formula.api.ols, statsmodels.stats.multitest.multipletests).

For alternative visualization of this analysis (**Extended Data Fig. 3g**), we also summarized program activity for each cNMF program (Usage_1–Usage_16) using a three-level averaging scheme to respect biological replication. First, GEP usage scores were averaged within each follicle segment (segment_id) to obtain follicle-level profiles. Second, segment means were averaged within each puck (puck) for each follicle type, estrous stage, and age. Third, puck-level means were averaged across pucks to yield the final condition means for Age × Stage × Follicle type. We then constructed an interleaved categorical axis ordered as Age → Follicle type → Stage to enable side-by-side comparisons across ages within each follicle type and stage.

Compositional analysis of cell and segment types.

Global cell-type compositional analysis.

The spot composition for each cell type was calculated for each puck. Mean composition was then calculated for young, middle, and old ages for each cell type. To determine significance of cell composition changes with age, the scCODA package was used[120], with young used as the control group, and epithelial – oviduct as the reference cell type, as its composition has low variation across conditions. Subsets of immune spots were created based on their segment assignments to follicles or CL, or stroma if unassigned. Endothelial spots localized to CL were subset from other endothelial spots.

Cell-type composition within segments analysis.

For each relevant predicted cell type, the fractional composition was computed as the proportion of spots assigned to that cell type within each segment. The mean and standard error of these fractions were calculated across segments and grouped by distinct segment types. These results were used to analyze patterns in cell type composition and visualize the relative contributions of different cell types and segments.

To statistically compare across follicle type and age, we applied a compositional regression framework in which cell type proportions were transformed using a centered log-ratio (CLR) to account for the closed-sum nature of compositional data. For each cell type within each follicle type, we fit ordinary least squares models of the form CLR ~ Age, using cluster-robust standard errors (clusters = puck) to account for within-sample correlation. Age effects (Young as reference) were tested for each cell type and follicle type, and p-values were adjusted using the Benjamini–Hochberg procedure. Significance was defined at FDR < 0.10. For visualization, mean ± s.e.m.

1285 immune subtype proportions were plotted for Young, Middle, and Old ovaries, with colors denoting age groups
1286 and asterisks indicating significance levels (q < 0.05, *q < 0.01, *q < 0.001, •q < 0.10).
1287
1288 *Segment type composition analysis.*
1289 The relative abundances of different segment types, including follicular and corpus luteum segments, was
1290 analyzed across estrous stage and animal age. The proportions of each segment type (e.g., preantral, antral mitotic,
1291 antral luteinizing, and atretic segments) were calculated as the fraction of individual segments of the same
1292 segment type within each sample (puck). Mean fractions and standard errors were computed across pucks for each
1293 experimental condition, grouped by estrous stage and animal age. Statistical differences between the fraction of a
1294 particular segment type across different groups of pucks were assessed with t-tests, and significant differences
1295 were highlighted in visualizations.
1296
1297 **Follicle embedding and trajectory inference using optimal transport.**
1298 Code underlying these analyses can be found in III_segment_OT_1_pca_coretypes.ipynb and
1299 III_segment_OT_2_plot_results.ipynb.
1300
1301 *Segment-to-segment distance matrix computation.*
1302 A distance matrix was computed between any pair of segments of all follicle and CL segments in young mice. For
1303 each segment, oocyte, granulosa or luteal spots, and theca spots were considered. A transport matrix from spots in
1304 any pair of segments was calculated with optimal transport, using the Sinkhorn algorithm implemented in moscot[92]
1305 (epsilon=0, tau_a=1., tau_b=1., rank=20, initializer=k-means, min_iterations=5, max_iterations=200). This
1306 transport matrix was multiplied elementwise with the cost matrix of the optimal transport problem and the sum over
1307 all elements in this resulting matrix was used as a distance measure between the two segments.
1308
1309 *Segment embedding and follicle pseudotime.*
1310 This segment-to-segment distance matrix was treated as a segment feature space. The k-nearest neighbor graph of
1311 segments (k=15) was built from the top 50 PCAs computed and embedded as a UMAP. This embedding was
1312 generated both for the union of all follicle and CL segments in young mice, and for follicles in young mice alone.
1313 Diffusion pseudotime[148] was then computed for follicles in young mice based on a manually defined root segment.
1314
1315 *Trajectory projection of follicles from middle-aged and old mice.*
1316 A distance matrix was calculated between all follicle and CL segments in young mice and middle and old mice,
1317 using the same optimal transport approach as above. Each segment from middle and old mice was then assigned to
1318 its closest neighbor in young mice based on this distance. Follicles from middle and old mice were then assigned
1319 the pseudotime coordinates from their closest neighbor follicle in young mice.
1320

Cell–cell communication analysis.

Code underlying these analyses can be found in III.5_nichenet_ageYoung_stageAll_segmentFollicle_withOocyte_byCluster.Rmd and III_segment_OT_2_plot_results_v0.3.ipynb.

Cell-cell communication analysis was performed with MultiNicheNet[93] on data from young mice, with follicle segments considered as samples for the purpose of the algorithm. Comparisons were performed between different follicle labels, using coarse cell type labels (preantral, antral, atretic). Oocyte, granulosa, theca, and immune spots were included in this analysis. Ligand-receptor pairs and receiver-sender cell type pairs specific to each follicle label were prioritized accordingly. Follicles that did not meet default cell type compositional thresholds were discarded (at least 5% of spots per segment mapping to each cell type). To characterize the communication states across all follicles, a summarized ligand-receptor score was calculated for each segment. This score was derived first by calculating the mean of normalized expression of receptor and ligand pairs for all cell types within a segment, log1p transforming, and then summed to generate the final segment specific ligand and receptor score.

Immune infiltration analysis.

To compare the infiltration of immune cells across segment types, immune spot composition was analyzed relative to distance from the segment center. For each scaled radial distance bin (calculated as described above) within individual segments, the proportion of immune spots was calculated by dividing the number of immune spots by the total number of spots within each bin. The average immune composition and standard error of the mean (SEM) for each distance bin were determined for every segment type to assess systematic variation with distance from the segment center. Tukey's Honest Significant Difference (HSD) test was applied to evaluate the monotonic relationship between the radial bin index (independent variable) and the mean values of the feature of interest (dependent variable) for each segment type. To address potential bias from tissue sectioning, additional analysis was conducted on oocyte-containing follicles to confirm that slicing artifacts did not affect the evaluation of radial infiltration (**Extended Data Fig. 1j**). Statistical comparisons and p-values were calculated using the SciPy library. Radial bins with fewer than two data points were excluded from both statistical and visualization analyses.

Age-associated differential gene expression analysis.

Follicles.

To analyze key hormone gene changes across young and old follicles, mean gene expression was calculated as described above. For each segment type (preantral, antral mitotic, antral luteinizing, and atretic follicles), stage (Estrus, Metestrus) and age, mean and SEM of gene expression were calculated for the hormone-related genes *Amhr2*, *Fshr*, *and Lhcgr*[47] . Differential expression analysis between estrous stages was performed using two-sided t-test.

1357 *Oocytes.*
1358 Primordial oocytes were removed from analysis due to the low representation in old animals. Genes were filtered
1359 to remove those expressed in less than 10% of oocytes. Differential expression analysis was performed using Scanpy
1360 on young and old oocytes, using log1p normalized data using t-test with overestimated variance and using the
1361 Benjamini-Hochberg correction method. Genes with a p-value <0.05 and a log2 fold change >1 were used for further
1362 analysis.
1363
1364 *Stromal cells.*
1365 Stromal cells including spots labeled as fibroblasts, stromal – nonsteroidogenic, and stromal – steroidogenic were
1366 used for differential expression analysis. Genes were filtered to remove those expressed in less than 10% of spots.
1367 Differential expression analysis was performed using Scanpy on young and old spots, using raw counts using t-test
1368 with overestimated variance and using the Benjamini-Hochberg correction method. Genes with a p-value <0.05 and
1369 a log2 fold change >1 were used for further analysis.
1370
1371 **Identifying multi-nucleated giant cells (MNGCs).**
1372 Code underlying these analyses can be found in II.5_registration_v0.8_all_pucks.ipynb and
1373 III_MNGC_dotplot_v0.1.ipynb.
1374
1375 *Annotation of MNGCs in histology sections.*
1376 Manual annotation of histology sections adjacent to sections used for Slide-seq analysis were used to classify the
1377 presence of multi-nucleated giant cells (MNGCs) based on pigmentation, size, and proximity to a growing follicle
1378 as previously described[11,33,114,115,152]. H&E stains with a high density of light brown clusters, generally surrounding
1379 growing follicles, were categorized as "visible MNGCs" (19 samples). Sections with lighter pigmentation and a
1380 lower density of clusters were categorized as "possible MNGCs" (13 samples). Samples lacking visible
1381 pigmentation were labeled as "no MNGCs."
1382
1383 *Segmentation of MNGCs in H&E and registration with spatial transcriptomics data.*
1384 Samples deemed to contain MNGCs upon visual inspection of the H&E images were selected for segmentation.
1385 H&E images and spot transcriptomics were registered using a napari plugin in squidpy[137], with anchor points
1386 manually defined at tissue features clearly visible in both (such as large oocytes or points on the edges of the tissue
1387 section). In this registered space, spots within MNGC regions were segmented based on histology and spot
1388 transcriptomics. For the analysis of immune cells in stroma and MNGC, all immune spots outside of follicle or
1389 corpus luteum segments were selected and classified as "stromal" (outside of MNGC segments) and "MNGC"
1390 (inside of MNGC segments).
1391
1392 **Co-localization analysis of segmented tissue structures.**

Code underlying these analyses can be found in III_segment_colocalization.ipynb. Within each puck, a spatial neighborhood graph of follicles was constructed to represent each follicle by the spatial center point of its constituent spots. Neighborhood enrichment was performed on this graph with Squidpy[137] within homotypic follicles (preantral, antral, and atretic) with varying radius from 200 µm to 2000 µm in steps of 200 µm.

Measurement of surface epithelium thickness.
To validate the findings of increased abundance of surface epithelial cells in old animals, surface epithelium thickness was measured using ImageJ[153]. For each section, three thickness measurements were taken and averaged. A single section was measured for each ovary and plotted using GraphPad Prism version 10.0.0.

Lead contact. Further information and requests for resources and reagents should be directed to and will be fulfilled by the lead contact, Hattie Chung (hattie.chung@yale.edu)

Data availability. All sequencing data (Slide-seq) and expression count matrices (Slide-seq) will be deposited in Gene Expression Omnibus and the cellxgene portal prior to publication.

Code availability. All code is available at https://github.com/HattieChungLab/ovarian_aging

Author contributions
H.C. and J.G. designed the study. H.C., A.K., I.B., and S.M. conducted the pilot experiment and analysis. A.K., H.C., and T.C.T.L. conducted the mouse work. G.M. created in-house Slide-seq tiles with supervision from F.C. R.R., T.C.T.L., and H.C. conducted Slide-seq experiments. R.R. and T.C.T.L conducted histology experiments and imaging. R.R. processed all Slide-seq data. T.C.T.L. and A.K. conducted cell type clustering and annotation under supervision by H.C., D.S.F., A.K.S., and P.C.S. D.S.F. designed and implemented the segmentation pipeline, optimal transport, and cell-cell interaction analyses. D.S.F., R.R., and R.S. conducted computational histology analyses. H.C. and D.S.F. designed and supervised all other analyses conducted by T.C.T.L., A.K., S.S., A.M., and H.T. H.C. and J.G. supervised the overall project. T.C.T.L., D.S.F., A.K., R.R., S.S., and H.C. interpreted the results with input from all authors. T.C.T.L., A.K., D.S.F., J.G., and H.C. wrote the paper with input from all authors. T.C.T.L. and A.K. contributed equally.

Acknowledgments
This work was funded by a Pilot Grant from the Productive Health Global Consortium (formerly GCRLE) awarded to H.C. H.C. also acknowledges support from start-up funds from Yale University and the NIH (R35 GM160070). T.C.T.L. is in part supported by the Productive Health Pilot Grant awarded to H.C. D.S.F. is supported by the Eric and Wendy Schmidt Center fellowship at the Broad Institute. J.L.G. and A.K. are supported by the NIH (R35 GM145305). We thank Anubhav Sinha for helpful discussions on HCR, and Sami Farhi and the Spatial Technology

Platform for allowing us to use their Dragonfly. We thank Murray Tipping, Francesca Mazzoni, and Wenfei Kang at MSKCC. We thank the Broad Institute vivarium staff, especially Nathan Chan, for assistance with vaginal cytology. We thank Nicholas S. Moore for helpful feedback on the manuscript, and all members of the Chung and Garrison Labs and Francesca E. Duncan for helpful discussions.

Competing interest declaration

A.K.S. reports compensation for consulting and/or scientific advisory board (SAB) membership from Honeycomb Biotechnologies, Cellarity, Danaher, Ochre Bio, Bio-Rad Laboratories, Relation Therapeutics, IntrECate biotherapeutics, Parabalis Medicines, Passkey Therapeutics and Dahlia Biosciences unrelated to this work. P.C.S. is a co-founder of Sherlock Biosciences and Delve Biosciences, a board member of Polaris Genomics, a former board member of Danaher Corporation, and a former scientific advisory board member of NextJenGane, and holds equity in the companies unrelated to this work. F.C. is a founder of Curio Bioscience and Doppler Bio. All other authors report no potential conflicts.

Supplemental Information

Extended Data Figures 1-7

Extended Data Tables 1-6

Supplementary Files 1-3

1448 **References**

1449 1. Bieuville, M. *et al.* Number of lifetime menses increases breast cancer occurrence in postmenopausal
1450 women at high familial risk. *Front. Ecol. Evol.* **11**, 912083 (2023).
1451 2. Tan, O. L. & Fleming, J. S. Proliferating cell nuclear antigen immunoreactivity in the ovarian surface
1452 epithelium of mice of varying ages and total lifetime ovulation number following ovulation. *Biol.*
1453 *Reprod.* **71**, 1501–1507 (2004).
1454 3. Wang, J., Wang, D., Chu, K., Li, W. & Zeng, Y. A. Procr-expressing progenitor cells are responsible
1455 for murine ovulatory rupture repair of ovarian surface epithelium. *Nat. Commun.* **10**, 4966 (2019).
1456 4. Williams, C. J. & Erickson, G. F. Morphology and physiology of the ovary. in *Endotext* (MDText.com,
1457 Inc., South Dartmouth (MA), 2000).
1458 5. Stickels, R. R. *et al.* Highly sensitive spatial transcriptomics at near-cellular resolution with Slide-
1459 seqV2. *Nat. Biotechnol.* **39**, 313–319 (2021).
1460 6. Rodriques, S. G. *et al.* Slide-seq: A scalable technology for measuring genome-wide expression at
1461 high spatial resolution. *Science* **363**, 1463–1467 (2019).
1462 7. Dunlop, C. E. & Anderson, R. A. The regulation and assessment of follicular growth. *Scand. J. Clin.*
1463 *Lab. Invest. Suppl.* **244**, 13–7; discussion 17 (2014).
1464 8. Shirasuna, K. & Iwata, H. Effect of aging on the female reproductive function. *Contracept. Reprod.*
1465 *Med.* **2**, 23 (2017).
1466 9. Amargant, F. *et al.* Ovarian stiffness increases with age in the mammalian ovary and depends on
1467 collagen and hyaluronan matrices. *Aging Cell* **19**, e13259 (2020).
1468 10. Mara, J. N. *et al.* Ovulation and ovarian wound healing are impaired with advanced reproductive age.
1469 *Aging (Albany NY)* **12**, 9686–9713 (2020).
1470 11. Briley, S. M. *et al.* Reproductive age-associated fibrosis in the stroma of the mammalian ovary. *J*
1471 *Reprod Fertil* **152**, 245–260 (2016).
1472 12. Lliberos, C. *et al.* Evaluation of inflammation and follicle depletion during ovarian ageing in mice.
1473 *Sci. Rep.* **11**, 278 (2021).

1474 13. Wilkosz, P., Greggains, G. D., Tanbo, T. G. & Fedorcsak, P. Female reproductive decline is
1475 determined by remaining ovarian reserve and age. *PLoS One* **9**, e108343 (2014).
1476 14. LaVoie, H. A. Transcriptional control of genes mediating ovarian follicular growth, differentiation,
1477 and steroidogenesis in pigs. *Mol. Reprod. Dev.* **84**, 788–801 (2017).
1478 15. Vazakidou, P. *et al.* The profile of steroid hormones in human fetal and adult ovaries. *Reprod. Biol.*
1479 *Endocrinol.* **22**, 60 (2024).
1480 16. Richards, J. S., Ren, Y. A., Candelaria, N., Adams, J. E. & Rajkovic, A. Ovarian follicular theca cell
1481 recruitment, differentiation, and impact on fertility: 2017 update. *Endocr. Rev.* **39**, 1–20 (2018).
1482 17. Orisaka, M., Tajima, K., Tsang, B. K. & Kotsuji, F. Oocyte-granulosa-theca cell interactions during
1483 preantral follicular development. *J. Ovarian Res.* **2**, 9 (2009).
1484 18. McGee, E. A. & Hsueh, A. J. Initial and cyclic recruitment of ovarian follicles. *Endocr. Rev.* **21**, 200–
1485 214 (2000).
1486 19. Duncan, W. C., Cowen, G. M. & Illingworth, P. J. Steroidogenic enzyme expression in human corpora
1487 lutea in the presence and absence of exogenous human chorionic gonadotrophin (HCG). *Mol. Hum.*
1488 *Reprod.* **5**, 291–298 (1999).
1489 20. Peck, J. D. *et al.* Lifestyle factors associated with histologically derived human ovarian non-growing
1490 follicle count in reproductive age women. *Hum. Reprod.* **31**, 150–157 (2016).
1491 21. Zheng, J.-H. *et al.* A stereological study of mouse ovary tissues for 3D bioprinting application. *Cell.*
1492 *Mol. Bioeng.* **14**, 259–265 (2021).
1493 22. te Velde, E. R. & Pearson, P. L. The variability of female reproductive ageing. *Hum. Reprod. Update*
1494 **8**, 141–154 (2002).
1495 23. Esencan, E., Beroukhim, G. & Seifer, D. B. Age-related changes in Folliculogenesis and potential
1496 modifiers to improve fertility outcomes - A narrative review. *Reprod. Biol. Endocrinol.* **20**, 156 (2022).
1497 24. Zhang, Z., Schlamp, F., Huang, L., Clark, H. & Brayboy, L. Inflammaging is associated with shifted
1498 macrophage ontogeny and polarization in the aging mouse ovary. *J Reprod Fertil* **159**, 325–337
1499 (2020).

1500 25. Jones, A. S. K. *et al.* Cellular atlas of the human ovary using morphologically guided spatial
1501 transcriptomics and single-cell sequencing. *Sci. Adv.* **10**, eadm7506 (2024).
1502 26. Alberico, H. C. & Woods, D. C. Role of granulosa cells in the aging ovarian landscape: A focus on
1503 mitochondrial and metabolic function. *Front. Physiol.* **12**, 800739 (2021).
1504 27. Cai, M. *et al.* Quercetin activates autophagy to protect rats ovarian granulosa cells from H2O2-induced
1505 aging and injury. *Eur. J. Pharmacol.* **966**, 176339 (2024).
1506 28. Zou, X. *et al.* Peroxiredoxin 4 deficiency induces accelerated ovarian aging through destroyed
1507 proteostasis in granulosa cells. *Biochim. Biophys. Acta Mol. Basis Dis.* **1870**, 167334 (2024).
1508 29. Dipali, S. S. *et al.* Proteomic quantification of native and ECM-enriched mouse ovaries reveals an age-
1509 dependent fibro-inflammatory signature. *Aging (Albany NY)* **15**, 10821–10855 (2023).
1510 30. Grosbois, J., Bailie, E. C., Kelsey, T. W., Anderson, R. A. & Telfer, E. E. Spatio-temporal remodelling
1511 of the composition and architecture of the human ovarian cortical extracellular matrix during in vitro
1512 culture. *Hum. Reprod.* **38**, 444–458 (2023).
1513 31. Pietroforte, S., Plough, M. & Amargant, F. Age-associated increased stiffness of the ovarian
1514 microenvironment impairs follicle development and oocyte quality and rapidly alters follicle gene
1515 expression. *bioRxivorg* (2024) doi:10.1101/2024.06.09.598134.
1516 32. Hense, J. D. *et al.* The role of cellular senescence in ovarian aging. *NPJ Aging* **10**, 35 (2024).
1517 33. Isola, J. V. V. *et al.* Reproductive Ageing: Inflammation, immune cells, and cellular senescence in the
1518 aging ovary. *J Reprod Fertil* **168**, (2024).
1519 34. Trimmer, K. A. *et al.* Spatial single-cell sequencing of meiosis I arrested oocytes indicates acquisition
1520 of maternal transcripts from the soma. *Cell Rep.* **42**, 112544 (2023).
1521 35. Landry, D. A. *et al.* Metformin prevents age-associated ovarian fibrosis by modulating the immune
1522 landscape in female mice. *Sci. Adv.* **8**, eabq1475 (2022).
1523 36. Wang, Z., Liu, C.-Y., Zhao, Y. & Dean, J. FIGLA, LHX8 and SOHLH1 transcription factor networks
1524 regulate mouse oocyte growth and differentiation. *Nucleic Acids Res.* **48**, 3525–3541 (2020).
1525 37. Morris, M. E. *et al.* A single-cell atlas of the cycling murine ovary. *Elife* **11**, e77239 (2022).

1526 38. Ben Yaakov, T., Wasserman, T., Aknin, E. & Savir, Y. Single-cell analysis of the aged ovarian
1527 immune system reveals a shift towards adaptive immunity and attenuated cell function. *Elife* **12**,
1528 (2023).
1529 39. Isola, J. V. V. *et al.* A single-cell atlas of the aging mouse ovary. *Nat. Aging* **4**, 145–162 (2024).
1530 40. Winkler, I. *et al.* The cycling and aging mouse female reproductive tract at single-cell resolution. *Cell*
1531 **187**, 981-998.e25 (2024).
1532 41. Huang, R. *et al.* Single-cell and spatiotemporal profile of ovulation in the mouse ovary. *bioRxivorg*
1533 (2024) doi:10.1101/2024.05.20.594719.
1534 42. Bingel, A. S. & Schwartz, N. B. Timing of LH release and ovulation in the cyclic mouse. *J. Reprod.*
1535 *Fertil.* **19**, 223–229 (1969).
1536 43. Chen, Y.-Y. *et al.* Single-cell transcriptomics of staged oocytes and somatic cells reveal novel
1537 regulators of follicle activation. *J Reprod Fertil* **164**, 55–70 (2022).
1538 44. Liu, L. *et al.* Identification of biomarkers for predicting ovarian reserve of primordial follicle via
1539 transcriptomic analysis. *Front. Genet.* **13**, 879974 (2022).
1540 45. Baarends, W. M. Anti-mullerian hormone and anti-mullerian hormone type II receptor messenger
1541 ribonucleic acid expression in rat ovaries during postnatal development, the estrous cycle, and
1542 gonadotropin-induced follicle growth. *Endocrinology* **136**, 4951–4962 (1995).
1543 46. Binder, A. K., Winuthayanon, W., Hewitt, S. C., Couse, J. F. & Korach, K. S. Steroid receptors in the
1544 uterus and ovary. in *Knobil and Neill's Physiology of Reproduction* vol. 1 1099–1193 (Elsevier, 2015).
1545 47. Jeppesen, J. V. *et al.* LH-receptor gene expression in human granulosa and cumulus cells from antral
1546 and preovulatory follicles. *J. Clin. Endocrinol. Metab.* **97**, E1524-31 (2012).
1547 48. Conti, M. & Kunitomi, C. A genome-wide perspective of the maternal mRNA translation program
1548 during oocyte development. *Semin. Cell Dev. Biol.* **154**, 88–98 (2024).
1549 49. Rajkovic, A., Pangas, S. A., Ballow, D., Suzumori, N. & Matzuk, M. M. NOBOX deficiency disrupts
1550 early folliculogenesis and oocyte-specific gene expression. *Science* **305**, 1157–1159 (2004).

1551 50. Kocabas, A. M. *et al.* The transcriptome of human oocytes. *Proc. Natl. Acad. Sci. U. S. A.* **103**, 14027–
1552 14032 (2006).
1553 51. Jaffe, L. A. & Egbert, J. R. Regulation of mammalian oocyte meiosis by intercellular communication
1554 within the ovarian follicle. *Annu. Rev. Physiol.* **79**, 237–260 (2017).
1555 52. Manova, K., Nocka, K., Besmer, P. & Bachvarova, R. F. Gonadal expression of c-kit encoded at the
1556 W locus of the mouse. *Development* **110**, 1057–1069 (1990).
1557 53. Paulini, F. & Melo, E. O. The role of oocyte-secreted factors GDF9 and BMP15 in follicular
1558 development and oogenesis: GDF9 and BMP15 and the follicular development. *Reprod. Domest.*
1559 *Anim.* **46**, 354–361 (2011).
1560 54. Tanaka, M., Hennebold, J. D., Macfarlane, J. & Adashi, E. Y. A mammalian oocyte-specific linker
1561 histone gene H1oo: homology with the genes for the oocyte-specific cleavage stage histone (cs-H1)
1562 of sea urchin and the B4/H1M histone of the frog. *Development* **128**, 655–664 (2001).
1563 55. Pangas, S. A. *et al.* Oogenesis requires germ cell-specific transcriptional regulators Sohlh1 and Lhx8.
1564 *Proc. Natl. Acad. Sci. U. S. A.* **103**, 8090–8095 (2006).
1565 56. Hinsch, K. D. & Hinsch, E. The zona pellucida "receptors" ZP1, ZP2 and ZP3. *Andrologia* **31**, 320–
1566 322 (1999).
1567 57. Hoodbhoy, T. *et al.* ZP2 and ZP3 traffic independently within oocytes prior to assembly into the
1568 extracellular zona pellucida. *Mol. Cell. Biol.* **26**, 7991–7998 (2006).
1569 58. Xie, J., Jin, Y. & Wang, G. The role of SCF ubiquitin-ligase complex at the beginning of life. *Reprod.*
1570 *Biol. Endocrinol.* **17**, 101 (2019).
1571 59. De La Chesnaye, E. *et al.* Fbxw15/Fbxo12J is an F-box protein-encoding gene selectively expressed
1572 in oocytes of the mouse ovary. *Biol. Reprod.* **78**, 714–725 (2008).
1573 60. Yoon, S.-J. *et al.* Role of Bcl2-like 10 (Bcl2l10) in regulating mouse oocyte maturation. *Biol. Reprod.*
1574 **81**, 497–506 (2009).
1575 61. Yu, C. *et al.* BTG4 is a meiotic cell cycle-coupled maternal-zygotic-transition licensing factor in
1576 oocytes. *Nat. Struct. Mol. Biol.* **23**, 387–394 (2016).

1577 62. Narducci, M. G. *et al.* TCL1 participates in early embryonic development and is overexpressed in
1578 human seminomas. *Proc. Natl. Acad. Sci. U. S. A.* **99**, 11712–11717 (2002).
1579 63. Miao, Y.-L., Kikuchi, K., Sun, Q.-Y. & Schatten, H. Oocyte aging: cellular and molecular changes,
1580 developmental potential and reversal possibility. *Hum. Reprod. Update* **15**, 573–585 (2009).
1581 64. Moghadam, A. R. E., Moghadam, M. T., Hemadi, M. & Saki, G. Oocyte quality and aging. *JBRA*
1582 *Assist. Reprod.* **26**, 105–122 (2022).
1583 65. Gill, A., Jamnongjit, M. & Hammes, S. R. Androgens promote maturation and signaling in mouse
1584 oocytes independent of transcription: a release of inhibition model for mammalian oocyte meiosis.
1585 *Mol. Endocrinol.* **18**, 97–104 (2004).
1586 66. Kawakami, S.-Y., Nansai, C. & Niimura, S. Inhibition of 20Î±-Hydroxysteroid Dehydrogenase
1587 Activity in Mouse Oocyte by Human 20Î±-HSD (AKR1C1) Inhibitor. *J. Biol. Today S World* **9**, 1–4
1588 (2020).
1589 67. Niimura, S. & Kawakami, S.-Y. Changes in the activities of hydroxysteroid dehydrogenases in mouse
1590 oocytes during meiotic maturation. *J. Reprod. Dev.* **49**, 451–456 (2003).
1591 68. Parkening, T. A., Collins, T. J. & Smith, E. R. Plasma and pituitary concentrations of LH, FSH, and
1592 prolactin in aging C57BL/6 mice at various times of the estrous cycle. *Neurobiol. Aging* **3**, 31–35
1593 (1982).
1594 69. Nelson, J. F., Felicio, L. S., Osterburg, H. H. & Finch, C. E. Differential contributions of ovarian and
1595 extraovarian factors to age-related reductions in plasma estradiol and progesterone during the estrous
1596 cycle of C57BL/6J mice. *Endocrinology* **130**, 805–810 (1992).
1597 70. Bondy, C. A. *et al.* Cellular distribution of insulin-degrading enzyme gene expression. Comparison
1598 with insulin and insulin-like growth factor receptors. *J. Clin. Invest.* **93**, 966–973 (1994).
1599 71. Acevedo, N., Ding, J. & Smith, G. D. Insulin signaling in mouse oocytes. *Biol. Reprod.* **77**, 872–879
1600 (2007).

1601 72. Landau, S., Braw-Tal, R., Kaim, M., Bor, A. & Bruckental, I. Preovulatory follicular status and diet
1602 affect the insulin and glucose content of follicles in high-yielding dairy cows. *Anim. Reprod. Sci.* **64**,
1603 181–197 (2000).
1604 73. Kanzaki, S. *et al.* Involvement of Nlrp9a/b/c in mouse preimplantation development. *J Reprod Fertil*
1605 **160**, 181–191 (2020).
1606 74. Van Gorp, H., Kuchmiy, A., Van Hauwermeiren, F. & Lamkanfi, M. NOD-like receptors interfacing
1607 the immune and reproductive systems. *FEBS J.* **281**, 4568–4582 (2014).
1608 75. Peng, H., Zhang, W., Xiao, T. & Zhang, Y. Expression patterns of Nlrp9a, Nlrp9b and Nlrp9c during
1609 mouse development. *Biologia (Bratisl.)* **69**, 107–112 (2014).
1610 76. Kotliar, D. *et al.* Reproducible single cell annotation of programs underlying T-cell subsets, activation
1611 states, and functions. *bioRxivorg* (2024) doi:10.1101/2024.05.03.592310.
1612 77. Galbraith, M. D. *et al.* CDK8 kinase activity promotes glycolysis. *Cell Rep.* **21**, 1495–1506 (2017).
1613 78. Zhu, C. *et al.* Hexosaminidase B-driven cancer cell-macrophage co-dependency promotes glycolysis
1614 addiction and tumorigenesis in glioblastoma. *Nat. Commun.* **15**, 8506 (2024).
1615 79. Naelitz, B. D. & Sharifi, N. Through the looking-glass: Reevaluating DHEA metabolism through
1616 HSD3B1 genetics. *Trends Endocrinol. Metab.* **31**, 680–690 (2020).
1617 80. Diraison, F. *et al.* Translationally controlled tumour protein (TCTP) is a novel glucose-regulated
1618 protein that is important for survival of pancreatic beta cells. *Diabetologia* **54**, 368–379 (2011).
1619 81. Fan, Z. *et al.* CMSS1: A RNA binding protein with pivotal roles in non-small cell lung cancer
1620 progression and prognosis. *BMC Cancer* **25**, 688 (2025).
1621 82. Lau, S. H. *et al.* Clusterin plays an important role in hepatocellular carcinoma metastasis. *Oncogene*
1622 **25**, 1242–1250 (2006).
1623 83. McGovern, K. E. *et al.* SPARC coordinates extracellular matrix remodeling and efficient recruitment
1624 to and migration of antigen-specific T cells in the brain following infection. *Sci. Rep.* **11**, 4549 (2021).
1625 84. Ramella, M. *et al.* Relevance of inflammation and matrix remodeling in abdominal aortic aneurysm
1626 (AAA) and popliteal artery aneurysm (PAA) progression. *Am. J. Transl. Res.* **10**, 3265–3275 (2018).

1627 85. Zhang, X., Tang, N., Hadden, T. J. & Rishi, A. K. Akt, FoxO and regulation of apoptosis. *Biochim.*
1628 *Biophys. Acta* **1813**, 1978–1986 (2011).
1629 86. Yan, H.-Z. *et al.* GHR is involved in gastric cell growth and apoptosis via PI3K/AKT signalling. *J.*
1630 *Cell. Mol. Med.* **25**, 2450–2458 (2021).
1631 87. He, X. *et al.* PIK3IP1, a Negative Regulator of PI3K, Suppresses the Development of Hepatocellular
1632 Carcinoma. *Cancer Research* **68**, 5591–5598 (2008).
1633 88. Hector, M. *et al.* Moss-derived human complement factor H modulates retinal immune response and
1634 attenuates retinal degeneration. *J. Neuroinflammation* **22**, 104 (2025).
1635 89. Chao, M. P., Weissman, I. L. & Majeti, R. The CD47-SIRPα pathway in cancer immune evasion and
1636 potential therapeutic implications. *Curr. Opin. Immunol.* **24**, 225–232 (2012).
1637 90. Hsueh, A. J., Billig, H. & Tsafriri, A. Ovarian follicle atresia: a hormonally controlled apoptotic
1638 process. *Endocr. Rev.* **15**, 707–724 (1994).
1639 91. Tilly, J. L., Kowalski, K. I., Johnson, A. L. & Hsueh, A. J. Involvement of apoptosis in ovarian
1640 follicular atresia and postovulatory regression. *Endocrinology* **129**, 2799–2801 (1991).
1641 92. Klein, D. *et al.* Mapping cells through time and space with moscot. *Nature* **638**, 1065–1075 (2025).
1642 93. Browaeys, R. *et al.* MultiNicheNet: a flexible framework for differential cell-cell communication
1643 analysis from multi-sample multi-condition single-cell transcriptomics data. *bioRxiv*
1644 2023.06.13.544751 (2023) doi:10.1101/2023.06.13.544751.
1645 94. Hofmann, S. M. *et al.* Adipocyte LDL receptor-related protein-1 expression modulates postprandial
1646 lipid transport and glucose homeostasis in mice. *J. Clin. Invest.* **117**, 3271–3282 (2007).
1647 95. Benitez-Amaro, A. *et al.* Low-density lipoprotein receptor-related protein 1 deficiency in
1648 cardiomyocytes reduces susceptibility to insulin resistance and obesity. *Metabolism* **106**, 154191
1649 (2020).
1650 96. Qu, J. *et al.* Low-density lipoprotein receptor-related protein 1 (LRP1) is a novel receptor for
1651 apolipoprotein A4 (APOA4) in adipose tissue. *Sci. Rep.* **11**, 13289 (2021).

1652 97. Day, F. *et al.* Large-scale genome-wide meta-analysis of polycystic ovary syndrome suggests shared
1653 genetic architecture for different diagnosis criteria. *PLoS Genet.* **14**, e1007813 (2018).
1654 98. Deb, S., Campbell, B. K., Clewes, J. S., Pincott-Allen, C. & Raine-Fenning, N. J. Intracycle variation
1655 in number of antral follicles stratified by size and in endocrine markers of ovarian reserve in women
1656 with normal ovulatory menstrual cycles: Intracycle variation in markers of ovarian reserve. *Ultrasound*
1657 *Obstet. Gynecol.* **41**, 216–222 (2013).
1658 99. Kagabu, S. & Umezu, M. Histological analysis of the "critical point" in follicular development in
1659 mice. *Reprod. Med. Biol.* **3**, 141–145 (2004).
1660 100. Richard, S., Zhou, Y., Jasoni, C. L. & Pankhurst, M. W. Ovarian follicle size or growth rate can both
1661 be determinants of ovulatory follicle selection in mice. *Biol. Reprod.* **110**, 130–139 (2024).
1662 101. Visser, J. A. *et al.* Increased oocyte degeneration and follicular atresia during the estrous cycle in anti-
1663 Müllerian hormone null mice. *Endocrinology* **148**, 2301–2308 (2007).
1664 102. Holesh, J. E., Bass, A. N. & Lord, M. Physiology, ovulation. (2017).
1665 103. Gusmao, D. O. *et al.* Pattern of gonadotropin secretion along the estrous cycle of C57BL/6 female
1666 mice. *Physiol. Rep.* **10**, e15460 (2022).
1667 104. Wall, E. G. *et al.* Unexpected plasma gonadal steroid and prolactin levels across the mouse estrous
1668 cycle. *Endocrinology* **164**, bqad070 (2023).
1669 105. Cunningham, A. C. *et al.* Chronicling menstrual cycle patterns across the reproductive lifespan with
1670 real-world data. *Sci. Rep.* **14**, 10172 (2024).
1671 106. Peluso, J. J., Steger, R. W., Huang, H. & Meites, J. Pattern of follicular growth and steroidogenesis in
1672 the ovary of aging cycling rats. *Exp. Aging Res.* **5**, 319–333 (1979).
1673 107. Lee-Thacker, S. *et al.* Core Binding Factors are essential for ovulation, luteinization, and female
1674 fertility in mice. *Sci. Rep.* **10**, 9921 (2020).
1675 108. Romereim, S. M. *et al.* Gene expression profiling of bovine ovarian follicular and luteal cells provides
1676 insight into cellular identities and functions. *Mol. Cell. Endocrinol.* **439**, 379–394 (2017).

1677 109. Abedel-Majed, M. A., Romereim, S. M., Davis, J. S. & Cupp, A. S. Perturbations in lineage
1678 specification of granulosa and theca cells may alter corpus luteum formation and function. *Front.*
1679 *Endocrinol. (Lausanne)* **10**, 832 (2019).
1680 110. Gaytan, F. *et al.* Development and validation of a method for precise dating of female puberty in
1681 laboratory rodents: The puberty ovarian maturation score (Pub-Score). *Sci. Rep.* **7**, 46381 (2017).
1682 111. Sato, J., Hashimoto, S., Doi, T., Yamada, N. & Tsuchitani, M. Histological characteristics of the
1683 regression of corpora lutea in wistar hannover rats: the comparisons with sprague-dawley rats. *J.*
1684 *Toxicol. Pathol.* **27**, 107–113 (2014).
1685 112. Gaytán, F. *et al.* Macrophages, cell proliferation, and cell death in the human menstrual corpus luteum.
1686 *Biol. Reprod.* **59**, 417–425 (1998).
1687 113. Devoto, L. *et al.* Expression of steroidogenic acute regulatory protein in the human corpus luteum
1688 throughout the luteal phase. *J. Clin. Endocrinol. Metab.* **86**, 5633–5639 (2001).
1689 114. Foley, K. G., Pritchard, M. T. & Duncan, F. E. Macrophage-derived multinucleated giant cells:
1690 hallmarks of the aging ovary. *J Reprod Fertil* **161**, V5–V9 (2021).
1691 115. Kloc, M. *et al.* Giant multinucleated cells in aging and senescence-an abridgement. *Biology (Basel)*
1692 **11**, 1121 (2022).
1693 116. Smith, M. F., Ricke, W. A., Bakke, L. J., Dow, M. P. D. & Smith, G. W. Ovarian tissue remodeling:
1694 role of matrix metalloproteinases and their inhibitors. *Mol. Cell. Endocrinol.* **191**, 45–56 (2002).
1695 117. Faas, M. *et al.* The immune response during the luteal phase of the ovarian cycle: a Th2-type response?
1696 *Fertil. Steril.* **74**, 1008–1013 (2000).
1697 118. Poole, D. H. & Pate, J. L. Luteal microenvironment directs resident T lymphocyte function in cows.
1698 *Biol. Reprod.* **86**, 29 (2012).
1699 119. Wynn, T. A. & Vannella, K. M. Macrophages in tissue repair, regeneration, and fibrosis. *Immunity* **44**,
1700 450–462 (2016).
1701 120. Büttner, M., Ostner, J., Müller, C. L., Theis, F. J. & Schubert, B. scCODA is a Bayesian model for
1702 compositional single-cell data analysis. *Nat. Commun.* **12**, 6876 (2021).

1703 121. Baker, S. J. & Spears, N. The role of intra-ovarian interactions in the regulation of follicle dominance.
1704 *Hum. Reprod. Update* **5**, 153–165 (1999).
1705 122. Hyde, K. A. *et al.* Characterization of preantral follicle clustering and neighborhood patterns in the
1706 equine ovary. *PLoS One* **17**, e0275396 (2022).
1707 123. Clement, F. *et al.* Growth kinetics of the granulosa cell population in ovarian follicles: an approach by
1708 mathematical modelling. *Cell Prolif.* **30**, 255–270 (1997).
1709 124. Robker, R. L. & Richards, J. S. Hormonal control of the cell cycle in ovarian cells: proliferation versus
1710 differentiation. *Biol. Reprod.* **59**, 476–482 (1998).
1711 125. Hatzirodos, N. *et al.* Transcriptome profiling of granulosa cells from bovine ovarian follicles during
1712 atresia. *BMC Genomics* **15**, 40 (2014).
1713 126. Irving-Rodgers, H. F., van Wezel, I. L., Mussard, M. L., Kinder, J. E. & Rodgers, R. J. Atresia
1714 revisited: two basic patterns of atresia of bovine antral follicles. *J Reprod Fertil* **122**, 761–775 (2001).
1715 127. Sen, A. *et al.* Androgens regulate ovarian follicular development by increasing follicle stimulating
1716 hormone receptor and microRNA-125b expression. *Proc. Natl. Acad. Sci. U. S. A.* **111**, 3008–3013
1717 (2014).
1718 128. McLean, A. C., Valenzuela, N., Fai, S. & Bennett, S. A. L. Performing vaginal lavage, crystal violet
1719 staining, and vaginal cytological evaluation for mouse estrous cycle staging identification. *J. Vis. Exp.*
1720 e4389 (2012).
1721 129. Byers, S. L., Wiles, M. V., Dunn, S. L. & Taft, R. A. Mouse estrous cycle identification tool and
1722 images. *PLoS One* **7**, e35538 (2012).
1723 130. Ajayi, A. F. & Akhigbe, R. E. Staging of the estrous cycle and induction of estrus in experimental
1724 rodents: an update. *Fertil. Res. Pract.* **6**, 5 (2020).
1725 131. Zheng, G. X. Y. *et al.* Massively parallel digital transcriptional profiling of single cells. *Nat. Commun.*
1726 **8**, 14049 (2017).
1727 132. Dobin, A. *et al.* STAR: ultrafast universal RNA-seq aligner. *Bioinformatics* **29**, 15–21 (2013).

1728 133. Wolf, F. A., Angerer, P. & Theis, F. J. SCANPY: large-scale single-cell gene expression data analysis.
1729 *Genome Biol.* **19**, 15 (2018).
1730 134. Korsunsky, I. *et al.* Fast, sensitive and accurate integration of single-cell data with Harmony. *Nat.*
1731 *Methods* **16**, 1289–1296 (2019).
1732 135. Traag, V. A., Waltman, L. & van Eck, N. J. From Louvain to Leiden: guaranteeing well-connected
1733 communities. *Sci. Rep.* **9**, 5233 (2019).
1734 136. Armstrong, G. *et al.* Uniform Manifold Approximation and Projection (UMAP) reveals composite
1735 patterns and resolves visualization artifacts in microbiome data. *mSystems* **6**, e0069121 (2021).
1736 137. Palla, G. *et al.* Squidpy: a scalable framework for spatial omics analysis. *Nat. Methods* **19**, 171–178
1737 (2022).
1738 138. Lotfollahi, M. *et al.* Mapping single-cell data to reference atlases by transfer learning. *Nat. Biotechnol.*
1739 **40**, 121–130 (2022).
1740 139. Pangas, S. A. *et al.* Intraovarian activins are required for female fertility. *Mol. Endocrinol.* **21**, 2458–
1741 2471 (2007).
1742 140. Mantri, M., Zhang, H. H., Spanos, E., Ren, Y. A. & De Vlaminck, I. A spatiotemporal molecular atlas
1743 of the ovulating mouse ovary. *Proc. Natl. Acad. Sci. U. S. A.* **121**, e2317418121 (2024).
1744 141. Meinsohn, M.-C. *et al.* Single-cell sequencing reveals suppressive transcriptional programs regulated
1745 by MIS/AMH in neonatal ovaries. *Proc. Natl. Acad. Sci. U. S. A.* **118**, e2100920118 (2021).
1746 142. Le Goascogne, C. *et al.* Immunoreactive cytochrome P-450(17 alpha) in rat and guinea-pig gonads,
1747 adrenal glands and brain. *J. Reprod. Fertil.* **93**, 609–622 (1991).
1748 143. Kapfhamer, J., Waite, C. & Ascoli, M. The Gαq/11-provoked induction of Akr1c18 in murine luteal
1749 cells is mediated by phospholipase C. *Mol. Cell. Endocrinol.* **470**, 179–187 (2018).
1750 144. Luo, W. & Wiltbank, M. C. Distinct regulation by steroids of messenger RNAs for FSHR and
1751 CYP19A1 in bovine granulosa cells. *Biol. Reprod.* **75**, 217–225 (2006).
1752 145. Yung, Y. *et al.* Localization of luteinizing hormone receptor protein in the human ovary. *Mol. Hum.*
1753 *Reprod.* **20**, 844–849 (2014).

1754 146. Kotliar, D. *et al.* Identifying gene expression programs of cell-type identity and cellular activity with
1755 single-cell RNA-Seq. *Elife* **8**, e43803 (2019).
1756 147. Buitinck, L. *et al.* API design for machine learning software: experiences from the scikit-learn project.
1757 *arXiv [cs.LG]* (2013).
1758 148. Haghverdi, L., Büttner, M., Wolf, F. A., Buettner, F. & Theis, F. J. Diffusion pseudotime robustly
1759 reconstructs lineage branching. *Nat. Methods* **13**, 845–848 (2016).
1760 149. Tirosh, I. *et al.* Dissecting the multicellular ecosystem of metastatic melanoma by single-cell RNA-
1761 seq. *Science* **352**, 189–196 (2016).
1762 150. Niu, W. & Spradling, A. C. Two distinct pathways of pregranulosa cell differentiation support follicle
1763 formation in the mouse ovary. *Proc. Natl. Acad. Sci. U. S. A.* **117**, 20015–20026 (2020).
1764 151. Zhang, Y. *et al.* Transcriptome landscape of human folliculogenesis reveals oocyte and granulosa cell
1765 interactions. *Mol. Cell* **72**, 1021-1034.e4 (2018).
1766 152. Wilkinson, H. N. *et al.* Tissue iron promotes wound repair via M2 macrophage polarization and the
1767 chemokine (C-C motif) ligands 17 and 22. *Am. J. Pathol.* **189**, 2196–2208 (2019).
1768 153. Schneider, C. A., Rasband, W. S. & Eliceiri, K. W. NIH Image to ImageJ: 25 years of image analysis.
1769 *Nat. Methods* **9**, 671–675 (2012).
1770
1771